國立臺灣大學理學院化學系

博士論文

Department of Chemistry

College of Science

National Taiwan University

Doctoral Dissertation

螢光奈米感測器開發

Development of Fluorescence Nanosensors

林裕軒

Yu-Syuan Lin

指導教授: 張煥宗 博士

Advisor: Huan-Tsung Chang, Ph.D.

中華民國 112 年 01 月

January, 2023

doi:10.6342/NTU202300566

國立臺灣大學博士學位論文
口試委員會審定書

NTU Ph.D. Dissertation
Oral Defense Approval Form

螢光奈米感測器開發

Development of Fluorescence Nanosensors

本論文係 林裕軒 君（學號 D06223108 ）在國立臺灣大學化學系完成之博士學位論文，於民國 112 年 01 月 16 日承下列考試委員審查通過及口試及格，特此證明。

The student 林裕軒 (student no. D06223108) enrolled in the Ph.D. Program of the Department of Chemistry, NTU has satisfactorily passed the oral defense on 2023/01/16 with the approval of all committee members as follows.

口試委員(Committee Members)：

張 煥 宗 （簽名 Signature）

（指導教授 Advisor）

胡焯淳 黃郁棻

黃志清 陳建甫

系主任、所長 陳振中 （簽章）

(Dept./Institute Chair’s Signature and Seal)

doi:10.6342/NTU202300566

中文摘要

螢光奈米材料具有高靈敏度、專一性及高穩定性，故在環境分析、生物感測器、食品安全及顯影技術中具有潛力。第一部分研究由組氨酸添加各種鹵化物以簡單、新穎且環保的電化學方法合成碳點。鹵化物在碳點的形成中起兩個重要作用；控制反應速率和表面狀態。我們通過傅里葉變換紅外光譜、循環伏安法、電化學阻抗譜和 X 光電子能譜結果驗證了銅離子與碘離子碳點表面配體（咪唑和組氨酸）相互作用。在 0.8 mM 碘離子的條件下，碘離子碳點對銅離子的選擇性高於被測金屬離子（如汞離子和銀離子）。此方法在訊雜比為 3 時對銅離子的偵測極限為 0.22 µM，並通過分析自來水、湖泊和海水樣品來驗證其實用性。

在第二部分中，與水溶性碳點相比，疏水性碳點的性質和應用很少被提及。在這項研究中，採用一鍋法、簡單的化學氧化方法在室溫下將濃硫酸及三酸甘油脂 (triolein, TO) 合成疏水碳點 (TO-C dots)。銅葉綠素鈉 (SCC) 通過光誘導電子轉移淬滅 TO-CD 螢光。在 400 nm 激發下，TO-C dots 在 500 nm 處的螢光強度顯示出對 1.0–10 µM 範圍內的 SCC 濃度的線性相關，偵測極限為 0.61 µM。調味飲料中 SCC 的定量顯示回收率為 98-103%，相對標準偏差小於 6.5%。通過在氫氧化鈉水解，疏水性 TO-C dots 可以簡單地轉化為親水性 TO-C dots。親水性 TO-CD 上磺酰基的存在增強了其對銅離子的配位能力，導致螢光猝滅，從而可以檢測銅離子，其偵測極限為 0.21 µM 和線性範圍為 0.5-10 µM。親水性 TO-CD 對銅離子具有高選擇性（耐受性至少是其他金屬離子的 10 倍）。該測定已通過加標土壤樣品的分析得到驗證，銅離子的回收率為 97.8-99.0%，相對標準偏差低於 2.0%。表面可調式的 TO-CD 展示了它們在快速偵測環境樣品中的銅離子和食品中的 SCC 方面的潛力。

在第三部分中，通過水熱法合成間苯二胺-抗壞血酸碳奈米粒子 (mPA CNPs)，作為一種新型螢光感測器（量子產率 = 10%）用於偵測 pH 和次氯酸鹽。間苯二

胺對於 pH 值和次氯酸鹽的反應性而被選為 CNPs 的主要成分。同時，引入了具有許多含氧基團的抗壞血酸以提高水溶性和增強反應性。因此，mPA CNPs 可以通過自身螢光變化作為 pH 感測器和在中性 pH 下作為次氯酸鹽感測器。所製備的 mPA CNP 在 pH 5.5 至 8.5（$R^2 = 0.989$）的 pH 範圍內以及次氯酸鹽的 0.125-1.25 µM 濃度範圍內（R2＝0.985）表現出線性螢光響應。在中性 pH 條件下，次氯酸鹽的檢測限 (LOD) 計算為 0.029 µM。此外，mPA CNPs 還能應用於細胞中 pH 及次氯酸鹽濃度的成像。

在最後一部分中，聚合物在穀胱甘肽 (GSH) 輔助下可用於製備穩定的螢光金奈米團簇 (Au NCs)。 GSH 為還原劑，而聚合物為模板以穩定形成的 Au NC。製備聚合物模板 GSH-Au NCs 的最佳 pH 值為 11.0。在螢光強度和穩定性方面，聚二烯丙基二甲基銨 (PDDA) 比聚苯乙烯磺酸鹽 (PSS) 更適合製備 Au NCs。硫化氫與金團簇表面反應形成硫化金使 PDDA/GSH-Au NCs 的螢光淬滅。PDDA/GSH-Au NCs 對硫離子的線性檢測範圍為 1-10 µM，偵測極限（訊雜比 = 3）為 0.32 µM。PDDA/GSH-Au NCs 在高鹽度環境下保持穩定，已應用於溫泉水樣品中硫化物離子的定量，具有良好的準確度和回收率。

關鍵字:碳量子點、金奈米團簇、碳奈米粒子、銅離子、銅葉綠素鈉

doi:10.6342/NTU202300566

Abstract

Fluorescent nanomaterials have high sensitivity, specificity, and stability, making them potential candidates for use in environmental analysis, biosensors, food safety, and imaging techniques. First of all, a simple, eco-friendly, and low-cost electrochemical approach has been applied to the syntheses of carbon dots (C dots) from histidine hydrochloride in the absence or presence of halides (Cl, Br, and I) at various potentials up to 10 V. The halides play two important roles in determining the formation of C dots; controlling the reaction rate and surface states. Fourier transform infrared spectroscopy, cyclic voltammetry, electrochemical impedance spectroscopy, and X-ray photoelectron spectroscopy results of I-C dots reveal the interactions of Cu^{2+} with the surface ligands (imidazole and histidine). The I-C dot probe in the presence of 0.8 mM I^- is selective toward Cu^{2+} over the tested metal ions such as Hg^{2+} and Ag^+. Practicality of this probe has been validated by the analyses of tap, lake, and sea water samples, with negligible matrix effects.

In the second part, a one-pot, simple chemical oxidation approach has been applied to synthesize hydrophobic carbon dots (TO-C dots) at room temperature from triolein (TO) in concentrated sulfuric acid solution. Sodium copper chlorophyllin (SCC) quenches

doi:10.6342/NTU202300566

the fluorescence of TO-C dots by a photoinduced electron transfer process. Quantitation of SCC in flavored drinks shows percentage recovery (%R) vaues of 98–103% and relative standard deviation (RSD) values less than 6.5%. The hydrophobic TO-C dots can be simply converted into hydrophilic TO-C dots through hydrolysis in NaOH solution. The presence of sulfonyl groups on the hydrophilic TO-C dots enhances the coordination ability of the CDs toward Cu^{2+} ions, leading to fluorescence quenching which allows for the detection of Cu^{2+} ions. The assay has been validated with the analysis of spiked soil samples, with %R values of Cu concentration of 97.8–99.0% and RSDs below 2.0%. The surface tunable CD probes demonstrate their potential for the rapid screening of Cu^{2+} ions in environmental samples and SCC in foods.

In the third part, *m*-Phenylenediamine carbon nanoparticles (mPA CNPs) were developed through one-pot hydrothermal reaction as a novel fluorescent probe (quantum yield = 10%) for pH and hypochlorite sensing. *m*-Phenylenediamine was chosen as the major component of CNPs for pH and hypochlorite responsiveness. Meanwhile, ascorbic acid with many oxygen-containing groups was introduced to generate favorable functionalities for improved water solubility and enhanced sensing response. The as-prepared mPA CNPs exhibited a linear fluorescence response over the pH ranges from

doi:10.6342/NTU202300566

pH 5.5 to 8.5 ($R^2 = 0.989$), and over the concentration range of 0.125–1.25 μM for hypochlorite ($R^2 = 0.985$). The mPA CNPs were further applied to the cell imaging. The mPA CNPs were also successfully used for cell imaging and sensitive detection of hypochlorite as well as pH changes in biological system.

In the last part, a glutathione (GSH)-assisted approach in the presence of a polymer has been demonstrated for the preparation of stable and fluorescent gold nanoclusters (Au NCs). GSH acts as a reducing agent, while the polymer is used as a template to stabilize the as-formed Au NCs. The optimal pH value for the preparation of polymer-templated GSH-Au NCs is 11.0. With respect to the fluorescence intensity and stability, polydiallyldimethylammonium (PDDA) is more suitable than polystyrene sulfonate (PSS) for the preparation of Au NCs. The PDDA/GSH-Au NCs show sensitivity and selectivity for the quantitation of sulfide ions, with a linear detection range of 1–10 μM and a low detection limit (signal-to-noise ratio = 3) of 0.32 μM. The low-cost PDDA/GSH-Au NCs have been applied to the quantitation of sulfide ions in spring water samples with good accuracy and recovery.

Keyword: carbon dots, gold nanoclusters, carbon nanoparticles, copper ions, Sodium copper chlorophyllin, hypochlorite.

Contents

doi:10.6342/NTU202300566

Table and Scheme Contents

doi:10.6342/NTU202300566

Figure Contents

doi:10.6342/NTU202300566

doi:10.6342/NTU202300566

doi:10.6342/NTU202300566

doi:10.6342/NTU202300566

doi:10.6342/NTU202300566

Chapter 1 Introduction

doi:10.6342/NTU202300566

1.1 Background

Environmental and food safety issues are becoming more prominent as human civilization becomes more urbanized. Toxic chemicals, water pollutants, and illegal additives that have resulted in negative effects on our health have sparked global alarm. Given these negative effects, it is imperative to develop reliable and effective techniques for monitoring these chemicals. Atomic absorption/emission spectrometry (AAS/AES), inductively coupled plasma mass spectrometry (ICP-MS), and liquid chromatography coupled with mass spectrometry (LC-MS) are classic methods for detecting heavy metals or organic pollutants in water [1-4]. These techniques are sensitive and accurate, but they require costly apparatus, well-trained workers, significant sample pretreatment processes, and a lengthy testing period. To achieve sensitive and selective analysis of trace water contaminants, it is still a significant goal to develop simple, quick, resilient, and cost-effective devices/probes. Colorimetric and fluorescent approaches for detecting water pollutants have been developed using nanomaterials such as noble metal nanoparticles (NPs), carbon dots, and semiconductor quantum dots [5-9], in addition to organic probes [10,11]. These probes can enable quick, easy operation and multiplex detection through the selective interaction with the target analytes after suitable surface functionalization with diverse ligands such as thiol compounds, DNA, proteins, and enzymes [12-13]. Label-free optical sensors with desirable qualities in terms of simplicity, speed, compatibility, sensitivity, and selectivity are highly needed to implement real-time and on-site detection of water contamination.

1.2 Carbon dots (C dots)

C dots are quasi-spherical nanocarbon particles with diameters less than 10 nm. Since Xu and colleagues discovered C dots in 2004 [14], a number of approaches for synthesizing them have been developed. These approaches can be broadly classified into two categories: "top-down" and "bottom-up" (Figure 1-1) [15]. The top-down method involves using techniques like arc discharge, electrochemical oxidation, and laser ablation to transform larger bits of carbon structures (such as graphite, graphene, carbon nanotubes, and activated carbon) into nano-sized, fluorescent C dots. For example, Xu and colleagues used an oxidation process between arc-discharged soot and nitric acid to produce fluorescent C dots by purifying single-walled carbon nanotubes (SWCNTs) [14]. However, this approach is rarely used these days due to some downsides, including the use of expensive materials, harsh reaction conditions, and long reaction times. In bottom-up methods, small molecules (such as amino acids, glucose, and citric acid) are used to generate C dots through a sequence of processes

doi:10.6342/NTU202300566

including condensation, polymerization, carbonization, and passivation by hydrothermal or electrochemical methods [15-18]. The properties of C dots are mainly affected by the nature of the precursors [19]. C dot form retains or enhances the properties of the precursors during the processes of dehydration, polymerization, carbonization, and passivation [17].

The rich and distinctive fluorescence properties of C dots are a result of their structural variety. Most scientists believe that a carbonaceous core and a surface passivation layer play the main roles in the complex fluorescence properties of C dots [20]. The carbonaceous core consists of a combination of sp2 and sp3-hybridized carbons, while the surface passivation layer, which is composed of various functional groups, forms on the surface of the carbonaceous core in order to reduce the Gibbs free energy of C dots. At the same time, the surface passivation layer leads to multiple combinations of functional groups, resulting in the complex properties of C dots, such as multicolor emissions and excitation-dependent emissions. These surface functional groups mainly depend on the precursor used and affect the polarity, reactivity, and selectivity of C dots. In addition, C dot properties can also be tuned by heteroatomic (such as N, S, and X) doping, which improves radiative recombination and results in a higher quantum yield [21]. C dots are applied in sensing and imaging due to their

doi:10.6342/NTU202300566

stability to light and salt, low cost, and ease of tuning.

1.3 Applications of C dots

C dots are widely used in sensors and cell imaging due to their inherent fluorescence characteristics, high sensitivity, fast response, simple preparation, and high selectivity. Due to their small size, large specific surface area, and rich surface functional groups, C dots can detect a variety of analytes through static or dynamic quenching. After a dynamic collision with the quencher, the fluorescence of C dots can be quenched due to non-radiative energy transfer or the new ground state of analyte-C dots complex, which indicates dynamic quenching or static quenching, respectively[22]. On the other hand, noncontact mechanisms like the photoinduced electron transfer (PET), inner filter effect (IFE), and fluorescence resonance energy transfer (FRET) can also apply to sensing analytes. C dots are applied to the detection of metal ios such as Cu^{2+} [23], Hg^{2+} [24], Zn^{2+} [25], Fe^{3+} [26], and ClO^{-} [27] which selective interact with the surface groups of C dots mostly carboxylate and amino groups via coordination or electrostatic interaction. For example, C dots prepared from citric acid and hyaluronic acid are selective toward Fe^{3+} [28] and those prepared from o-phenylenediamine are selective toward Cu^{2+} [29], due to the formation of iron-hydroxyl complex and o-phenylenediamine-copper complex on the surface of C dots.

1.4 Gold nanoclusters

Noble metal nanoclusters (NCs) with various protective ligands (e.g., macromolecules, polymers, and tiny organic ligands) form a distinct sub-class of NPs with several to tens of atoms [30]. Metal NCs have molecule-like characteristics such as discrete electronic states and size-dependent fluorescence since the size of the metal core is equal to the electron's Fermi wavelength (ca. 0.7 nm) [31,32]. Metal NCs' optical characteristics are mostly determined by their atomic–level structures, which can be affected by core size, metal composition, capping ligand type, and ligand–surface metal atoms/ions complexation [33]. Gold, silver, and copper are commonly used to synthesis metal NCs. Among them, Gold nanoclusters are the most widely used, due to their stability and higher quantum yield.

Gold NCs (AuNCs) feature a core of few to hundreds of gold atoms and are maintained by ligands on the surface that protect them. Normally, their average size is less than 5 nm [34]. The numbers of Au atoms in the core, oxidation states, structure, and protective ligands all affect the fluorescence of AuNCs [35-38]. Metal NCs exhibit significant fluorescence properties when the metal size is close to the Fermi wavelength.

doi:10.6342/NTU202300566

The metal NCs emit light under ultraviolet light because electrons transfer between occupied d-band and Fermi level (E_f), or between Highest Occupied Molecular Orbital and Lowest Unoccupied Molecular Orbital (HOMO-LUMO) [39]. The continuous frequency band divides into distinct energy levels when the nanoparticle size approaches the Fermi wavelength [40]. The energy level spacing (E) of AuNCs has a significant impact on their fluorescence properties. The E of AuNCs is determined by the ratio of $E_f/N^{1/3}$ to the emission energy, where E_f is the Fermi level of gold and N is the number of Au atoms that make up AuNCs, according to the spherical colloid model [41]. On the other hand, the ligand-to-metal charge transfer transition (LMCT) or ligand-to-metal-metal charge transfer transition (LMMCT) is involved in the fluorescence mechanism of AuNCs, which can convert excited states S1 or S2 (singlet states) into T1 or T2 (triplet states) due to the presence of heavy atoms (Au), resulting in longer-wavelength emission and a longer lifetime (~1 μs). [36, 42, 43] There are many types of ligand used to protect AuNCs. During 1978 to 2000s, a series of research represented found that phosphine can generate small-sized fluorescence AuNCs while well controlling the particle size. [44] In recent two decades, thiols have become one of the most used ligands for synthesizing AuNCs, since the strong interaction of Au-S improves the stability of AuNCs. [45] The unique thiol-Au interaction also played an important role in the size-focusing process in both top-down and bottom-up strategy.

doi:10.6342/NTU202300566

For example, the size of AuNCs can be controlled via changing the ration of lipoic acid and 11-mercaptoundecanoic acid which represent lipoic acid has stronger etching effect than 11-mercaptoundecanoic acid. The emission of AuNCs is caused by charge transfer from the S atom in the sulfhydryl ligand to the core of the AuNCs (LMCT)[46,47]. Thus, the ability of sulfhydryl groups to donate electrons has a significant impact on the fluorescence intensity of AuNCs (Figure. 1-2) [48]. Thiols are convenient to use in the production of AuNCs due to the presence of sulfhydryl groups, but appropriate ligands must be chosen to provide robust fluorescence emission. Furthermore, the specific interaction between the target analyte and the ligand on the metal NCs surface can cause a significant change in theirfluorescence, allowing for a variety of sensing applications ranging from metal ions to small molecules to large macromolecules like nucleic acids and proteins [30,49].

1.5 Application of AuNCs

The advantages of large stock shift and mild synthetic condition drive AuNCs as new star in the sensing field. Similar to C dots, AuNCs are mainly applied to heavy metal ions sensing due to the abundance of the surface functional group. For example, GSH capped AuNCs are used to sensing Cu^{2+} ions via the coordination between Cu^{2+}

doi:10.6342/NTU202300566

ions and amine and carboxylate groups of GSH [50]. In 2018, Nath and college improve the quantum yield of AuNCs to 20% via treating dithiothreitol (DTT) with BSA. The DTT-BSA AuNCs can be used to detect Pb^{2+} ions through the coordination of Pb^{2+} ions and amino acid residues of BSA [51]. Contrary to C dots, Au NCs can also detect analytes by metallophilic interaction causing fluorescence quenching. A classic example is the closed-shell interaction between Hg^{2+} ions ($4f^{14}5d^{10}$) and surface Au^{+} ions ($4f^{14}5d^{10}$) of AuNCs have been wildly used to monitor the Hg^{2+} ions level in water samples [38,52-54]. After Hg^{2+} ions alter the electronic structure of AuNCs, the fluorescence of AuNCs is significantly quenched [55]. Beside this, there is another case of CN^{-} which can dissolve Au in AuNCs in to $Au(CN)^{2-}$ form [56]. Our group has demonstrated BSA-Ce/Au NCs as a ratiometric sensor for CN- based on the fluorescence at 658 nm quench induced by CN^{-} etching Ce/Au core and the fluorescence at 410 nm enhancement due to complexes among BSA, Ce^{4+}, and $[Au(CN)_2]^{-}$ [56]. S^{2-} is an important analyte because of its toxicity. Since the solubility product constant (K_{sp}) of Au_2S is quite low ($1.58*10^{-73}$ M^2), AuNCs are suitable for the detection of S^{2-} [57]. Additionally, our group introduced a one-pot approach to prepare DNA-Au/Ag NCs which is extremely sensitive toward S^{2-} (LOD = 0.83 nM) due to the sulfide formation and the structure change of templated DNA from packed hairpin to random coil structures [58]. As a result, although AuNCs have great sensitivity and

doi:10.6342/NTU202300566

selectivity toward cationic and anionic analytes, most of them are not stable even keep in the refrigerator for above 2 months.

1.6 Motivation

The design of fluorescence nanomaterials is important for biological and analytical applications. In this dissertation, C dots and AuNCs are selected as the platform due to their good photo- and chemo-stability and higher biocompatibility compared to semiconductor quantum dots and organic dyes. Our group has demonstrated the underlying chemistry and strategies of C dots for heavy metal ion detection. However, they can be improved in some ways. First, the key to nanomaterials being applied in our daily lives is cost. Although C dots show great potential in various applications, their yield is not good enough for large-scale production, especially using the most popular hydrothermal method. Second, most of the functional groups on the surface of C dots are amine, carboxylic acid, keto, and hydroxyl groups. Improving the diversity of functional groups can lead to more applications. Third, detecting C dots in complex matrices such as oil, hot spring water, and sea water is still a big challenge and is not well-discussed. The solubility and stability of C dots in these matrices are the key to overcoming this challenge. Therefore, we will use two scalable methods to produce C-dots, chemical oxidation and electrochemical methods. Both of these methods do not involve the danger of high pressure and allow us to observe changes in the precursors at any time. In addition, we will functionalize the surface of C-dots with unusual functional groups such as hydrophobic and sulfonic groups to expand their potential

doi:10.6342/NTU202300566

applications in complex matrix.

Contrary to C dots, AuNCs have been protected by many types of ligands and are soluble in various organic solvents. Although AuNCs show tolerance to solvents, there are still two problems that need to be solved. First, like C dots, AuNCs are not cost-effective due to the expensive ligands such as proteins, DNA, and thiolate molecules. Second, compared to C dots, although AuNCs exhibit longer emission wavelengths and fluorescence lifetimes, their photo-stability is not as good. Therefore, we will attempt to use charged polymers as templates to synthesize AuNCs and observe the effect of different charge polymers on the fluorescence of AuNCs through electrostatic forces to achieve suspension.

1.7 Reference

[1] J. L. Manzoori, H. Abdolmohammad-Zadeh, M. Amjadi, Ultra-trace determination of silver in water samples by electrothermal atomic absorption spectrometry after preconcentration with a ligand-less cloud point extraction methodology, J. Hazard. Mater. 144 (2007) 458–463.

[2] A. Stefansson, I. Gunnarsson, N. Giroud, New methods for the direct determination of dissolved inorganic, organic and total carbon in natural waters by Reagent-Free™ Ion Chromatography and inductively coupled plasma atomic emission spectrometry, Anal. Chim. Acta. 582 (2007) 69–74.

[3] G. Hartmetz, J. Slemrova, Detection of volatile nitrosamines in waste water from chemical plants by combined capillary gas chromatography-mass spectrometry, Bull. Environ. Contam. Toxicol. 25 (1980) 106–112.

[4] G. Tripathi, V. K. Yadav, J. Singh, V. Mishra, Analytical Methods of Water Pollutants Detection. In: D. Pooja, P. Kumar, P. Singh, S. Patil, (Eds.) Sensors in water pollutants monitoring: role of material. (2020) Advanced Functional Materials and Sensors. Springer, Singapore.

[5] J. Chen, A. Zheng, Y. Gao, C. He, G. Wu, Y. Chen, et al., Functionalized CdS quantum dots-based luminescence probe for detection of heavy and transition

doi:10.6342/NTU202300566

metal ions in aqueous solution, Spectrochim. Acta A Mol. Biomol. Spectrosc. 69 (2008) 1044–1052.

[6] M. Annadhasan, T. Muthukumarasamyvel, V.R. Sankar Babu, N. Rajendiran, Green synthesized silver and gold nanoparticles for colorimetric detection of Hg^{2+}, Pb^{2+}, and Mn^{2+} in aqueous medium, ACS Sustainable Chem. Eng. 2 (2014) 887–896.

[7] P. Devi, P. Rajput, A. Thakur, K.-H. Kim, P. Kumar, Recent advances in carbon quantum dot-based sensing of heavy metals in water, TrAC-Trend. Anal. Chem. 114 (2019) 171–195.

[8] H.-W. Chu, B. Unnikrishnan, A. Anand, Y.-W. Lin, C.-C. Huang, Carbon quantum dots for the detection of antibiotics and pesticides, Journal of Food and Drug Analysis 28 (2020) 5.

[9] Y. He, C.-Y. Wen, Z.-J. Guo, Y.-F. Huang, Noble metal nanomaterial-based aptasensors for microbial toxin detection, Journal of Food and Drug Analysis 28 (2020) 508–520.

[10] T. Rasheed, C. Li, F. Nabeel, W. Huang, Y. Zhou, Self-assembly of alternating copolymer vesicles for the highly selective, sensitive and visual detection and quantification of aqueous Hg^{2+}, Chem. Eng. J. 358 (2019) 101–109.

doi:10.6342/NTU202300566

[11] S. Madhupriya, K.P. Elango, Highly selective colorimetric sensing of Cu (II) ions in aqueous solution via modulation of intramolecular charge transfer transition of aminonaphthoquinone chemosensor, Spectrochim. Acta A 97 (2012) 100–104.

[12] C. Wang, C. Yu, Detection of chemical pollutants in water using gold nanoparticles as sensors: a review, Rev. Anal. Chem. 32 (2013) 1–14.

[13] H. Aldewachi, T. Chalati, M. N. Woodroofe, N. Bricklebank, B. Sharrackc, P. Gardiner, Gold nanoparticle-based colorimetric biosensors, Nanoscale 10 (2018) 18–33.

[14] X. Xu, R. Ray, Y. Gu, H.J. Ploehn, L. Gearheart, K. Raker, W.A. Scrivens Electrophoretic analysis and purification of fluorescent single-walled carbon nanotube fragments J. Am. Chem. Soc., 126 (2004) 12736–12737

[15] S. Ross, R.-S. Wu, S.-C. Wei, G.M. Ross, H.-T. Chang, The analytical and biomedical applications of carbon dots and their future theranostic potential: A review. J. Food Drug Anal. 28 2020, 677–695.

[16] P.-C. Hsu, Z.-Y. Shih, C.-H. Lee, H.-T. Chang, Synthesis and analytical applications of photoluminescent carbon nanodots, Green Chem. 14 (2012) 917.

[17] P.-C. Hsu, H.-T. Chang, Synthesis of high-quality carbon nanodots from hydrophilic compounds: role of functional groups, Chem. Commun. 48 (2012) 3984–3986.

doi:10.6342/NTU202300566

[18] P. Roy, P.-C. Chen, A.P. Periasamy, Y.-N. Chen, H.-T. Chang, Photoluminescent carbon nanodots: synthesis, physicochemical properties and analytical applications, Mater. Today 18 (2015) 447–458.

[19] K.W. Chu, S.L. Lee, C.J. Chang, L. Liu, Recent progress of carbon dot precursors and photocatalysis applications, Polymers 11 (2019) 689.

[20] S. Zhu, Y. Song, X. Zhao, J. Shao, J. Zhang, B. Yang, The photoluminescence mechanism in carbon dots (graphene quantum dots, carbon nanodots, and polymer dots): current state and future perspective. Nano Res. 8 (2015) 355–381.

[21] Y. Park, J. Yoo, B. Lim, W. Kwon, S.-W. Rhee, Improving the functionality of carbon nanodots: doping and surface functionalization. J. Mater. Chem. A, 4 (2016) 11582–11603.

[22] F. Zu, F. Yan, Z. Bai, J. Xu, Y. Wang, Y. Huang, X. Zhou, The quenching of the fluorescence of carbon dots: a review on mechanisms and applications. Mikrochim Acta 184 (2017) 1899–1914.

[23] Y. Dong, R. Wang, G. Li, C. Chen, Y. Chi, G. Chen, Polyamine-functionalized carbon quantum dots as fluorescent probes for selective and sensitive detection of copper ions. Anal. Chem. 84 (2012) 6220–6224.

doi:10.6342/NTU202300566

[24] G. Ren, Y. Meng, Q. Zhang, M. Tang, B. Zhu, F. Chai, C. Wang, Z. Su, Nitrogen-doped carbon dots for the detection of mercury ions in living cells and visualization of latent fingerprints. New J. Chem 42 (2018) 6824–6830.

[25] M. Yang, Q. Tang, Y. Meng, J. Liu, T. Feng, X. Zhao, S. Zhu, W. Yu, B. Yang, Reversible "off-on" fluorescence of Zn^{2+}-passivated carbon dots: mechanism and potential for the detection of EDTA and Zn^{2+}. Langmuir 34 (2018) 7767–7775.

[26] Y. Chen, X. Sun, W. Pan, G. Yu, J. Wang, Fe^{3+}-sensitive carbon dots for detection of Fe^{3+} in aqueous solution and intracellular imaging of Fe^{3+} inside fungal cells. Front. Chem. 7 (2020) 911.

[27] Z. Wei, H. Li, S. Liu, W. Wang, H. Chen, L. Xiao, C. Ren, X. Chen. Carbon dots as fluorescent/colorimetric probes for real-time detection of hypochlorite and ascorbic acid in cells and body fluid. Anal. Chem. 91 (2019) 15477–15483.

[28] Q.-L. Wen, Z.-F. Pu, Y.-J. Yang, J. Wang, B.-C. Wu, Y.-L. Hu, P. Liu, J. Ling, Q. Cao, Hyaluronic acid as a material for the synthesis of fluorescent carbon dots and its application for selective detection of Fe^{3+} ion and folic acid. Microchem. J. 159 (2020) 105364.

[29] M. Vedamalai, A.P. Periasamy, C.-W. Wang, Y.-T. Tseng, L.C. Ho, C.-C. Shih, H.-T. Chang, Carbon nanodots prepared from o-phenylenediamine for sensing of Cu^{2+} ions in cells. Nanoscale 6 (2014) 13119–13125.

doi:10.6342/NTU202300566

[30] X. Yuan, Z. Luo, Y. Yu, Q. Yao, J. Xie, Luminescent noble metal nanoclusters as an emerging optical probe for sensor development, Chem. Asian J. 8 (2013) 858–871.

[31] J. Zheng, P.R. Nicovich, R.M. Dickson, Highly fluorescent noble-metal quantum dots, Annu. Rev. Phys. Chem. 58 (2007) 409–431.

[32] R. Jin, C. Zeng, M. Zhou, Y. Chen, Atomically precise colloidal metal nanoclusters and nanoparticles: fundamentals and opportunities, Chem. Rev. 116 (2016) 10346–10413.

[33] X. Kang, M. Zhu, Tailoring the photoluminescence of atomically precise nanoclusters, Chem. Soc. Rev. 48 (2019) 2422–2457.

[34] Y. Zhang, C. Zhang, C. Xu, X. Wang, C. Liu, G.I.N. Waterhouse, Y. Wang, H. Yin, Ultrasmall Au nanoclusters for biomedical and biosensing applications: A mini-review, Talanta 200 (2019) 432–442.

[35] G. Pramanik, J. Humpolickova, J. Valenta, P. Kundu, S. Bals, P. Bour, M. Dracinsky, P. Cigler, Gold nanoclusters with bright near-infrared photoluminescence, Nanoscale 10 (2018) 3792–3798.

[36] Q. Li, M. Zhou, W.Y. So, J. Huang, M. Li, D.R. Kauffman, M. Cotlet, T. Higaki, L.A. Peteanu, Z. Shao, R. Jin, A mono-cuboctahedral series of gold nanoclusters:

doi:10.6342/NTU202300566

Photoluminescence origin, large enhancement, wide tunability, and structure-property correlation, J. Am. Chem. Soc. 141 (2019) 5314–5325.

[37] K. Chaudhari, P.L. Xavier, T. Pradeep, Understanding the evolution of luminescent gold quantum clusters in protein templates, ACS Nano 5 (2011) 8816–8827.

[38] H. Kawasaki, K. Hamaguchi, I. Osaka, R. Arakawa, pH-dependent synthesis of pepsin-mediated gold nanoclusters with blue green and red fluorescent emission, Adv. Funct. Mater. 21 (2011) 3508–3515.

[39] Y. Lu and W. Chen, Sub-nanometre sized metal clusters: from synthetic challenges to the unique property discoveries, Chem. Soc. Rev. 41 (2012) 3594.

[40] A. P. Alivisatos, Science, semiconductor clusters, nanocrystals, and quantum dots, 271 (1996) 933–937.

[41] J. Zheng, C. Zhang and R. M. Dickson, Highly fluorescent, water-soluble, size-tunable gold quantum dots, Phys. Rev. Lett. 93 (2004) 077402.

[42] Q. Yu, P. Gao, K.Y. Zhang, X. Tong, H. Yang, S. Liu, J. Du, Q. Zhao, W. Huang, Luminescent gold nanocluster-based sensing platform for accurate H_2S detection in vitro and in vivo with improved anti-interference, Light Sci. Appl. 6 (2017) e17107.

doi:10.6342/NTU202300566

[43] X.S. Han, X. Luan, H.F. Su, J.J. Li, S.F. Yuan, Z. Lei, Y. Pei, Q.M. Wang, Structure determination of alkynyl-protected gold nanocluster Au_{22} $(tBuC{\equiv}C)_{18}$ and its thermochromic luminescence, Angew. Chem. Int. Ed. 59 (2020) 2309–2312.

[44] L. Naldini, F. Cariati, G. Simonetta, L. Malatesta, Gold–tertiary phosphine derivatives with intermetallic bonds. Chem. Commun. 1966, 647–648.

[45] S. Zhu, X. Wang, Y. Cong, L. Li, Regulating the optical properties of gold nanoclusters for biological applications. ACS Omega 5 (2020) 22702–22707.

[46] C.-C. Huang, Z. Yang, K.-H. Lee and H.-T. Chang, Synthesis of highly fluorescent gold nanoparticles for sensing mercury(II), Angew. Chem. 119 (2007) 6948– 6952.

[47] M. Yu, C. Zhou, J. Liu, J. D. Hankins and J. Zheng, Luminescent gold nanoparticles with pH-dependent membrane adsorption, J. Am. Chem. Soc. 133 (2011) 11014–11017.

[48] H. Chang, H. Chang, Y. Hung, T. Hsiung, Y. Lin and C. Huang, Ligand effect on the luminescence of gold nanodots and its application for detection of total mercury ions in biological samples, RSC Adv., 3 (2013) 4588.

[49] J. Li, J.-J. Zhu, K. Xu, Fluorescent metal nanoclusters: From synthesis to applications, TrAC-Trend. Anal. Chem. 58 (2014) 90–98.

[50] G. Zhang, Y. Li, J. Xu, C. Zhang, S. Shuang, C. Dong, M.M.F. Choi, Glutathione-

protected fluorescent gold nanoclusters for sensitive and selective detection of Cu^{2+}. Sens Actuators B. 183 (2013) 583–588

[51] P. Nath, M. Chatterjee, N. Chanda, Dithiothreitol-facilitated synthesis of bovine serum albumin–gold nanoclusters for Pb(II) ion detection on paper substrates and in live cells. ACS. Appl. Nano. Mater. 1 (2018) 5108−5118.

[52] T. Zhang, H. Xu, S. Xu, B. Dong, Z. Wu, X. Zhang, L. Zhang, H. Song, DNA stabilized Ag–Au alloy nanoclusters and their application as sensing probes for mercury ions. RSC Adv. 6 (2016) 51609–51618.

[53] Y.-H. Lin, W.-L. Tseng, Ultrasensitive sensing of Hg^{2+} and CH_3Hg^+ based on the fluorescence quenching of lysozyme type VI-stabilized gold nanoclusters Anal. Chem. 82 (2010) 9194–9200.

[54] C. Wu, J. Wang, J. Shen, C. Bi, H. Zhou, Coumarin-based Hg^{2+} fluorescent probe: Synthesis and turn-on fluorescence detection in neat aqueous solution Sens. Actuators B. 238 (2017) 683–692.

[55] J. Xie, Y. Zheng, J.Y. Ying, Highly selective and ultrasensitive detection of Hg^{2+} based on fluorescence quenching of Au nanoclusters by Hg^{2+}–Au^+ interactions Chem. Commun. 46 (2010) 961–963.

[56] C.-W. Wang, Y.-N. Chen, B.-Y. Wu, C.-K. Lee, Y.-C. Chen, Y.-H. Huang, H.-T. Chang, Sensitive detection of cyanide using bovine serum albumin-stabilized

doi:10.6342/NTU202300566

cerium/gold nanoclusters. Anal. Bioanal. Chem. 408 (2016) 287–294.

[57] Y. Zhang, M. Li, Q. Niu, P. Gao, G. Zhang, C. Dong, S. Shuang, Gold nanoclusters as fluorescent sensors for selective and sensitive hydrogen sulfide detection. Talanta 171 (2017) 143–151.

[58] W.-Y. Chen, G.-Y. Lan, H.-T. Chang, Use of Fluorescent DNA-templated gold/silver nanoclusters for the detection of sulfide ions. Anal. Chem. 83 (2011) 9450–9455.

doi:10.6342/NTU202300566

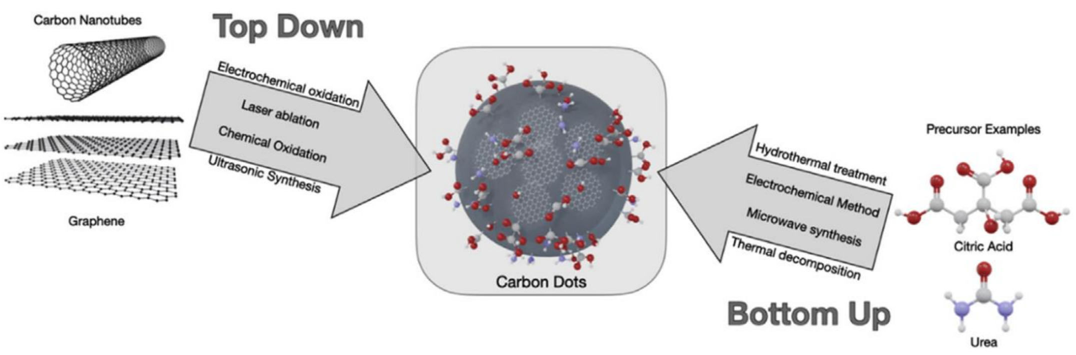

Figure 1-1. Top-down and bottom-up approaches for the synthesis of C-dots.

(Reprinted with permission from ref. 15 Copyright 2020 Elsevier)

doi:10.6342/NTU202300566

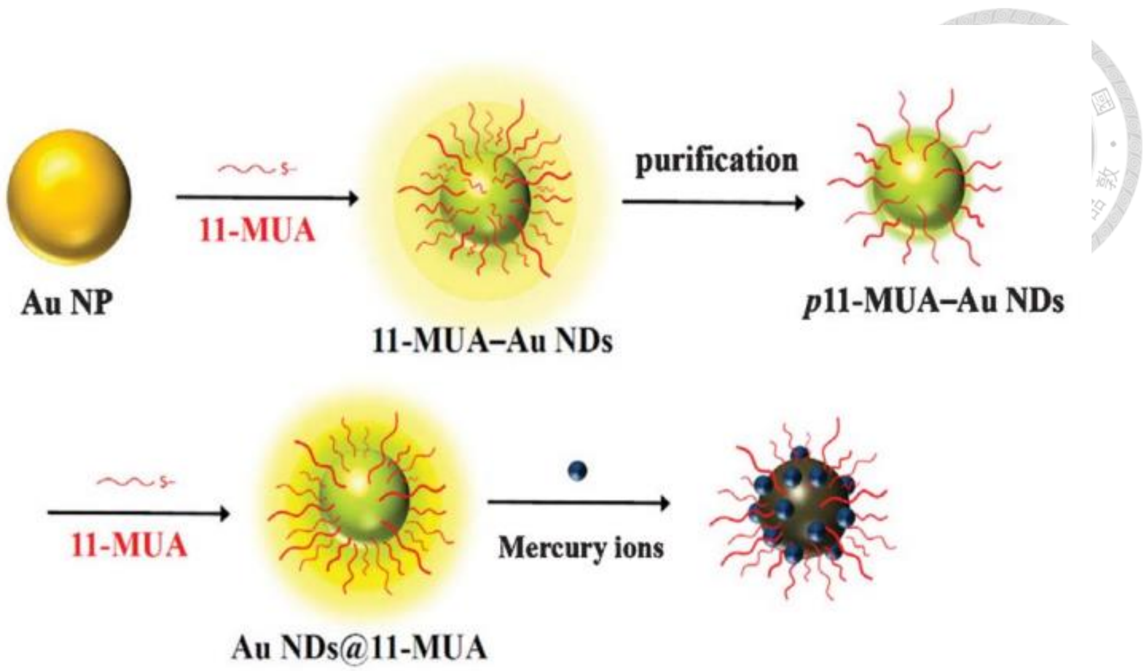

Figure 1-2. Cartoon representation of the preparation of Au NDs@11-MUA for the detection of Hg ions based on Hg-induced luminescence quenching. (Reprinted with permission from ref. 48, Copyright 2013, Royal Society of Chemistry)

Chapter 2 Parameters Affecting the Optical Properties of Carbon Dots Prepared from Histidine

The content in this chapter has been published to: Y.-S. Lin, Y Lin, A.P. Periasamy, J Cang, H.-T. Chang, Parameters affecting the synthesis of carbon dots for quantitation of copper ions. Nanoscale Adv. 1 (2019) 2553–2561.

doi:10.6342/NTU202300566

2.1 Introduction

Photoluminescent nanomaterials such as carbon dots (C dots), quantum dots, nanoclusters, and gold nanodots have become interesting optical sensing materials for detecting various analytes.[1-5] Among them, C dots are more biocompatible and stable against salt and photoirradiation induced photoluminescence (PL) quenching. Most C dots possess interesting excitation dependence PL properties; their emission undergoes a red shift upon increasing the excitation wavelength.[6] Usually, their PL intensity decreases upon increasing the emission wavelength.[7] The interesting PL properties of C dots are related to their core size, surface defects and ligands, oxidation state, as well as number of conjugated π electrons.[1,8-14]

Many approaches, including laser ablation, ultrasonication, direct heating, microwave-assisted heating, plasma treatment, hydrothermal routes, have been applied for the preparation of C dots from different precurssors.[15-21] Among them, the hydrothermal approach is most popular, mainly because of its simplicity.[6,21] It has been reported that C dots are formed through four steps of condensation, polymerization, carbonization, and passivation.[22-24] Various sources, including coffee powder, tea, and apple juice, have been used for preparation of C dots through hydrothermal approaches.[6,25-30] However, hydrothermal approaches require high energy and are usually limited to preparation of few grams of C dots per batch.

doi:10.6342/NTU202300566

Although the formation processes and optical properties of C dots have been suggested,[22-24] strong evidence to support the suggestion/hypothesis is still needed. In this study, we applied our previously developed electrochemical approach to the preparation of C dots from histidine.[31] We previously showed that control of solution pH value is important for the electrochemical preparation of C dots from glycine. However, detailed information about the formation of C dots is missing. We in this study further tested several important factors for controlling the preparation of C dots from histidine, including electrolysis time, concentration of histidine, as well as species and concentrations of salts (electrolytes). We measured the UV-vis absorption and PL spectra of C dots that had been prepared in alkaline solution at 10 V for different periods of time up to 120 min. Through the obtained optical data, we provided more detail information about the effect of halides on the formation of C dots. The C dots prepared in the presence of iodide (I^-) are selective and sensitive for quantitation of copper ions (Cu^{2+}) in the presence of 0.8 mM NaI.

2.2 Experimental Section

2.2.1 Materials.

L-Histidine hydrochloride monohydrate was purchased from TCI (Tokyo, Japan).

doi:10.6342/NTU202300566

Potassium nitrate (>99.0%), silver nitrate (>99.0%), and sodium chloride (>99.0%) were purchased from Sigma-Aldrich (St. Louis, MO, USA). Copper nitrate trihydrate (>99.0%), lead nitrate (>99.0%), and sodium bromide (99.5 %) were purchased from Acros (Morris Plains, NJ, USA). Magnesium nitrate hexahydrate (>98.0%) and sodium iodide (>99.0%) were procured from SHOWA (Tokyo, Japan). Cobalt chloride (97.0%), iron chloride (98.0%), and mercury chloride (>98.0%) were obtained from Alfa Aesar (Heysham, England). Calcium nitrate tetrahydrate (>99.0%) and manganese chloride dehydrate (>99.0%) were purchased from Merck (Kenilworth, NJ, USA). Monobasic, dibasic, and tribasic sodium salts of phosphate, phosphoric acid (85.0%), sodium hydroxide (98.0%), and zinc nitrate hexahydrate (>99.0%) were obtained from J.T. Baker (Center Valley, PA, USA). Ultrapure water (18.2 MΩ cm) from a Milli-Q system (Millipore, Billerica, MA, USA) was used to prepare all solutions.

2.2.2 Preparation of C dots.

A two-platinum-electrode electrochemical system was used for the synthesis of C dots. The length and diameter of the Pt electrode are 6 and 0.05 cm, respectively. A single output direct current (DC) power supply (TP-1303C, Taipei, Taiwan) was used for the synthesis of C dots under a static potential (1 to 10 V) between the two electrodes. Known amounts (0.38-3.83 g) of histidine hydrochloride were dissolved separately in

doi:10.6342/NTU202300566

NaOH solution (1 M) to obtain final concentrations of 0.09-0.90 M, with a final pH value of 9.0 that was adjusted with 10 M HCl or NaOH. To study the effect of halides on the formation of C dots from histidine, aqueous solutions of NaCl (0–2.34 g), NaBr (2.06 g), or NaI (3.00 g) were added to the histidine solutions (20 mL). Aliquots (10 μL) of the solutions after being subjected to the electrolysis for various periods of time (1-120 min) were taken out for spectrochemical measurement. For quantitation of Cu^{2+} ions, the C dots that had been prepared at 10 V for 120 min and had been left undisturbed at ambient temperature (25 °C) for two days were used. This solution was then filtered through a 0.22 μm membrane to remove large particles, which was then subjected to dialysis against pure water through a membrane (MWCO = 100–500D) for 24 h. For simplicity, C dots prepared in the presence of Cl^-, Br^-, and I^- are denoted as Cl-C, Br-C, and I-C dots, respectively. Their concentrations are presented as 1X for simplicity.

2.2.3 Characterization.

Aqueous solutions of four different C dots were subjected to PL measurements using a microplate fluorometer (Synergy 4 Multi-Mode Microplate Reader) from BioTek instruments (Winooski, VT, USA). Their PL decay curves were recorded using a photo-counting TimeHarp 300 system from PicoQuant (Berlin, Germany) with a diode laser emitting at 375 nm (FluoTime 300) as the light source. A Synergy H1 multi-mode monochromatic spectrophotometer from BioTek instruments (Winooski, VT, USA) was used to measure their UV-vis absorption spectra. The Fourier transform infrared (FTIR) spectra of histidine and C dots were recorded using a Varian 640 FTIR spectrophotometer from Varian (Palo Alto, CA, USA). The transmission electron microscopy (TEM) and high-resolution transmission electron microscopy (HRTEM) images of the C dots were acquired using an H-7100 TEM from Hitachi (Tokyo, Japan) and a JSM-1200EX II HRTEM from JEOL (Tokyo, Japan), respectively. The X-ray photoelectron spectroscopy (XPS) measurements were conducted using a K-Alpha X-ray photo electron spectrometer system from Thermo (Waltham, MA, USA). The binding energy values of C dots were calibrated using the C1s signal at 284.6 eV. Their Raman spectra were acquired using an Olympus BX51 microscope and a Nicolet Almega XR dispersive Raman spectrometer from Thermo (Waltham, MA, USA) with a 10 mW laser emitting at 780 nm peak, using the Raman peak of Si wafer (520 cm^{-1}) as a standard. Cyclic voltammetry (CV) curves of phosphate buffer (20 mM, pH 3.0) without and with containing C dots (200 μL) and metal ions (200 μM) were recorded using a CHI 760D electrochemical work station from CH instruments (Austin, TX, USA). A glassy carbon electrode, saturated Ag/AgCl, and Pt wire were used as the working, reference, and counter electrodes, respectively. Electrochemical impedance spectra (EIS) and the Nyquist plots of glassy carbon electrodes in the frequency range of 0.01 to 10000 Hz at an amplitude of 5 mV were recorded using the CHI 760D electrochemical work station in N_2 saturated phosphate buffer (20 mM, pH 3.0) without and with containing C dots (200 μL) and Cu^{2+} ions (200 μM).

2.2.4 Quantitation of Cu^{2+} ions.

Quantitation of Cu^{2+} ions (0–50 μM) using C-dots (0.001X; final concentration) was conducted in phosphate buffer solutions (20 mM) at pH values of 3.0 and 7.0. Linearity, limit of detection, and selectivity were investigated at pH 3.0. To obtain linearity for quantitation of Cu^{2+} ions, aliquots of C dots (0.01X, 100 μL) were added to phosphate buffer solution (25 mM, pH 3.0, 800 μL) prior to addition of Cu^{2+} ions (0–500 μM, 100 μL). The mixtures were equilibrated by shaking at ambient temperature for 60 min, and their PL spectra were recorded when excited at 420 nm. To test the selectivity, C dots (0.1X, 100 μL) were added to phosphate buffer solution (25 mM, 800 μL). Various metal ions (K^+, Mg^{2+}, Ca^{2+}, Mn^{2+}, Fe^{3+}, Co^{2+}, Cu^{2+}, Zn^{2+}, Pb^{2+}, Hg^{2+}, Ag^+; 1 mM, 100 μL) were then added into the resulting solution. The mixtures were equilibrated while shaking at ambient temperature for 60 min, and their PL spectra were recorded with an excitation wavelength of 420 nm. This assay was validated by the analyses of lake and tap water samples that had been collected from National Taiwan

doi:10.6342/NTU202300566

University campus, and sea water sample that had been collected from Keelung coast (East China Sea; Taiwan). Each of the water samples was filtered through a 0.22 μm membrane. Aliquots (100 μL) of the real samples were spiked with various concentrations (0.3-3 μM; final concentrations) of Cu^{2+} ions. Then, phosphate buffer (200 mM, pH 3.0, 100 μL), C dots (0.01X, 100 μL), and ultrapure water were added subsequently to the spiked solutions, each with a final volume of 1.0 mL. The mixtures were equilibrated while shaking at ambient temperature for 60 min, and their PL spectra were recorded under excitation at 420 nm.

2.3 Results and discussion

2.3.1 Formation of C dots

When applying a voltage greater than 1.31 V, oxidation of histidine occurred on the Pt anode, in which the oxidized histidine was adsorbed onto the electrode through its terminal carboxyl group and secondary amino group. Most of the adsorbed molecules were then converted to form imidazoles.[31,32] During the electrolysis course, the solution pH value increased slightly as a result of the formation of NH_3. The adsorbed imidazoles were converted to form C dots through a process of polymerization, carbonization and passivation.[32] The production yield of C dots prepared from amino

doi:10.6342/NTU202300566

acids through a simple electrochemical approach under alkaline than acidic conditions is usually higher.[31] The yields of C dots, Cl-C dots, Br-C dots, and I-C dots are 5.1, 12.3, 15.6 and 33.8%, respectively. The yield of C dots is lower than the other three dots, mainly because they were prepared in the solution containing lower concentration of electrolyte. The yield of I-C dots is the highest, mainly because I^- is a stronger leaving group than Br^- and Cl^-, leading to higher reaction efficiency.

2.3.2 Effect of applied voltage.

Applied voltage affects the electrolysis rate and thus the formation of C dots. At an applied voltage < 1.31 V,[33] C-dots were not formed, mainly because oxidation of histidine did not occur. At a constant electrolysis time (3 min), the PL intensity of the solution increases upon increasing applied voltage from 1 to 10 V as shown in Figure 2-1A. Interestingly, the PL profiles are all similar, revealing that the applied voltage unlikely affect the structure of C-dots. The result reveals that more C dots were formed when applying at a higher voltage for the same reaction time. Considering reaction speed and PL intensity, we selected 10 V for preparation of C dots hereafter. Since the amount of heat and bubbles generated increased upon increasing voltage, a voltage greater than 10 V is not suggested unless a cooling system is applied.

2.3.3 Effect of histidine concentration and pH value.

Figure 2-1B shows the PL spectra of C dots prepared from different concentrations of histidine (0.09-0.90 M) at pH 9.0 and 10 V for 120 min. The PL intensity at 505 nm increases upon increasing the concentration of histidine up to 0.63 M. Further increasing histidine concentration, the PL intensity decreases, mainly because through intermolecular attractions some unreacted histidine molecules formed aggregates and then adsorbed onto the surfaces of C dots, leading to aggregation of C dots. Under the optimal histidine concentration (0.63 M), we tested the effect of pH (3.0-9.0) on the formation of C dots. Figure 2-1C shows that the PL intensity increases upon increasing the pH values from 3.0 to 9.0. Under acidic conditions (pH ~ 3.0), protonated imidazole ring interacts weakly with the Pt anode surface, leading to poor efficiency of oxidation, polymerization, and carbonization. Upon increasing pH value (e.g. pH ~ 5.0), the interaction of histidine with the Pt electrode increases, thus C dots are formed quickly, leading to higher PL than that synthesized at pH 3.0. More C dots are formed and PL further increases upon increasing pH value from 5.0–7.0, simply because the interaction of the adsorbed molecule with the Pt electrode is stronger as a result of increased dissociation degrees of its carboxylic acid group.[34] At pH 9.0, the PL intensity reaches its maximum. The anodic generation of oxygen/or hydroxyl ions accelerates the electrochemical oxidation/or polymerization of the adsorbed molecules, leading to

doi:10.6342/NTU202300566

the formation of C dots with more emissive traps and higher PL intensity.[35] Further increasing pH value, amount of C dots formed increases slightly. Since it is difficult to prepare solution with similar compositions to that at lower pH values, synthesis of C dots at pH > 9.0 was not conducted.

2.3.4 Effect of sodium halides.

It has been reported that addition of sodium halides into amino acid solution enhances its electrochemical oxidation rates due to increased conductivity.[36] We thus investigated the effects of NaCl (0-2.0 M) on formation of C dots under optimal conditions (0.63 M histidine and pH 9.0). Figure 2-1D shows that the PL intensity of Cl-C dots increases upon increasing the NaCl concentration up to 1 M, mainly because of increased reaction rates. At NaCl concentrations greater than 1 M, histidine molecules aggregated as evidenced with the formation of a white solid product. Thus 1 M NaCl was found to be optimal for preparation of C dots. Under similar synthesis conditions, Br-C dots and I-C dots were prepared for comparison of their physicochemical and spectrochemical properties with that of Cl-C dots and C dots. Figure 2-2 shows the TEM images of C dots, Cl-C dots, Br-C dots and, I-C dots. All of the X-C dots were prepared under similar conditions (close ionic strengths). By counting 100 of the four types of C dots, their average sizes were determined to be 3.2

doi:10.6342/NTU202300566

±0.6, 3.9±0.9, 3.8±0.6 and, 4.9±0.7 nm, respectively. The HRTEM images displayed in the insets show each of them having lattices with a d-spacing of 0.31 nm that are consistent with the (002) diffraction planes of sp^2 graphitic carbon. The FTIR spectra (Figure 2-3) were recorded to identify the functional groups on the surfaces of the four types of C dots. The peaks at 2962, 1640, 1462 and 1150 cm^{-1} were assigned to $–CH_2–$, amide I/C=O, amide III/C-N, and C-O stretching vibrations, respectively. The broad bands at around 3320 cm^{-1} suggests the existence of functional groups such as–COOH, –OH, $–NH_2$, $–NH_3^+$ on the surface of all four C dots.[37] The suggestion is supported with their high water dispersibility. The XPS spectra displayed in Figure 2-4 show their C1s spectra, revealing the presence of C–C (284.6 eV), C–I (285.2 eV), C–Br (285.6 eV), C–N/or C–O (286.0 eV), C–Cl (286.6 eV), C=O (286.8 eV), and O–C=O (287.8 eV) bonds.[38,39] Each of their N1s spectra shows four peaks at 398.1 eV, 399.1 eV, 399.8 eV and 400.6 eV, which are attributed to pyridinic N, pyrrolic N, graphitic N, and N–H, respectively.[40] The deconvoluted C1s and N1s spectra support the presence of ring structures and the formation of C dots. Table 2-1 lists the elemental compositions of the as-prepared C dots. Note that the Br-C dots and I-C dots have higher oxygen content than the rest, indicating their greater surface passivation. The Raman spectra of the four types of C dots displayed in Figure 2-5 show the characteristic D- and G-bands at 1311 $cm^{−1}$ and 1531 $cm^{−1}$, which are attributed to the first-order scattering of the E_{2g}

doi:10.6342/NTU202300566

vibration mode in the graphite sheets and the structural defects, respectively.[41] The peak at 1420 cm^{-1} is attributed to the carboxylate groups (COO^{-}).[31] The D-band to G-band ratio (I_D/I_G) of the four types of C dots decreases in the order of I-C dots (0.98) > Br-C dots (0.96) > C dots (0.94) > Cl-C dots (0.90), showing that I-C dots possess the highest density of defects. The result suggests that the halides affect the surface reconstruction processes and defects differently.[42]

Figure 2-6A-C show the effect of sodium halides on the PL of C dots at different excitation wavelengths. As shown in Figure 2-6A, C dots prepared in the absence and presence of 1 M NaCl upon excitation at 280 nm all exhibit one sharp peak at 330 nm and two broad peaks at 445 and 505 nm. The sharp peak at 330 nm is attributed to strong emission from the π–π* transitions in the core.[43] The two broad peaks are attributed mainly to strong emissive contribution from the surface states. The PL intensities of Cl-C dots at 445 and 505 nm are higher than those prepared in the absence of NaCl. Increased NaCl concentration greatly enhanced the oxidation rate of histidine, leading to formation of more strong emissive surface states and thus high PL intensity. Unlike Cl-C dots, the peak at 330 nm for Br-C dots or I-C dots was quenched significantly due to inner effect, greater specific adsorption capacity and greater covalent character of Br^{-}/I^{-} than Cl^{-}.[44] Br-C and I-C dots both show two peaks at 445 and 505 nm, revealing the existence of emissive surface states. Although I^{-} has greater effect on the surface

doi:10.6342/NTU202300566

state, the PL intensities of I-C dots at the two peaks are weaker than that of Cl-C and Br-C dots, mainly because it induces greater PL quenching through intersystem crossing. The quenching efficiency of C dots at 505 nm induced by 1 mM NaI is 43.9 %, which supports our reasoning. As shown in Figure 2-6B, upon excitation at 360 nm, two emission peaks at 445 and 490 nm all were observed in the four types of C dots. Their PL intensities both decrease in the order of Cl-C dots > Br-C dots > C dots > I-C dots because of strong intersystem crossing (heavy-atom effect). As shown in Figure 2-6C, upon excitation at 420 nm, an emission peak at 505 nm was observed, with a decreased order of PL intensity: Cl-C dots > C dots > Br-C dots > I-C dots. The differential PL increasing/decreasing orders at various excitation wavelengths is mainly because the three halides have stronger effects on the surface emission than on the core emission. Figure 2-6D shows the absorption spectra of all four tested C dots solutions and histidine hydrochloride solution. A sharp peak at 220 nm for histidine hydrochloride solution is assigned to its imidazole ring.[45] The peak at 220 nm for Br-C dots and I-C dots undergoes a red shift, mainly due to the absorption of the two halides. The broad absorption over the wavelength range from 300 to 400 nm is attributed to the n–π^* transition of the C＝O bond and the π–π^* transition of the conjugated C＝C b0nd.[24]

doi:10.6342/NTU202300566

2.3.5 Effect of reaction time

To provide more detailed information about the formation of C dots, we investigated the effect of reaction time on the formation of the four types of C dots. Figure 2-7 shows the time-dependence PL intensities of all four C dots when excited at different wavelengths. As shown in Figure 2-7A, upon excitation at 280 nm, the PL of C dots at 330 nm increases gradually and reaches a plateau at around 50 min. Meanwhile the PL of Cl-C dots does not change significantly for the first 20-min period. Instead, it increases gradually and reaches a plateau at 50 min. In both cases, the PL decreases slightly after 50 min and becomes stable after 120 min. The results suggest that Cl^- suppresses the core emission when its content on the Cl-C dots is high. Upon increasing reaction time, the amount of C dots increases, leading to less density of adsorbed Cl^- on the surface of each C dot. Because the emission at 330 nm is small in the Br-C and I-C dots, the effects of Br^- and I^- on their time-evolution PL are hard to be observed. Figure 2-7B compares the PL intensities of the four types of C dots at 445 nm. Besides the PL of I-C dots, the PL intensities from the other three all increased gradually upon increasing reaction time, revealing that more surface states are formed. For I-C dots, the PL increases gradually and reaches a plateau at around 8 min, and then decreases before reaching a constant at around 30 min, mainly because of the formation of I_3^- that has strong absorption bands centered separately at near 280 and 350 nm,

doi:10.6342/NTU202300566

leading to PL quenching of the C dots due to the inner filter effect. The PL of Cl-C dots, Br-C dots and I-C dots are all higher than that of C dots, supporting that the halide affect the surface emission and formation rate of C dots. Besides I-C dots, gradual increased PL intensities were found in the other C dots when excited at 360 or 420 nm (Figure 2-7C-F). Because of having stronger effects on the surface defects and intersystem crossing of iodide, the PL intensities of I-C dots decrease once they reach their maxima. Interestingly, all the three C dots prepared in the presence of sodium halides show detectable PL within 1 min electrolysis when excited at 360 or 420 nm (Figure 2-7C-F). Also displayed in the insets of Figure 2-7C-F are their time-dependent UV-vis absorption spectra. The sharp peak at 220 nm for each of the four C dots is assigned to that of imidazole ring.[45] Upon increasing the electrolysis time, the peak of Br-C dots or I-C dots at 220 nm undergoes a red shift due to increased absorption of Br_2 or I_2 as a result of increases in their formation amounts. The absorbance values over 300 to 400 nm increases upon increasing the reaction time, mainly because of gradual increases in the formation of C dots. Table 1 reveals negligible differences in the PL lifetimes (excitation wavelength/emission wavelength: 375/440 nm) of C dots, Cl-C dots, Br-C dots and I-C dots regardless of the reaction times. The lifetime data support iodide induced greater intersystem crossing. Besides I- C dots, the other three types of C dots obtained after 60 min have slightly longer lifetimes, mainly because of increases in their

doi:10.6342/NTU202300566

surface oxidation with oxygen.

2.3.6 Formation routes.

Scheme 1 summarizes the formation of C dots from histidine at pH 9.0. After adsorption of histidine onto the anodic Pt electrode, histidine undergoes an electrochemical oxidation to form imidazole. Subsequently, the adsorbed imidazole is through a process of polymerization, carbonization, and passivation to form C dots. As shown in Scheme 1 the solution color changes can be easily observed by the naked eye. The solution becomes darker upon increasing reaction time, mainly because greater amounts of C-dots and larger aggregates (particles) of C dots are formed. Oxidation also occurs to change their surface states. Addition of the halides to the reaction solution increases the conductivity and thus the electrolysis rate. In addition, the halides also induce formation of greater surface defects. Their different nucleophilic substitution rates, specific adsorption capacity, and migration/or diffusion rates are also responsible for the formation of different C dots.[46]

2.3.7 Sensitivity and selectivity.

To test analytical applications of the four C-dots, their stability in aqueous solutions at different pH values (3.0-11.0) was tested. As displayed in Figure 2-8A, they are all stable in the tested pH region. The main reason for choosing the excitation/emission wavelengths of 420/505 nm is because the optical properties are related to the surface defects of the C dots and are expected to be more sensitive to an environmental change. Figure 2-8B shows their high salt tolerance; stable up to 3 M NaCl. The results reveal their potential in analytical applications. Because histidine has high specificity towards Cu^{2+} (formation constant K $= \mathbf{2.34 \times 10}^{10}$ at pH 4.0),[47] we used the as-prepared C dots to detect Cu^{2+} ions. Cu^{2+} plays important roles in many biological functions, while at high concentrations also potentially causes some diseases such as gastrointestinal disorders, liver/kidney damage.[48-50] Although the sensitivity for the detection of Cu^{2+} is slightly higher at pH 7.0 than at 3.0, mainly because Cu^{2+} ions interact more strongly with the adsorbed histidine and the surface functional groups such as amino and carboxylate, interference from Zn^{2+} ions are seriously at pH > 3.0. In addition, formation of metal oxides is another disadvantage. On the other hand, poor sensitivity and less stability of C dots at pH < 3.0 are disadvantageous.

To evaluate selectivity of the four C dots toward Cu^{2+} at pH 3.0, we determined their relative PL intensity $[(I_F - I_{Fo})/I_{Fo}]$ at 505 nm in the presence of different metal ions when excited at a wavelength of 420 nm. Figure 2-9 shows the selectivity of all four tested C dots toward various metal ions at a concentration of 100 μM. Cu^{2+}, Hg^{2+},

doi:10.6342/NTU202300566

and Ag^+ all induced significant PL quenching of the four types of C dots. To mask the interferences from Hg^{2+} and Ag^+ ions, NaI was added. The solubility products (K_{sp}) values of Hg_2I_2 and AgI are 4.6 x 10^{-29} and 8.3 x 10^{-17}, respectively, which are much higher than that (1.0 x 10^{-12}) of CuI. To minimize interference from Ni^{2+}, in addition to NaI, citric acid that can form stroner complexes with Ni^{2+} over Cu^{2+} was added.[51] In the presence of 0.8 mM NaI and 1 mM of citric acid, I-C dot probe provides high selectivity toward Cu^{2+} ions (100 μM) over the potential interfering metal ions (100 μM) as shown in Figure 2-10A. We note that the other three types of C dots also can be used for selective detection of Cu^{2+} ions, with slighly higher interference from some potential interfering species such as Fe^{3+}. Hereafter, we only discuss quantitation of Cu^{2+} using I-C dots.

Figure 2-10B shows the relative PL intensity of I-C dots decreases upon increasing Cu^{2+} ions over the concentration range of 0–50 μM. The Cu^{2+} induced PL quenching is mainly through an electron transfer process.[52] The quenching efficiencies of C dots and I-C dots induced by 100 μM Cu^{2+} are 65.2 % and 65.6 %, respectively, ruling out strong interaction of the surface iodides with Cu^{2+}. The I-C dots probe exhibits linearity toward Cu^{2+} ions over the concentration range of 0.3-3 μM (R^2 = 0.98), with a limit of detection (LOD) of 0.22 μM at a signal-to-noise ratio 3. The LOD is lower than the tolerance level (20 μM) of Cu^{2+} ions in drinking water defined by US Environmental

Protection Agency (EPA).[4] Table 2-3 lists the linear ranges and the LODs of different nanomaterials based probes toward the quantitation of Cu^{2+} ions, showing a lower LOD provided by the I-C dots than that by the rest.[53-60] In addition, organic solvent is not required when applying this simple assay. Having high selectivity and low LOD, the I-C dot probe holds great potential for the quantification of Cu^{2+} ions in real samples containing complex matrixes.

2.3.8 Sensing mechanism.

To provide more information about the specificty of I-C dots toward Cu^{2+} ions, a simple and sensitive electrochemical tool (CV) was applied. Bare GCE exhibits a featureless CV curve over the potential range from -0.6 to 0.8 V in the presence of I-C dots (1 mL) as shown in Figure 2-11A. Faradaic or non-Faradaic reactions did not occur even when CVs were recorded in a wide potential window (-0.6–1.3 V), revealing that the active binding sites did not contribute to the electron transfer or double layer capacitance. In a solution containing I-C dots and Fe^{3+} ions, oxidation or reduction peaks of Fe^{3+} ions were not detected. After spiking Cu^{2+} ions (100 µM) into the solution, two reduction peaks at *ca.* −0.1 and −0.31 V and one oxidation peak at *ca.* 0.1 V appeared.[61] Peaks at -0.31 and 0.1 V are attributed to the reduction and oxidation of Cu-histidine complexes, respectively. Upon increasing Cu^{2+} concentrations, the reduction peaks shifted to more negative potentials, revealing that Cu^{2+} ions were

doi:10.6342/NTU202300566

reduced to metallic copper (Cu^0) at *ca.* −0.1 V. To identify the interfacial changes during the formation of the complex, EIS measurements were conducted. The Nyquist plot of a bare GCE recorded in the presence of I-C dots with N_2 purging is displayed in Figure 2-11B. The bare GCE exhibits a small arc in the high frequency region due to strong adsorption of I-C dots on the electrode surface. The arc diameter becomes smaller in the presence of Cu^{2+} as a result of improved charge transfer. CV and EIS results revealed the plausible binding sites of Cu^{2+} ions in I-C dots and the reduction of Cu^{2+} ions to form the metallic copper, supporting our proposed sensing mechanism. As shown in Table 2-1, the oxygen content of I-C dots increased significantly after being reacted with Cu^{2+} ions. As depicted in Figure 2-3, the characteristic absorption peaks at 1640 cm^{-1} and 1596 cm^{-1} disappeared after being reacted with Cu^{2+} ions, revealing the oxidation of amide I groups on the surface of I-C dots.[62] Two new bands at 1289 and 2383 cm^{-1} are ascribed to the C-O and CO_2 stretching vibrations, which revealed that the surface functional groups of I-C dots were oxidized. The $2p_{3/2}$ and $2p_{1/2}$ peaks at 932.3 and 952.1 eV in the Cu 2p spectrum are attributed to the metallic copper, respectively (Figure 2-4).[63] There is a small characteristic satellite peak around 942.0 eV for Cu $2p_{3/2}$, which indicates some unreacted copper ions were bound onto the surface of I-C dots. All these results confirm that the I-C dots were oxidized by the surface Cu^{2+} ions/complexes and metallic copper was formed on the surface of I-C

doi:10.6342/NTU202300566

dots.

2.3.9 Real sample analysis.

Practicality of the I-C dot probe was validated through the determination of the concentrations of Cu^{2+} ions in various real samples, including tap water, lake water and sea water, using a standard addition method. Figure 2-12 shows good linearity (R^2 = 0.98) of relative PL intensity $[(I_{F0} - I_F)/I_{F0}]$ responses at 505 nm toward spiked Cu^{2+} ions over the concentrations range from 0.3 to 3 μM. There was no obvious difference in the linearity and the slope among the three samples, revealing negligible matrix effects. Having high sensitivity and selectivity, this probe is useful for quantitation of Cu^{2+} ions in water samples.

2.4 Conclusions

A simple and cost-effective electrochemical approach was applied to prepare C dots from histidine under alkaline conditions, which allows one to gain more information about the formation of C dots. Upon increasing reaction time, more C dots were formed. Because the formation speed of C dots increases upon increasing electrolysis rate, larger amounts of C-dots can be prepared in a short period of time

doi:10.6342/NTU202300566

from precursors in high-conductivity media at a high voltage using a large electrode. When compared to hydrothermal routes, this electrochemical approach produces much less amount of large particles. Halides induce surface defects, leading to enhanced surface emission intensity, but they also cause PL quenching through intersystem crossing. Having a high sensitivity and selectivity, the I-C dot probe holds great potential for quantitation of Cu^{2+} in complicated samples.

2.5 References

[1] Z.X. Liu, B.B. Chen, M.L. Liu, H.Y. Zou, C.Z. Huang, Cu(i)-Doped carbon quantum dots with zigzag edge structures for highly efficient catalysis of azide–alkyne cycloadditions, Green Chem., 19 (2017) 1494–1498.

[2] H. Jin, , R. Gui J. Gong, W. Huang, Aptamer and 5-fluorouracil dual-loading Ag2S quantum dots used as a sensitive label-free probe for near-infrared photoluminescence turn-on detection of CA125 antigen, Biosens. Bioelectron., 92 (2017) 378–384.

[3] W.-Y. Chen, C.-C. Huang, L.-Y. Chen, H.-T. Chang, Self-assembly of hybridized ligands on gold nanodots: tunable photoluminescence and sensing of nitrite, Nanoscale 6 (2014) 11078–11083.

[4] G.-Y. Lan, C.-C. Huang, H.-T. Chang, Silver nanoclusters as fluorescent probes for selective and sensitive detection ofcopper ions, Chem. Commun. 46 (2010) 1257–1259.

[5] J. Feng, W.J. Wang, X. Hai, Y.L. Yu, J.H, Wang, Green preparation of nitrogen-doped carbon dots derived from silkworm chrysalis for cell imaging, J. Mater. Chem. B, 4 (2016) 387–393.

doi:10.6342/NTU202300566

[6] P.-C. Hsu, Z.-Y. Shih, C.-H. Lee, H.-T. Chang, Synthesis and analytical applications of photoluminescent carbon nanodots, Green Chem. 14 (2012) 917–920.

[7] H. Nie, M. Li, Q. Li, S. Liang, Y. Tan, L. Sheng, W. Shi, S.X.A. Zhang, Carbon Dots with Continuously Tunable Full-Color Emission and Their Application in Ratiometric pH Sensing, Chem. Mater. 26 (2014) 3104−3112.

[8] S. Liu, J. Tian, L. Wang, Y. Zhang, X. Qin, Y. Luo, A. M. Asiri, A.M.A.O. Al-Youbi, X. Sun, Hydrothermal Treatment of Grass: A Low-Cost, Green Route to Nitrogen-Doped, Carbon-Rich, Photoluminescent Polymer Nanodots as an Effective Fluorescent Sensing Platform for Label-Free Detection of Cu(II) Ions, Adv. Mater. 24 (2012) 2037–2041.

[9] X. Wang, K. Qu, B. Xu, J. Ren, X. Qu, Microwave assisted one-step green synthesis of cell-permeable multicolor photoluminescent carbon dots without surface passivation reagents, J. Mater. Chem. 21 (2011) 2445–2450.

[10] L. Ma, W. D. Xiang, H.H. Gao, J. Wang, Y. Ni, X. Liang, Facile synthesis of tunable fluorescent carbon dots and their third-order nonlinear optical properties, Dyes Pigm. 128 (2016) 1–7.

doi:10.6342/NTU202300566

[11] H. Li, X. He, Z. Kang, H. Huang, Y. Liu, J. Liu, S. Lian, C.H.A. Tsang, X. Yang, S.T. Lee, Water-Soluble Fluorescent Carbon Quantum Dots and Photocatalyst Design, Angew. Chem. Int. Ed. 49 (2010) 4430–4434.

[12] D. Pan, J. Zhang, Z. Li, M. Wu, Hydrothermal Route for Cutting Graphene Sheets into Blue-Luminescent Graphene Quantum Dots, Adv. Mater. 22 (2010) 734–738.

[13] G.E. LeCroy, F. Messina, A. Sciortino, C.E. Bunker, P. Wang, S.K.A. Fernando, Y. P. Sun, Characteristic Excitation Wavelength Dependence of Fluorescence Emissions in Carbon “Quantum” Dots, J. Phys. Chem. C 121 (2017) 28180–28186.

[14] V. Strauss, J.T. Margraf, C. Dolle, B. Butz, T.J. Nacken, J. Walter, W. Bauer, W. Peukert, E. Spiecker, T. Clark, D.M. Guldi, Carbon Nanodots: Toward a Comprehensive Understanding of Their Photoluminescence, J. Am. Chem. Soc. 136 (2014) 17308–17316.

[15] Y.P. Sun, B. Zhou, Y. Lin, W. Wang, K.A.S. Fernando, P. Pathak, M.J. Meziani, B. A. Harruff, X. Wang, H. Wang, P.G. Luo, H. Yang, M.E. Kose, B. Chen, L.M. Veca, S.Y. Xie, Quantum-Sized Carbon Dots for Bright and Colorful Photoluminescence, J. Am. Chem. Soc., 128 (2006) 7756–7757.

doi:10.6342/NTU202300566

[16] Q.L. Zhao, Z.L. Zhang, B.H. Huang, J. Peng, M. Zhang, D.W. Pang, Chem. Commun. Facile preparation of low cytotoxicity fluorescent carbon nanocrystals by electrooxidation of graphite, Chem. Commun. 0 (2008) 5116–5118.

[17] J. Niu, H. Gao, J. Lumin. Synthesis and drug detection performance of nitrogen-doped carbon dots, 149 (2014) 159–162.

[18] Z. Ma, H. Ming, H. Huang, Y. Liu, Z. Kang, One-step ultrasonic synthesis of fluorescent N-doped carbon dots from glucose and their visible-light sensitive photocatalytic ability, New J. Chem., 36 (2012) 861-864.

[19] V.N. Mehta, S. Jha, R.K. Singhal, S.K. Kailasa, Preparation of multicolor emitting carbon dots for HeLa cell imaging, New J. Chem. 38 (2014) 6152–6160.

[20] S.Y. Park, C.Y. Lee, H.-R. An, H. Kim, Y.-C. Lee, E.C. Park, H.-S. Chun, H.Y. Yang, S.-H. Choi, H.S. Kim, K.S. Kang, H.G. Park, J.-P. Kim, Y. Choi, J. Lee, H.U. Lee, Advanced carbon dots via plasma-induced surface functionalization for fluorescent and bio-medical applications, Nanoscale, 9 (2017) 9210-9217

[21] P.-C. Hsu, H.-T. Chang, Synthesis of high-quality carbon nanodots from hydrophilic compounds: role of functional groups, Chem. Commun. 48 (2012) 3984–3986.

doi:10.6342/NTU202300566

[22] A.B. Bourlinos, A. Stassinopoulos, D. Anglos, R. Zboril, V. Georgakilas, E.P. Giannelis, Photoluminescent Carbogenic Dots, Chem. Mater. 20 (2008) 4539–4541.

[23] S. Mitra, S. Chandra, T. Kundu, R. Banerjee, P. Pramanik, A. Goswami, Rapid microwave synthesis of fluorescent hydrophobic carbon dots, RSC Adv. 2 (2012) 12129-12131.

[24] X. Jia, J. Li, E. Wang, One-pot green synthesis of optically pH-sensitive carbon dots with upconversion luminescence, Nanoscale 4 (2012) 5572−5575.

[25] P.-C. Hsu, P.-C. Chen, C.-M. Ou, H.-Y. Chang. H.-T. Chang., Extremely high inhibition activity of photoluminescent carbon nanodots toward cancer cells, J. Mater. Chem. B 1 (2013) 1774–1781.

[26] C.-L. Li, C.-M. Ou, C.-C. Huang, W.-C. Wu, Y.-P. Chen, T.-E. Lin, L.-C. Ho, C.-W. Wang, C.-C. Shih, H.-C. Zhou, Y.-C. Lee, W.-F. Tzeng, T.-J. Chiou, S.-T. Chu, J. Cangm, H.-T. Chang, Carbon dots prepared from ginger exhibiting efficient inhibition of human hepatocellular carcinoma cells, J. Mater. Chem. B 2 (2014) 4564–4571.

[27] Y.S. Liu, Y.N. Zhao, Y.Y. Zhang, One-step green synthesized fluorescent carbon nanodots from bamboo leaves for copper(II) ion detection, Sens. Act. B 196 (2014) 647−652.

doi:10.6342/NTU202300566

[28] B.S.B. Kasibabu, S.L. D'souza, S. Jha, R.K. Singhal, H. Basu, S.K. Kailasa, One-step synthesis of fluorescent carbon dots for imaging bacterial and fungal cells, Anal. Methods 7 (2015) 2373–2378.

[29] S. Sahu, B. Behera, T.K. Maiti, S. Mohapatra, Simple one-step synthesis of highly luminescent carbon dots from orange juice: application as excellent bio-imaging agents, Chem. Commun. 48 (2012) 8835–8837.

[30] V.N. Mehta, S. Jha, H. Basu, R.K. Singhal, S.K. Kailasa, One-step hydrothermal approach to fabricate carbon dots from apple juice for imaging of mycobacterium and fungal cells, Sens. Act. B. 213 (2015) 434–443.

[31] C.-I. Wang, W.-C. Wu, A.P. Periasamy, H.-T. Chang, Electrochemical synthesis of photoluminescent carbon nanodots from glycine for highly sensitive detection of hemoglobin, Green Chem. 16 (2014) 2509–2514.

[32] K. Ogura, M. Kobayashi, M. Nakayama, Y. Miho, In-situ FTIR studies on the electrochemical oxidation of histidine and tyrosine, J. Electroanal. Chem. 463 (1999) 218–223.

[33] D.M. Close, P. Wardman, Calculation of Standard Reduction Potentials of Amino Acid Radicals and the Effects of Water and Incorporation into Peptides, J. Phys. Chem. A 122 (2018) 439–445.

doi:10.6342/NTU202300566

[34] S. Li, M. Hong, Protonation, Tautomerization, and Rotameric Structure of Histidine: A Comprehensive Study by Magic-Angle-Spinning Solid-State NMR, J. Am. Chem. Soc. 133 (2011) 1534–1544.

[35] N.L. Weinberg, H.R. Weinberg, Electrochemical oxidation of organic compounds, Chem. Rev. 68 (1968) 449–523.

[36] M.R. Thombare, G. S. Gokavi, Kinetics and mechanism of oxidation of glycine and alanine by Oxone® catalyzed by bromide ion, J. Braz. Chem. Soc. 25 (2014) 1545–1551.

[37] J. Jiang, Y. He, S. Li, H. Cui, Amino acids as the source for producing carbon nanodots: microwave assisted one-step synthesis, intrinsic photoluminescence property and intense chemiluminescence enhancement, Chem. Commun. 48 (2012) 9634−9636.

[38] M. Patel, W. Feng, K. Savaram, M.R. Khoshi, R. Huang, J. Sun, E. Rabie, C. Flach, R. Mendelsohn, E. Garfunkel, H. He, Microwave Enabled One-Pot, One-Step Fabrication and Nitrogen Doping of Holey Graphene Oxide for Catalytic Applications, Small 11 (2015) 3358–3368.

[39] X.L. Zhou, F. Solymosi, P.M. Blass, K.C. Cannon, J.M. White, Interactions of methyl halides (Cl, Br and I) with Ag(111), Surf. Sci. 219 (1989) 294–316.

[40] Z. Liu, Y. Yang, Z. Du, W. Xing, S. Komarneni, Z. Zhang, X. Gao, Z. Yan, Furfuralcohol Co-Polymerized Urea Formaldehyde Resin-derived N-Doped Microporous Carbon for CO2 Capture, Nanoscale Res. Lett. 10 (2015) 333–343.

[41] Y.Q. Dong, L.S. Wan, J.H. Cai, Q.Q. Fang, Y.W. Chi, G.N. Chen, Natural carbon-based dots from humic substances, Sci. Rep. 5 (2015) 10037.

[42] J.C. Charlier, Defects in Carbon Nanotubes, Acc. Chem. Res. 35 (2002) 1063–1069.

[43] J. Schneider, C.J. Reckmeier, Y. Xiong, M.V. Seckendorff, A.S. Andrei S. Susha, P. Kasák, A.L. Rogach, Molecular Fluorescence in Citric Acid-Based Carbon Dots, J. Phys. Chem. C 121 (2017) 2014−2022.

[44] K. Ogura, Electrochemical reduction of carbon dioxide to ethylene: Mechanistic approach, Journal of CO2 Utilization 1 (2013) 43–49.

[45] L.J. Saidel, A.R. Goldfarb, S. Waldman, The absorption spectra of amino acids in the region two hundred to two hundred and thirty millimicrons, J. Biol. Chem. 197 (1952) 285–291.

[46] H. Wang B. C.W. Gu, D.W. Lee, J.S. Lee, Effect of halide-mixing on the switching behaviors of organic-inorganic hybrid perovskite memory, Sci. Rep. 7 (2017) 43794.

[47] R. Leberman, B.R. Rabin, Metal complexes of histidine, Trans. Faraday Soc. 55 (1959) 1660 –1670.

[48] D.G. Barceloux, D. Barceloux, J. Toxicol., Copper, Clin. Toxicol, 37(2) (1999) 217–230.

[49] M. Olivares, R. Uauy, Copper as an essential nutrient, Am. J. Clin. Nutr. 63 (1996) 791S-6S.

[50] P.G. Georgopoulos, A. Roy, M.J. Yonone-Lioy, R.E. Opiekun, P.J. Lioy, Environmental copper: its dynamics and human exposure issues, J. Toxicol. Environ. Health, Part B, 4 (2001) 341–394.

[51] O.Y. Zelenin, Interaction of the Ni^{2+} ion with citric acid in an aqueous solution, Russ J Coord Chem, 33 (2007) 346–350.

[52] J.Q. Tian, Q. Liu, A.M. Asiri, A.O. Al-Yubi, X.P. Sun, Ultrathin graphitic carbon nitride nanosheet: a highly efficient fluorosensor for rapid, ultrasensitive detection of Cu(2+), Anal., Chem. 85 (2013) 5595–5599.

[53] A. Zhu, Q. Qu, X. Shao, B. Kong, Y. Tian, Carbon-Dot-Based Dual-Emission Nanohybrid Produces a Ratiometric Fluorescent Sensor for In Vivo Imaging of Cellular Copper Ions, Angew. Chem. Int. Ed., 124 (2012) 7297–7301.

doi:10.6342/NTU202300566

[54] M. Koneswaran, R. Narayanaswamy, RETRACTED: l-Cysteine-capped ZnS quantum dots based fluorescence sensor for Cu^{2+} ion, Sens. Act. B. 139 (2009) 104–109.

[55] G. He, C. Liu, X. Liu, Q. Wang, A. Fan, S. Wang, X. Qian, Design and synthesis of a fluorescent probe based on naphthalene anhydride and its detection of copper ions, PloS one. 12 (2017) e0186994.

[56] M.C. Rong, K.X. Zhang, Y.R. Wang, X. Chen, The synthesis of B, N-carbon dots by a combustion method and the application of fluorescence detection for Cu^{2+}, Chin. Chem. Lett. 28 (2017) 1119–1124.

[57] C. Boonme, T. Noipa, T. Tuntulani, W. Ngeontae, Cysteamine capped CdS quantum dots as a fluorescence sensor for the determination of copper ion exploiting fluorescence enhancement and long-wave spectral shifts, Spectrochim. Acta Mol. Biomol. Spectrosc. 169 (2013) 161–168.

[58] X.F. Hou, F. Zeng, F.K. Du and S.Z. Wu, Nanotechnology, Carbon-dot-based fluorescent turn-on sensor for selectively detecting sulfide anions in totally aqueous media and imaging inside live cells, 24 (2013) 335502.

[59] Y. Wang, W.-T. Wu, M.-B. Wu, H.-D. Sun, H. Xie, C. Hu, X.-Y. Wu and J.-H. Qiu, Yellow-visual fluorescent carbon quantum dots from petroleum coke for the efficient detection of Cu2+ ions, New Carbon Mater. 30 (2015) 550–559.

[60] L. Zhao, H. Li, Y. Xu, H. Liu, T. Zhou, N. Huang, Y. Li and L. Ding, Selective detection of copper ion in complex real samples based on nitrogen-doped carbon quantum dots, Anal. Bioanal. Chem. 410 (2018) 4301–4309.

[61] Y.C. Weng, T.H. Cheng, Electrochemical behavior of Cu^{2+}-histidine complexes on a gassy carbon electrode, Naturforsch. 66 (2011) 279 – 288.

[62] G. Oza, K. Oza, S. Pandey, S. Shinde, A. Mewada, M. Thakur, M. Sharon, M. Sharon, A Green Route Towards Highly Photoluminescent and Cytocompatible Carbon dot Synthesis and its Separation Using Sucrose Density Gradient Centrifugation, J Fluoresc. 25 (2015) 9–14.

[63] Y.-J. Lin,, P.-C. Chen Z. Yuan, J.-Y. Ma, H.-T. Chang, The isomeric effect of mercaptobenzoic acids on the preparation and fluorescence properties of copper nanoclusters, Chem. Commun. 51 (2015) 11983–11986.

Table 2-1. Elemental compositions (%) of four types of C dots before and after reaction with Cu^{2+} ions.

Elements	C dots	Cl-C dots	Br-C dots	I-C dots	I-C dots + Cu^{2+}
C	68.79	66.40	57.00	59.70	44.84
N	14.52	15.35	17.73	15.30	6.50
O	16.33	17.61	23.96	23.33	47.15
I	-[a]	-	-	1.46	0.55
Br	-	-	0.95	-	-
Cl	0.37	0.64	0.23	0.21	0.22

[a] not detected

Table 2-2. PL lifetimes of four different types of C dots determined at different time periods of electrolysis.

Nanomaterials	$\tau_{1\ \mathrm{min}}$ (ns)	$\tau_{30\ \mathrm{min}}$ (ns)	$\tau_{60\ \mathrm{min}}$ (ns)	$\tau_{120\ \mathrm{min}}$ (ns)
C dots	5.57	4.92	4.83	5.05
Cl-C dots	4.58	4.71	4.45	4.54
Br-C dots	4.51	4.89	4.72	4.84
I-C dots	4.29	4.40	4.01	3.91

doi:10.6342/NTU202300566

Table 2-3. Quantitation of Cu^{2+} ions using different nanomaterial probes.

Probe	Linear range (μM)	LOD (μM)	Ref.
[a]CdSe@C-TPEA	1-100	1	53
[b]ZnS QDs	26-260	7.1	54
[c]Probe L	4-12	1.8	55
[d]B, N-C dots	1-25	0.3	56
Cys-CdS QDs	2-10	1.5	57
C dots	5.16-20	1.72	58
Petroleum coke C dots	0.25-10	0.029	59
N-C dots	0.6-30	0.19	60
I-C dots	0.3-3	0.22	This study

[a] TPEA: N-(2-aminoethyl)-N,N,N'tris(pyridin-2-ylmethyl)ethane-1,2-diamine.

[b] QDs: quantum dots.

[c] Probe L prepared from 4-bromo-1,8 naphthalene anhydride and 2-thiophene formaldehyde.

[d] B, N-C dots prepared from aminophenylboronic acid

doi:10.6342/NTU202300566

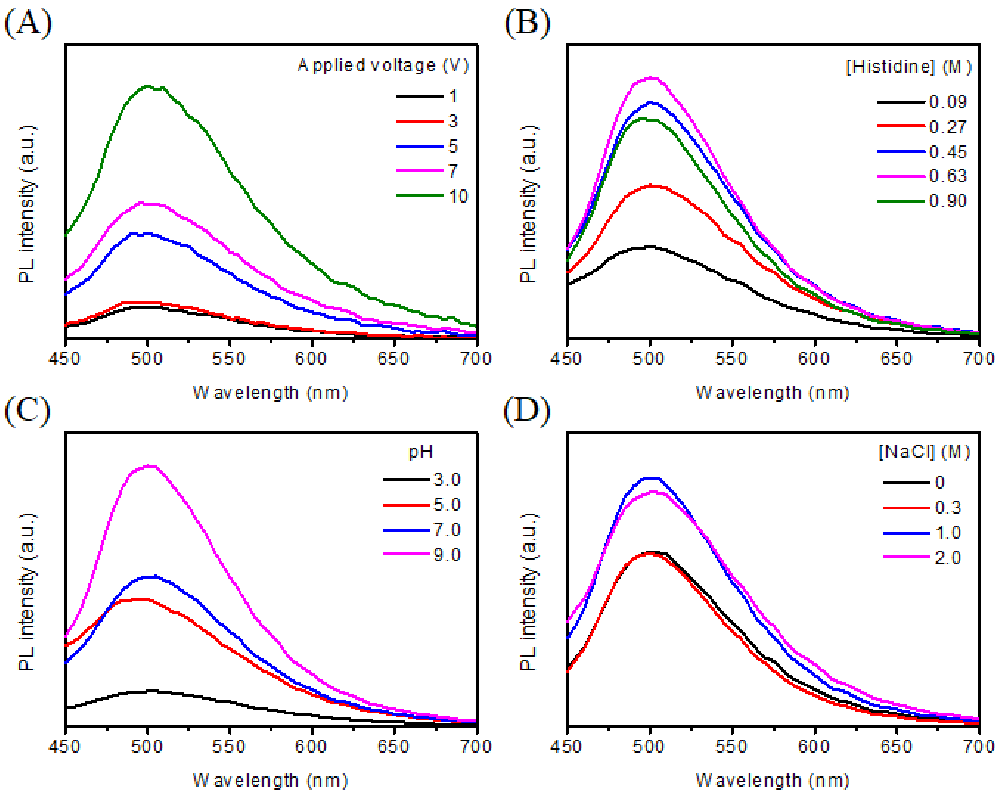

Figure 2-1. Effects of (A) applied voltage, (B) histidine concentration, (C) pH, and (D) NaCl concentration on the formation of C dots at 10 V for 2 h. Excitation and emission wavelengths are 420 nm and 505 nm, respectively. (A) 0.63 M histidine at pH 9.0; (B) 1 M NaCl at pH 9.0; (C) 0.63 M histidine and 1 M NaCl; (D) 0.63 M histidine at pH 9.0.

doi:10.6342/NTU202300566

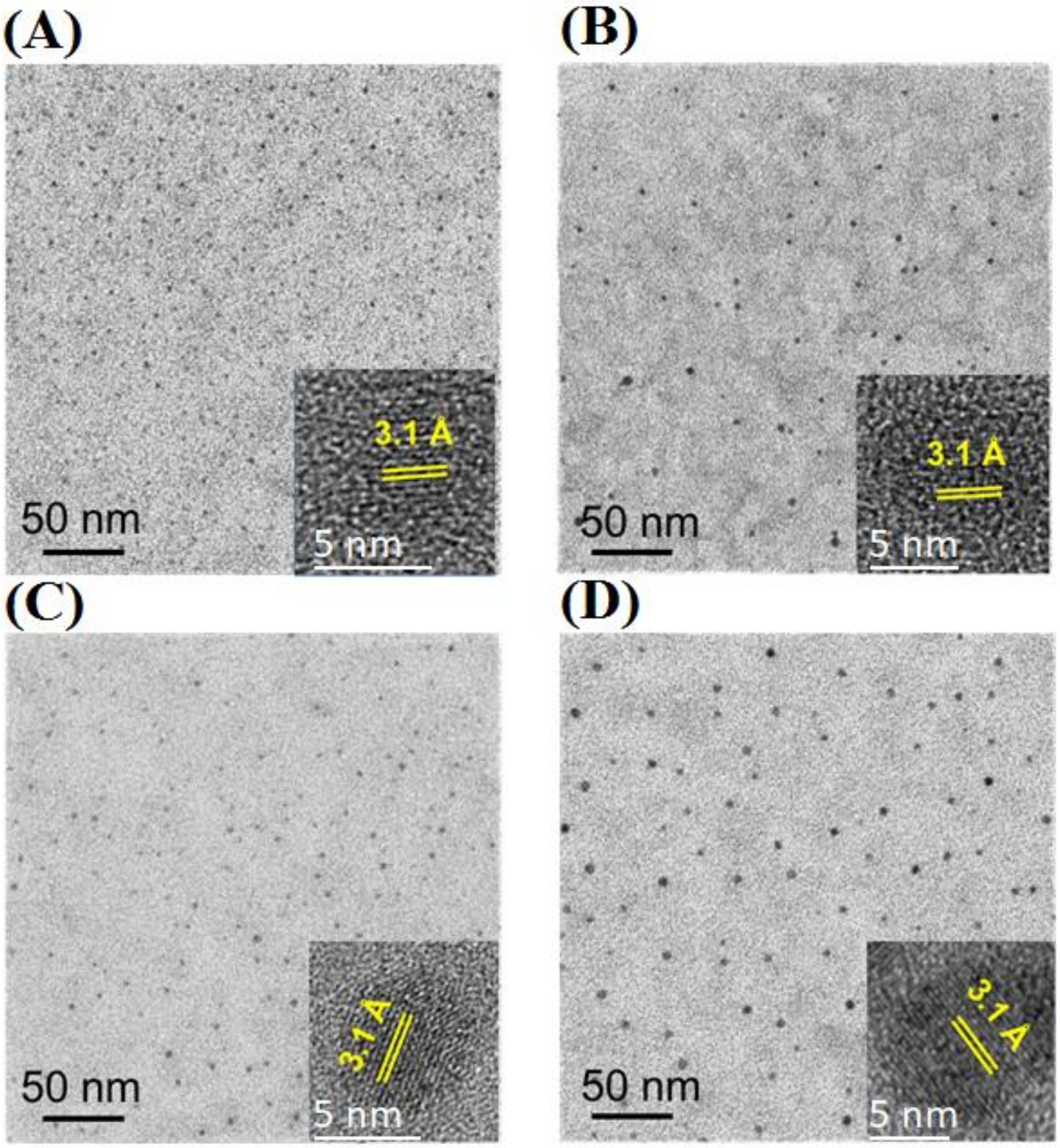

Figure 2-2. TEM images of (A) C dots, (B) Cl-C dots, (C) Br-C dots, and (D) I-C dots.

Insets: HRTEM images of the corresponding C dots.

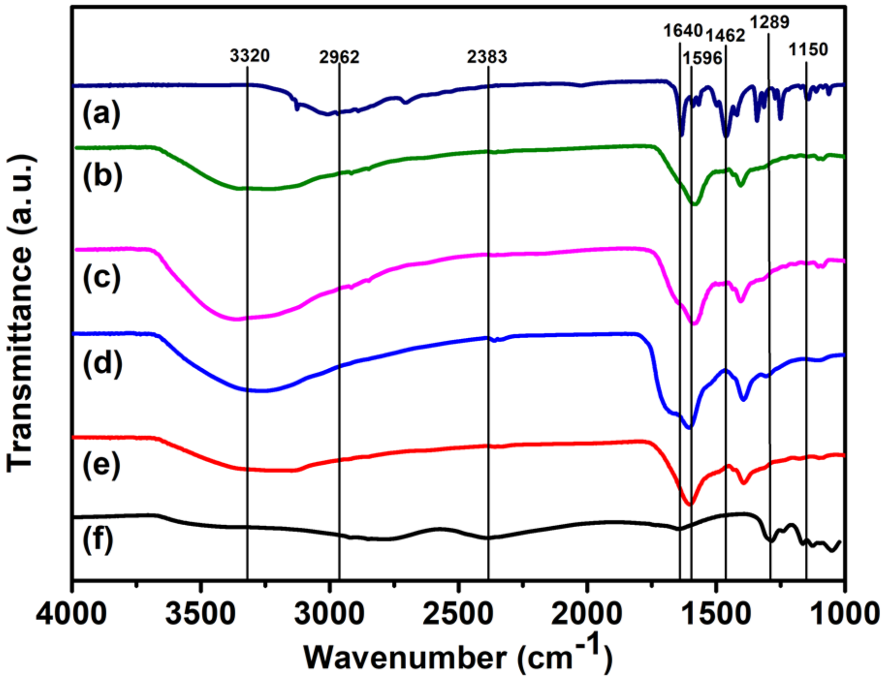

Figure 2-3. FTIR spectra of (a) histidine, (b) C dots, (c) Cl-C dots, (d) Br-C dots, (e) I-C dots, and (f) I-C dots after reaction with 100 μM Cu^{2+} ions.

doi:10.6342/NTU202300566

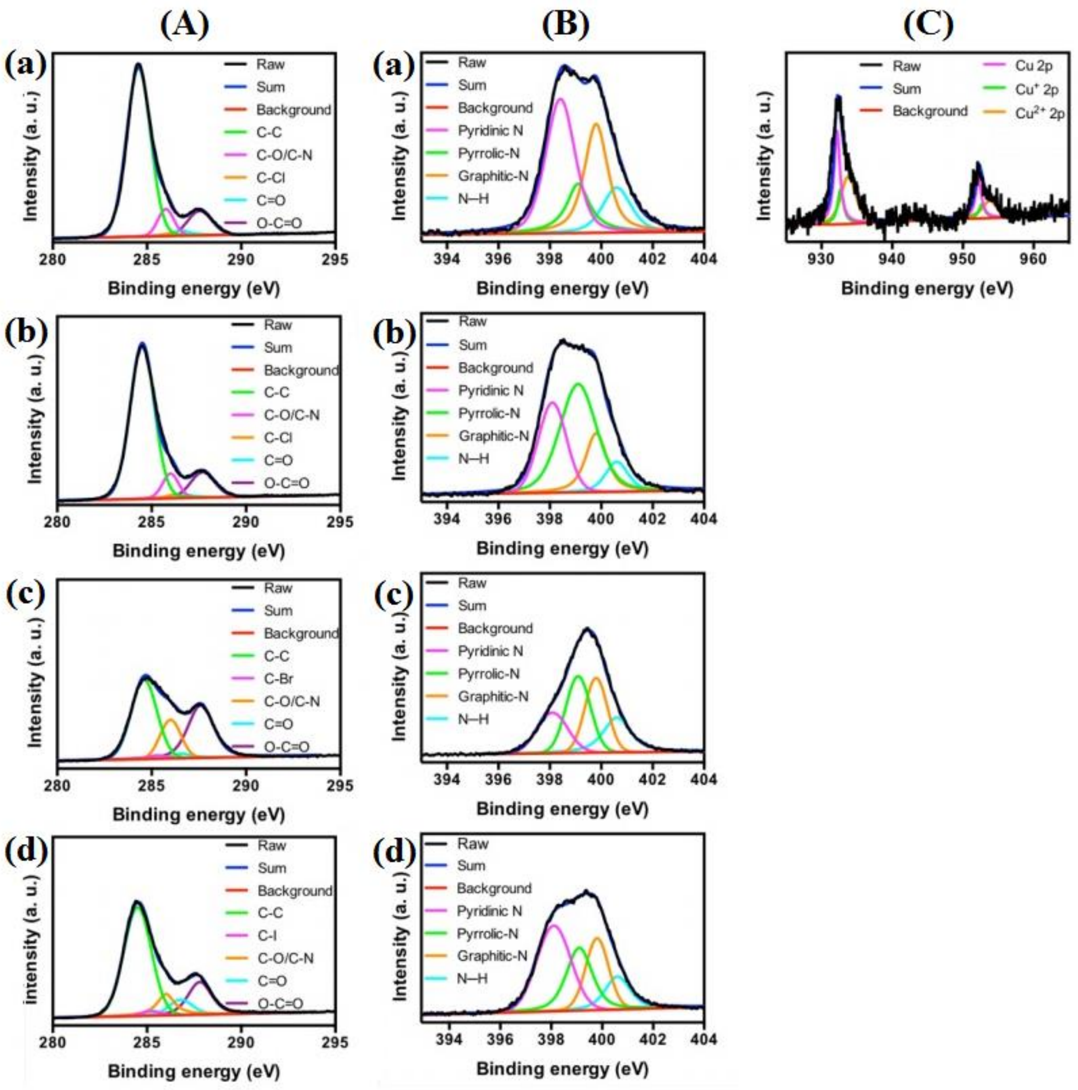

Figure 2-4. Deconvoluted (A) C1s and (B) N1s core level XPS spectra of (a) C dots, (b) Cl-C dots, (c) Br-C dots, and (d) I-C dots. (C) Deconvoluted $Cu_{2p3/2}$ core level spectra of I-C dots after reaction with 100 μM Cu^{2+} ions.

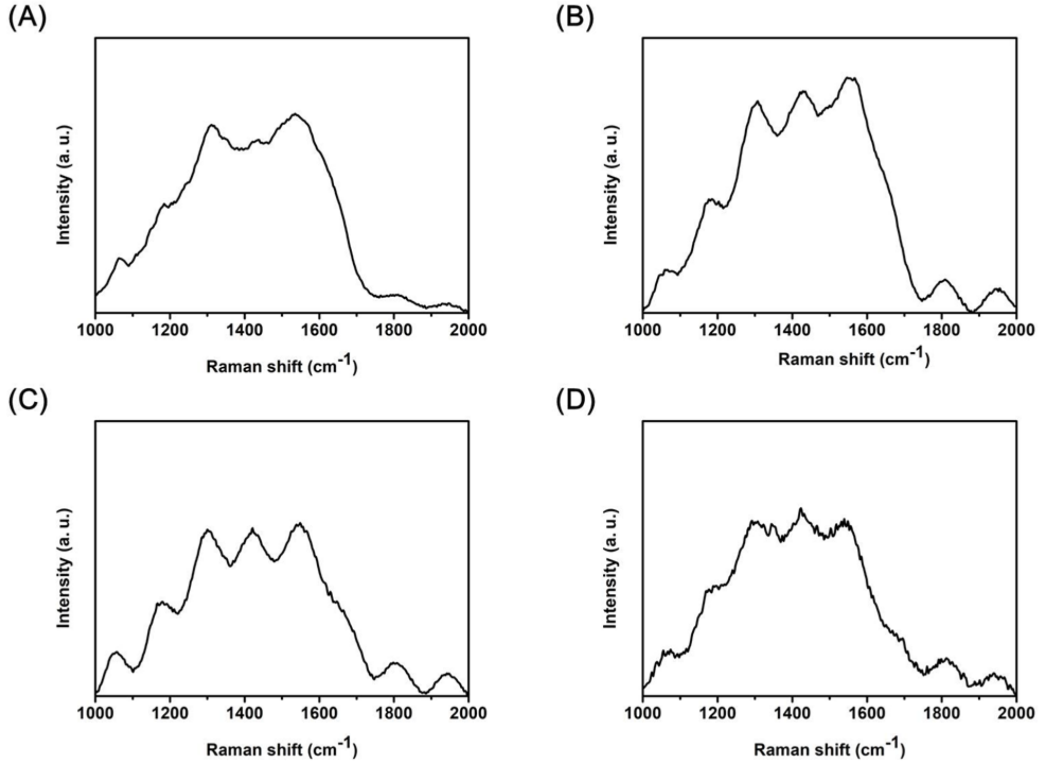

Figure 2-5. Raman spectra of (A) C dots, (B) Cl-C dots, (C) Br-C dots, and (D) I-C dots.

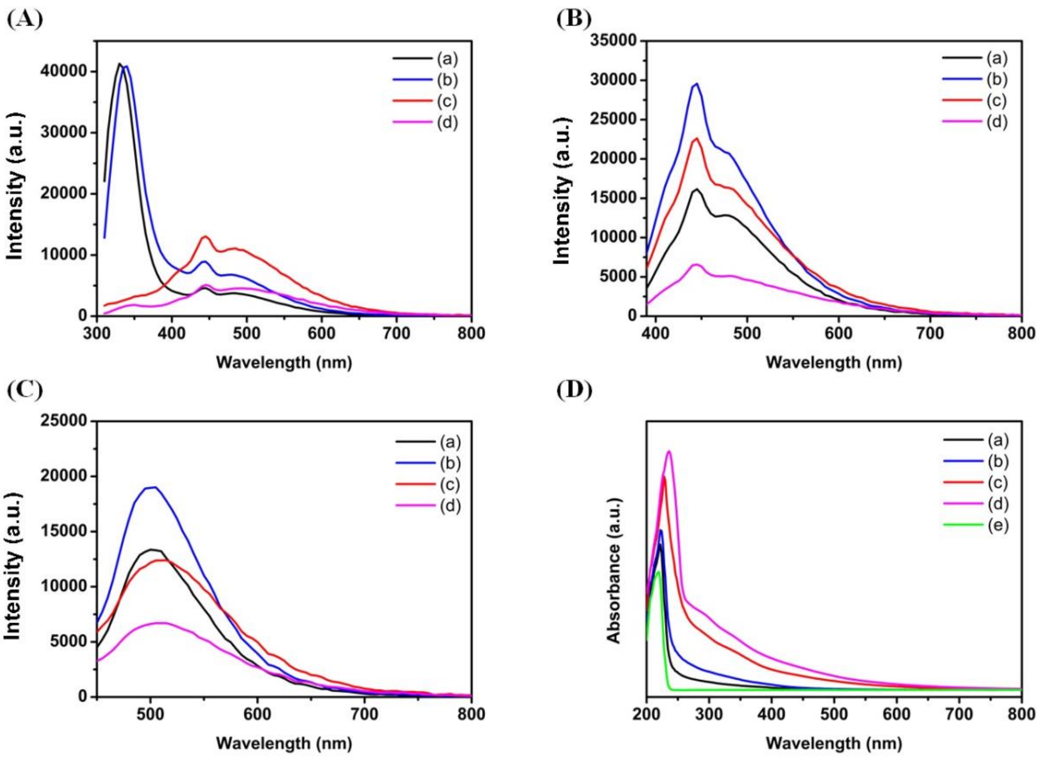

Figure 2-6. Effect of sodium halides on the formation of C dots from 0.63 M histidine solution at pH 9.0 with/without containing 1 M NaX at 10 V for 2 h. PL spectra (A-C) and UV-vis absorption spectra (D). PL spectra of C dots (a), Cl-C dots (b), Br-C dots (c), and I-C dots (d) at excitation wavelengths of (A) 280, (B) 360, and (C) 420 nm. UV-vis absorption spectra of C dots (a), Cl-C dots (b), Br-C dots (c), I-C dots (d) and histidine (e).

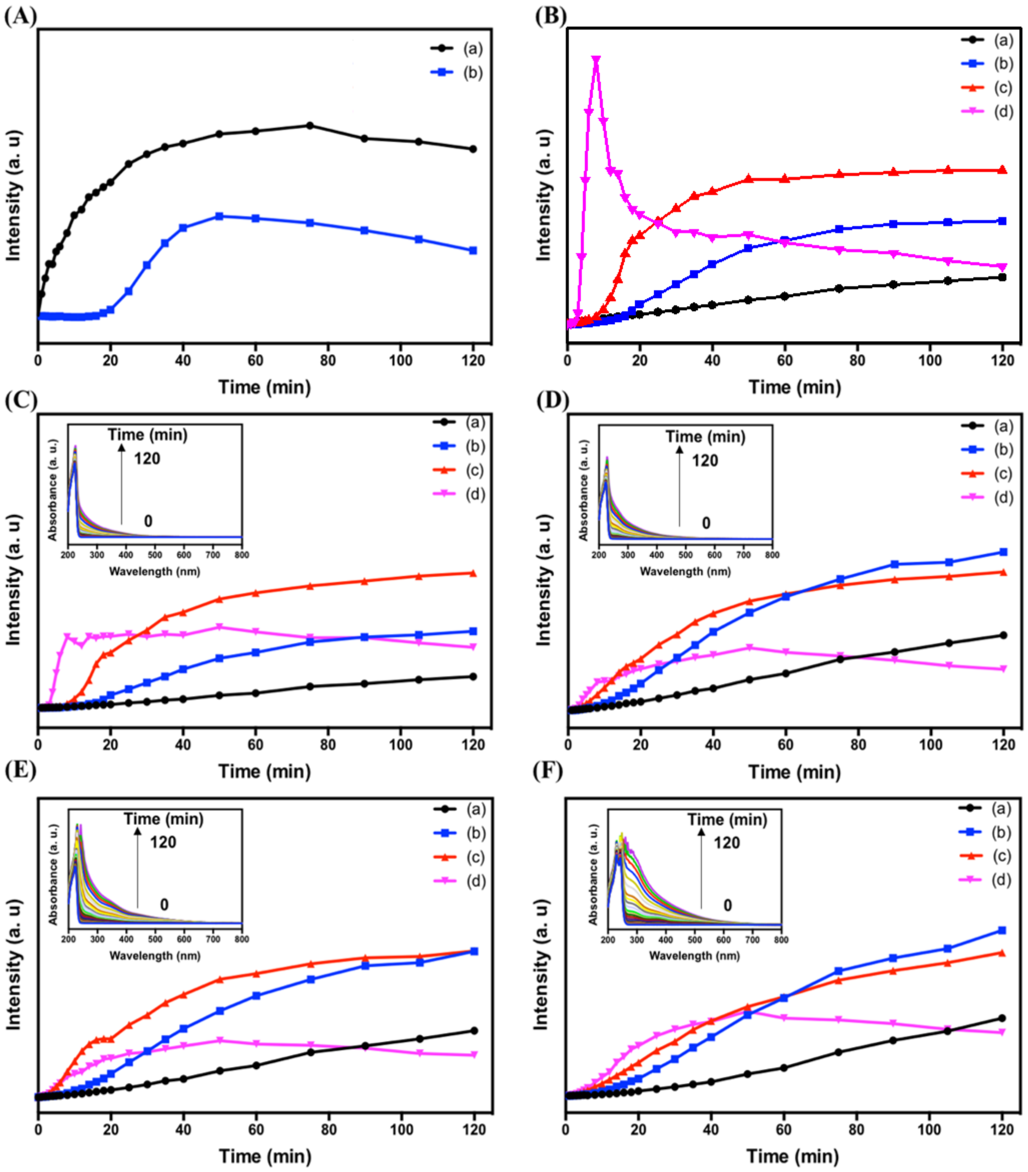

Figure 2-7. Effect of reaction time on the PL intensity and UV-vis absorption spectra of C dots (a), Cl-C dots (b), Br-C dots (c), and I-C dots (d). The emission wavelengths are 330 (A), 445 (B), and 505 nm (C), respectively, when excited at 280 nm. The emission wavelengths are 445 (D) and 490 nm (E), respectively, when excited at 360 nm. The emission wavelength is 505 nm (F) when excited at 420 nm. Insets in (C), (D), (E) and (F) are their corresponding UV-Vis absorption spectra. All C dots were prepared at 10

V from 0.63 M histidine solutions at pH 9.0 with/without containing 1 M NaX.

doi:10.6342/NTU202300566

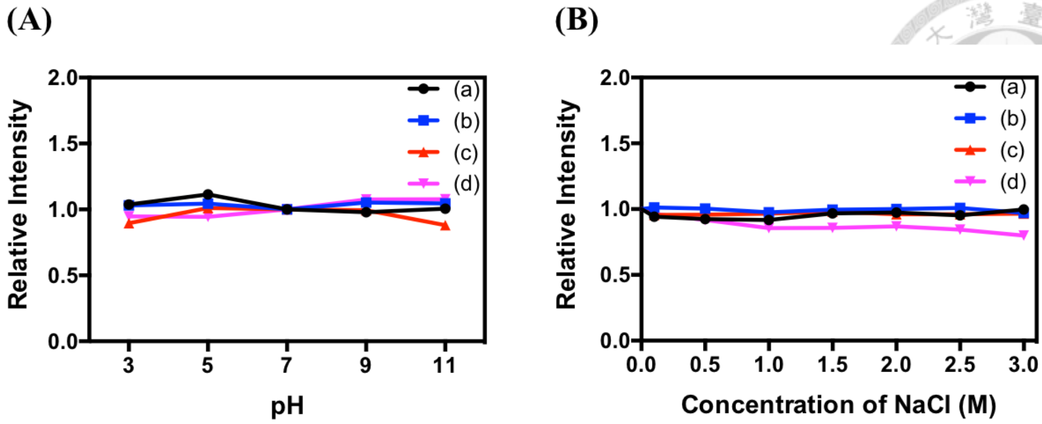

Figure 2-8. Effects of (A) pH (3.0–11.0) and (B) NaCl concentration (0–3.0 M) on the stability of (a) C dots, (b) Cl-C dots, (c) Br-C dots, and(d) I-C dots. C dots: 0.01X; phosphate solutions: 20 mM; excitation and emission wavelengths: 420 and 505 nm, respectively.

doi:10.6342/NTU202300566

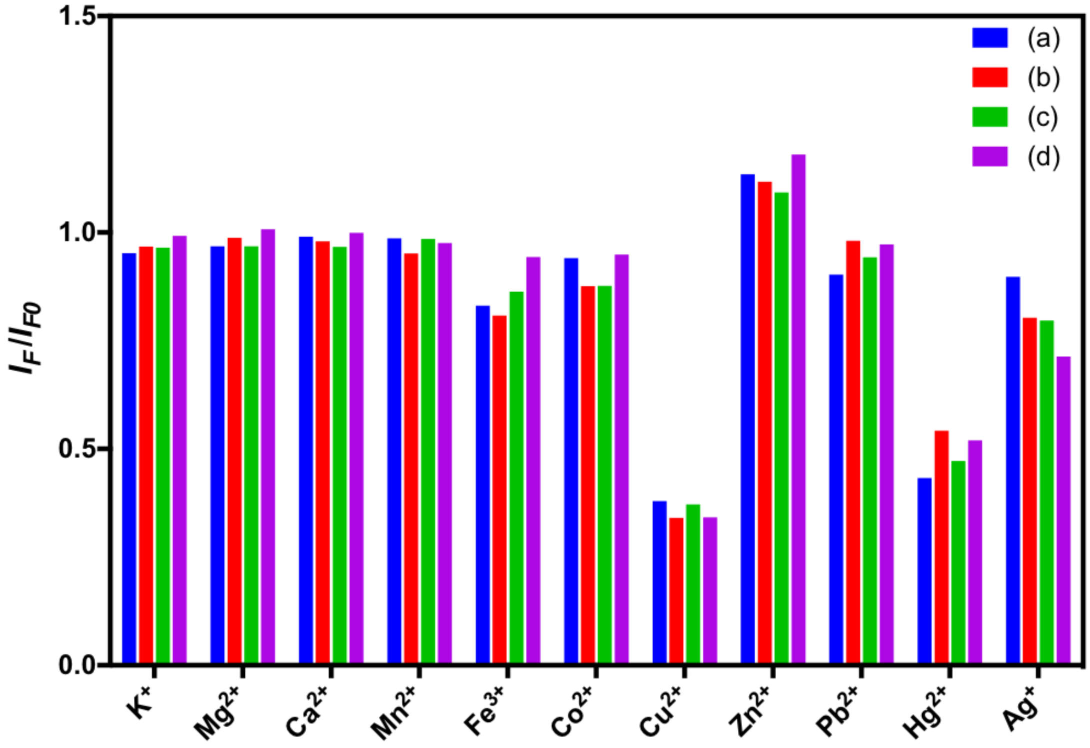

Figure 2-9. Selectivity of (a) C dots, (b) Cl-C dots, (c) Br-C dots, and (d) I-C dots toward the detection of Cu^{2+} ions (100 μM) over the other metal ions (100 μM) in phosphate buffer (20 mM, pH 3.0). The concentrations of the four C dots used are all 0.01X. Other conditions are the same as in Figure 2-6.

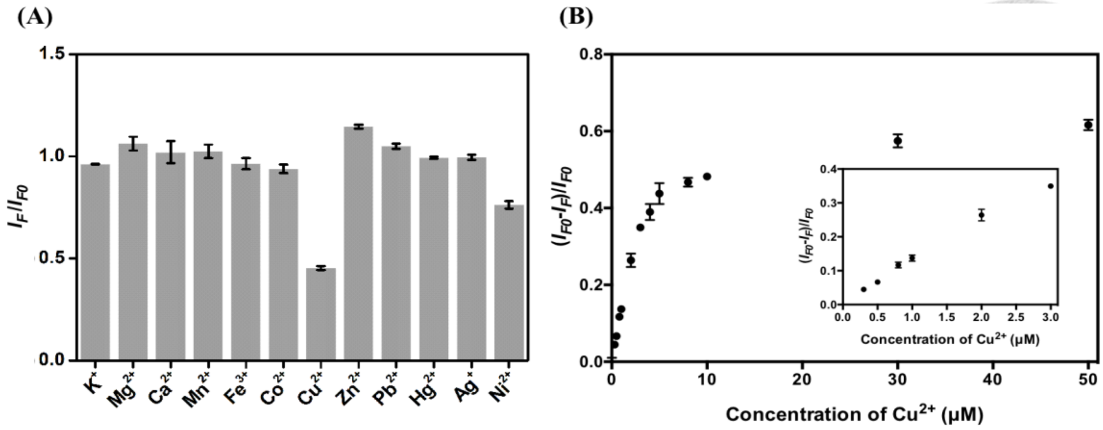

Figure 2-10. Selectivity (A) and sensitivity (B) of I-C dots for Cu^{2+} ions (100 μM) in phosphate buffer (20 mM, pH 3.0) containing 0.8 mM NaI and 1 mM citric acid. The concentrations of I-C dots in (A) and (B) are 0.01X and 0.001X, respectively. I_{F0} and I_F are the PL intensities of I-C dots at 505 nm in the absence and presence of Cu^{2+}, respectively, when excited at 420 nm. The concentrations for the other metal ions are all 100 μM. I-C dots were prepared from 0.63 M histidine solution at pH 9.0 containing 1 M NaI at 10 V for 2 h.

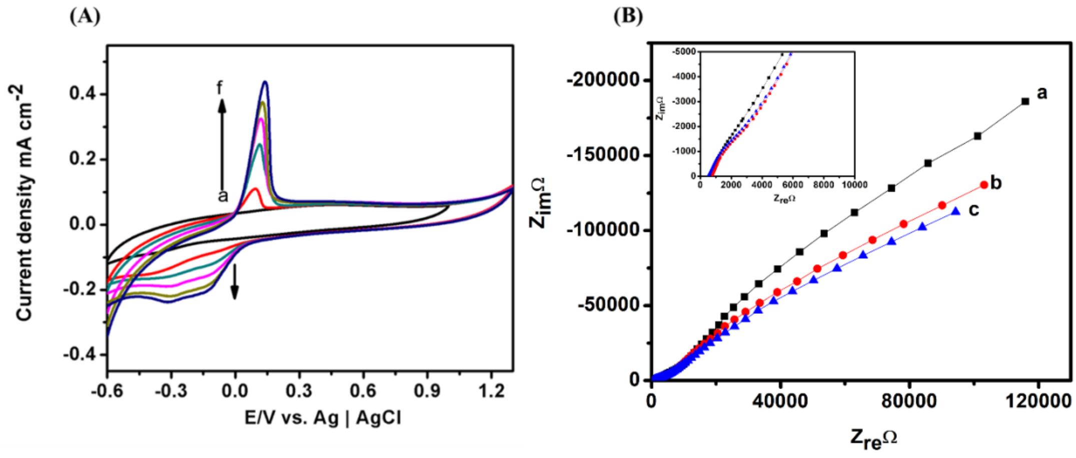

Figure 2-11. (A) CV curves and (B) EIS spectra of bare GCE recorded in phosphate buffer (20 mM, pH 3.0) under different conditions. (A) I-C dots were dispersed in phosphate buffer (20 mM, pH 3.0) solution (a) without and (b-f) with containing Cu^{2+} and Fe^{3+} (200 µM). Cu^{2+} ion concentrations (µM) used are (b) 100, (c) 200, (d) 300, (e) 400, and (f) 500. Fe^{3+} was added as a control. Scan rate for CV curves is 50 mV s^{-1}. (B) EIS spectra were recorded over the frequency range from 0.01 to 10000 Hz at an amplitude of 5 mV in N_2 saturated phosphate buffer (a) without I-C dots, (b) with I-C dots, and (c) with I-C dots and 100 µM Cu^{2+} ions. Inset in (B): Magnified view of high frequency region of EIS spectra.

doi:10.6342/NTU202300566

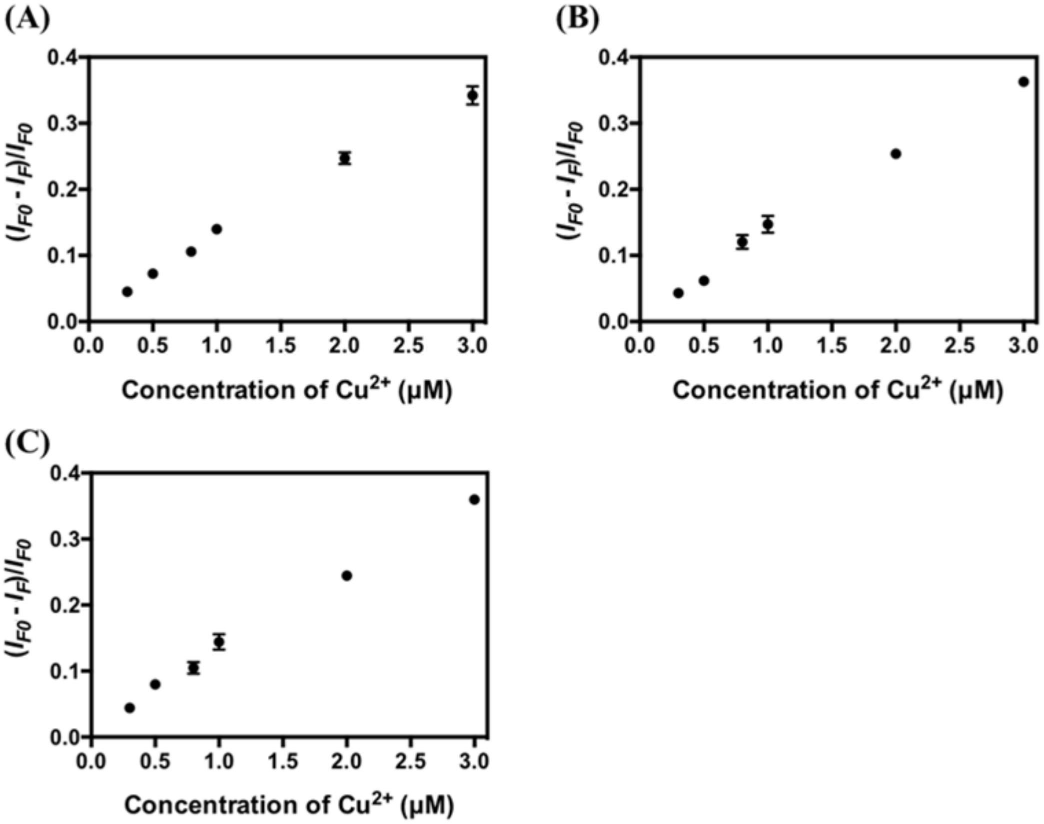

Figure 2-12. Linearity of relative PL intensity at 505 nm of I-C dots (0.001X) toward the quantitation of Cu^{2+} ions in (A) tap water, (B) lake water, and (C) seawater. Samples were mixed with phosphate buffer (20 mM, pH 3.0), and standard Cu^{2+} solutions. Other conditions are the same as in Figure 2-6.

doi:10.6342/NTU202300566

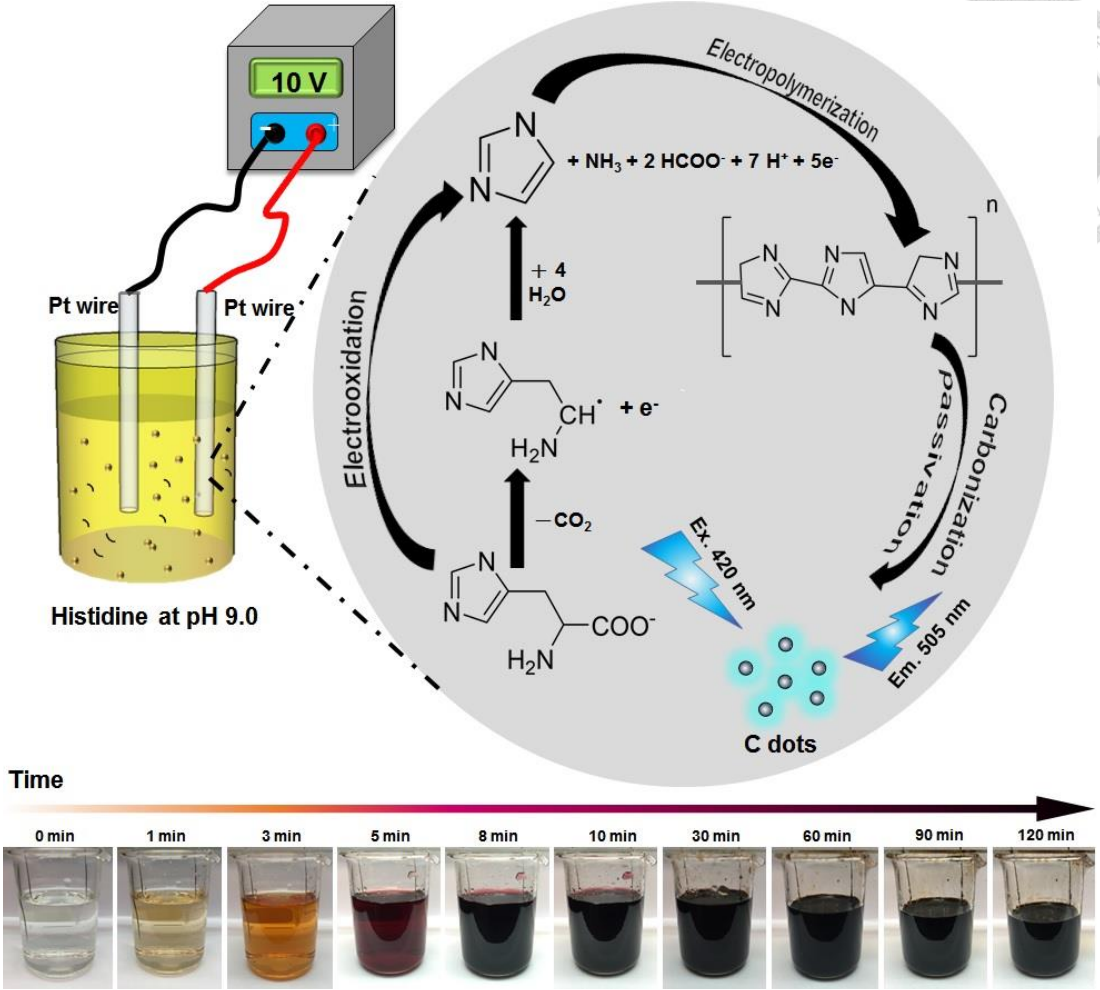

Scheme 2-1. Schematic representation of preparation of C dots from histidine hydrochloride through an electrochemical route.

Chapter 3 Carbon dots with polarity-tunable characteristics for the selective detection of sodium copper chlorophyllin and copper ions

The content in this chapter has been published to: Y.-S. Lin, Z.-Y. Yang, A Anand, C.-C. Huang, H.-T. Chang, Carbon dots with polarity-tunable characteristics for the selective detection of sodium copper chlorophyllin and copper ions. Anal. Chim. Acta 1191 (2022) 339311.

doi:10.6342/NTU202300566

3.1 Introduction

Carbon dots (CDs) are quasi-spherical nanoparticles of nanocarbon family with sizes below 10 nm [1]. Advantages of simple synthesis, low toxicity, high biocompatibility, and photo-stability of CDs allow for their application in different fields, including bioimaging [2,3], sensing [4–6], photocatalysis [7], and biomedical applications [8–11]. These applications also take advantage of their distinctive surface-structures, electronic and optical properties such as excitation-dependent emission and tunable bandgap, and diverse surface functional groups, which strongly depend on the synthesis methods, precursors, surface functionalization, passivation, and heteroatom doping [12]. Various approaches such as electrochemical oxidation [13], chemical oxidation [14,15], hydrothermal routes [16], and microwave-assisted heating [17], have been developed to obtain CDs. Of these methods, chemical oxidation has been proven to be highly favorable for the large-scale synthesis of CDs.

Copper is a widely used metal in numerous industrial, environmental, and domestic processes. However, environmental pollution as a result of rapid industrialization has led to a significant concern in environmental monitoring of Cu^{2+} ions [18]. Moreover, Cu^{2+} ion is one of the essential elements that plays an important role in many biological functions in humans [19], while excessive Cu^{2+} ion may cause diseases such as Wilson

doi:10.6342/NTU202300566

disease, and other neurodegenerative disorders like Alzheimer's and Parkinson's disease [20,21]. On the other hand, sodium copper chlorophyllin (SCC), a semi-synthetic derivative of chlorophyll (natural green pigment), is widely used as a food coloring agent for candies and olive oils to impart green color [22]. SCC is mainly produced by the saponification of chlorophyll by alkali treatment, to yield chlorophyllin, followed by the replacement of magnesium ion in the porphyrin ring with Cu^{2+} ion [22]. SCC is more stable than most green food coloring agents, and hence it is used as an adulterant to disguise inferior olive oil as high-quality virgin olive oil [23]. SCC is allowed as a food colorant in various products in the European Union (EU) [24,25]. The acceptable daily intake (ADI) of Cu-chlorophyll and related complexes is less than 15 mg kg^{-1} body weight/day [24] as recommended by EU, which is higher than that (7.5 mg kg^{-1} day^{-1}) allowed by the United States Food and Drug Administration (US FDA) [26]. Therefore, the detection of SCC in food samples is important due to its uptake regulation.

Inductively coupled plasma mass spectroscopy (ICP-MS) and liquid chromatography-mass spectrometry (LC-MS) are the common methods for the detection of Cu^{2+} ions and SCC, respectively [27,28]. However, the requirement of sophisticated equipments, complicated and time consuming operation procedures, and the cumbersome sample preparation tremendously limit their wide applications. Thus, it is necessary to

doi:10.6342/NTU202300566

develop detection methods for Cu^{2+} ions and SCC with advantages of high sensitivity, simple operation, rapid analysis, and low cost. In recent years, fluorescent CDs have been widely studied for the detection of metal ions [29–34]. CDs are biocompatible and exhibit excitation-dependent emission properties [35,36]. The fluorescence changes of CDs may depend on various mechanisms such as charge transfer (CT), photoinduced electron transfer (PET), excimer formation, Forster resonance energy transfer (FRET), or aggregation induced emission (AIE) [37]. Monitoring of fluorescence changes of CDs is usually conducted for the detection of Cu^{2+} ions [38–42]. However, they suffer from the interferences from metal ions such as Co^{2+}, Ni^{2+}, and Hg^{2+} [40–42], mainly because of their strong complexation with the surface functional groups (carboxylic and amine) of CDs [38–42]. Whereas, sulfonyl groups provide higher selectivity for Cu^{2+} ions over potential interfering metal ions like Co^{2+} [43]. Unlike Cu^{2+} ion, detection of copper- based complexes such as SCC is more challenging and CD-based fluorescence probes are rarely reported for the quantitation of SCC. Hydrophobic CDs from different precursors have been reported for various applications like fluorescence imaging probes, optoelectronic devices, photoluminescence ink, and polymer-based composite materials [44,45]. Therefore, preparing hydrophobic CDs can be a promising alternative for the detection and quantitation of SCC in drinks and food.

All the fluorescence-based probes reported for the detection of metal ions are either hydrophilic or hydrophobic [44,45]. To the best of our knowledge, no report is available on the synthesis of hydrophilic CDs from the hydrophobic ones, used for the detection of metal ions or metal-based complexes. In this study, CDs is prepared by chemical oxidation of triolein (TO) using concentrated sulfuric acid at ambient temperature (25 ˚C). TO is a relatively less expensive compound in the fatty acid family. Its olein group provides hydrophobicity when its glycerol part undergoes carbonization to form hydrophobic carbon dots (TO-C dots). The obtained TO-C dots are well dispersed in organic solution due to their long alkyl chains on the surfaces. One interesting characteristic of the TO-C dots is that their surface hydrophobicity can be easily converted to hydrophilicity after a simple hydrolysis reaction, followed by deprotonation of their carboxylic acid groups in NaOH solution. To show their potential for quantitation of Cu^{2+} ions in various samples, the hydrophobic TO-C dots were applied for the quantitation of SCC in non-alcoholic flavored drinks, meanwhile the hydrophilic TO-C dots were used for the analysis of Cu^{2+} in soil samples.

3.2 Experimental Section

3.2.1 Materials

Triolein was obtained from TCI (Tokyo, Japan). Aluminum chloride (> 99.0%), potassium nitrate (> 99.0%), quinine hemisulfate salt monohydrate (> 97.0%), rhodamine 6G (> 99.0%), silver nitrate (> 99.0%), sodium bicarbonate (> 95.0%), sodium chloride (> 99.0%), sodium copper chlorophyllin (> 98.0%), and sulfuric acid (> 98.0%) were bought from Sigma-Aldrich (St. Louis, USA). Cadmium chloride (99.0%), copper nitrate trihydrate (> 99.0%), and lead nitrate (> 99.0%) were obtained from Acros (Morris Plains, USA). Chromium nitrate (> 99.0%) and magnesium nitrate hexahydrate (> 98.0%) were purchased from SHOWA (Tokyo, Japan). Iron chloride (> 98.0%), nickel chloride (> 97.0%), cobalt chloride (> 9 7.0%), and mercury chloride (> 98.0%) were procured from Alfa Aesar (Heysham, England). Monobasic, dibasic, and tribasic sodium salts of phosphate (> 96.0%), sodium hydroxide (98.0%), and zinc nitrate hexahydrate (> 99.0%) were purchased from Macron Fine Chemicals (Center Valley, PA, USA). Calcium nitrate tetrahydrate (> 99.0%) and manganese chloride dihydrate (> 99.0%) were obtained from Merck (Kenilworth, NJ, USA). Montana soil (SRM2710) was obtained from National Institute of Standards and Technology (NIST, Maryland, USA). Non-alcoholic flavored drinks (green milk tea with SCC (Uni-President Enterprises Corporation, Tainan, Taiwan)

doi:10.6342/NTU202300566

and without SCC (Lipton, United Kingdom)) were purchased from a local market in Taipei City, Taiwan. Dimethyl sulfoxide (DMSO), ethanol, ethyl acetate, and toluene solvents (> 98.0%) were purchased from J.T. Baker (Center Valley, USA). Ultrapure water (18.2 MΩ cm) from a Milli-Q system (Millipore, USA) was used to prepare all solutions.

3.2.2 Preparation of hydrophobic and hydrophilic TO-C dots

TO-C dots were synthesized by a chemical oxidation approach [46]. 100 mM triolein (40 mL) was added into 13.5 M H_2SO_4 (40 mL) in a flask and stirred for 3 h at room temperature. Both triolein and H_2SO_4 were prepared in ethyl acetate. After the reaction, the mixture was diluted two times with ethyl acetate and purified by liquid-liquid extraction. Briefly, the mixture was extracted with ultrapure water (100 mL) once to remove the hydrophilic residues and excess sulfuric acid, and then neutralized the remaining H_2SO_4 in organic phase with 0.1 M $NaHCO_3$ (100 mL). After removing ethyl acetate by rotary evaporation, the $NaHCO_3$ and salt were removed by centrifugation to obtain hydrophobic TO-C dots. To prepare hydrophilic TO-C dots, 500 mg of hydrophobic TO-C dots were redispersed in 1 M NaOH solution (10 mL) and incubated for 30 min. The product obtained was dialysed against ultrapure water through a

doi:10.6342/NTU202300566

membrane (MWCO = 1.0 kDa) for 24 h, with the water replaced every 6 h. The solution was lyophilized and then redispersed in ultrapure water to obtain hydrophilic TO-C dots with a concentration of 50 mg mL^{-1} for further application.

3.2.3 Characterization of TO-C dots

Fluorescence measurements of TO-C dots were carried out using a FS5 spectrophotometer (Edinburgh instruments, Livingston, USA). A FluoTime 300 system (PicoQuant, Berlin, Germany) with a diode laser as the light source (emitting at 375 nm) was used to measure the fluorescence decay curves. UV-vis absorption spectra were recorded using Evolution 201/220 UV-visible spectrophotometer (Thermo, Waltham, MA, USA). A Varian 640 FTIR spectrophotometer (Palo Alto, CA, USA) was used to measure the Fourier transform infrared (FTIR) spectra of glycerol, triolein, and TO-C dots. The transmission electron microscopy (TEM) images of the TO-C dots were recorded using Hitachi H-7100 TEM (Tokyo, Japan). A K-Alpha X-ray photoelectron spectrometer (Thermo, Waltham, MA, USA) was used to perform the X-ray photoelectron spectroscopy (XPS) measurements. Calibration of the binding energy values of TO-C dots was done using the C1s signal at 284.6 eV as a standard.

doi:10.6342/NTU202300566

3.2.4 Determination of fluorescence quantum yield

The fluorescence quantum yield (QY) of TO-C dots was measured using quinine sulfate as the standard and calculated with the following equation:

$$\mathrm{QY} = \mathrm{QY}_{std} \times \frac{I_x}{I_{std}} \times \frac{A_{std}}{A_x} \times \left(\frac{\eta_x}{\eta_{std}}\right)^2$$

Where I_x and I_{std} denote the integrated fluorescence intensities of TO-C dots and quinine sulfate, respectively. A_x and A_{std} denote the absorbance values of TO-C dots and the standard, respectively. η_x and η_{std} represent the refractive indexs of the solvent used for dispersing TO-C dots and dissolving the standard, respectively. Quinine sulfate (QY_{std}: 54%) was dissolved in 0.1 M H_2SO_4 (refractive index: 1.33) and the hydrophobic TO-C dots were dispersed in ethyl acetate (refractive index: 1.37).

3.2.5 Detection of SCC

Detection of SCC (0–100 μM) using hydrophobic TO-C dots (1.0 mg mL^{-1}, final concentration) was conducted in ethyl acetate:acetone (5:1) solution. To obtain linearity for the quantitation of SCC, 100 μL of TO-C dots (10 mg mL^{-1}, in ethyl acetate/acetone solution) were added to 800 μL ethyl acetate/acetone solution followed by the addition of 100 μL SCC (0–1.0 mM, in ethyl acetate/acetone solution). After shaking at ambient temperature for 15 min, their fluorescence spectra were recorded under excitation at 400 nm. The assay validation was performed by the analyses of green milk tea with containing SCC (Uni-President Enterprises Corporation, Tainan, Taiwan) and without containing SCC (Lipton, United Kingdom) purchased from a local market in Taipei City, Taiwan. Liquid-liquid extraction of drinks (5.0 g) was performed according to a reported method (TFDAA0017.01) from Taiwan Food and Drug Administration (TFDA) [47]. Aliquots (200 μL) of the drinks were spiked with various concentrations of SCC (20 μL with final concentration of 1.0–10 μM). Subsequently, hydrophobic TO-C dots (10 mg mL^{-1}, 100 μL) and ethyl acetate/acetone solution (680 μL) were added to the spiked solutions (final volume 1.0 mL). The mixtures were equilibrated for 15 min, and their fluorescence spectra at an excitation wavelength of 400 nm were recorded. The spiked samples were further analyzed using ICP-MS. Aliquots (5 μL) of the drinks were treated with liquid-liquid extraction before being subjected to digestion with aqua regia. Before ICP-MS analysis, they were spiked with various concentrations (1.0–10 μM) of Cu^{2+} ions in 2% nitric acid.

3.2.6 Detection of Cu^{2+} ions

100 μL of hydrophilic TO-C dots (1.0 mg mL^{-1}) and 100 μL Cu^{2+} ions (0–1.0 mM) were added to 800 μL sodium phosphate buffer solution (12.5 mM, pH 8.0), and shaken

at ambient temperature for 15 min to attain equilibrium and the fluorescence spectra (excitation wavelength=400 nm) were recorded. The above procedure was repeated with other metal ions (Al^{3+}, Cd^{2+}, Ca^{2+}, Cr^{3+}, Cu^{2+}, Co^{2+}, Fe^{3+}, Pb^{2+}, Mg^{2+}, Mn^{2+}, Ni^{2+}, K^+, Ag^+, Zn^{2+} or Hg^{2+}; 100 μM, 100 μL) to invesitigate the selectivity of the assay. To test the tolerance (the tolerable concentration ratios for interferences with a relative error of <5%), 100 μL hydrophilic TO-C dots (1 mg mL^{-1}) and 100 μL Cu^{2+} ions (100 μM) were added to 800 μL sodium phosphate buffer solution (12.5 mM) followed by the addition of metal ions (Al^{3+}, Ca^{2+}, Cr^{3+}, Co^{2+}, Fe^{3+}, Pb^{2+}, Mg^{2+}, Ni^{2+}, K^+, or Zn^{2+}) with different concentrations and then shaken for 15 min before recording the fluorescence spectra. Applicality of the hydrophilic TO-C dots probe was validated by the analysis of a soil sample obtained from NIST. Acidic digestion of the soil sample (1.0 g) was performed according to EPA method 305B [48]. Briefly, aliquots (33 μL) of the diluted solution of digested soil samples were spiked with various concentrations (final concentrations 0.5–10 μM) of Cu^{2+} ions. Sodium phosphate buffer (50 μL, 200 mM, pH 8.0), 100 μL hydrophilic TO-C dots (1.0 mg mL^{-1}, 100 μL), and ultrapure water were added (final volume 1.0 mL) to the spiked solutions and the mixtures were shaken at ambient temperature for 15 min to attain equilibrium before recording their fluorescence spectra.

doi:10.6342/NTU202300566

3.3 Results and Discussion

3.3.1 Synthesis of TO-C dots

The hydrophobic TO-C dots with their surfaces dominated by alkyl groups along with some carboxyl, hydroxyl, and sulfonyl groups were prepared at ambient temperature by a concentrated sulfuric acid-mediated oxidation reaction of triolein (Scheme 3-1). Concentrated sulfuric acid was chosen as the carbonization agent due to (1) its strong dehydrating activity for carbonization, (2) its strong oxidizing ability that assists the generation of hydroxyl and carboxyl groups, and (3) its ability to generate sulfur-containing functional groups on CDs such as sulfonyl groups through an addition reaction [49]. The advantage of this synthesis method is that it could achieve carbonization and surface functionalization without the need for applying high temperature or any additional energy. Triolein is a symmetrical triglyceride derived from glycerol with three branches of mono-unsaturated omega-9 fatty acid (i.e., oleic acid; an organic acid with a long chain of 17 carbon atoms), and thus it is insoluble in water. The polyol characteristic (three hydroxyl groups) of glycerol imparts increased miscibility with water and hygroscopic nature. At high temperature (160 °C), glycerol in the presence of sulfuric acid could be carbonized to form nanocarbon [50], however it produces mostly soluble sulfonated products at lower temperature (100 °C) [50]. In the present study, no CDs were formed

doi:10.6342/NTU202300566

when glycerol (50 mM) was used as the precursor to react with sulfuric acid (6.75 M) at ambient temperature (data not shown). Figure 3-1 shows the UV-vis absorption and fluorescence spectra of the products obtained separately from glycerol and triolein after their reactions with sulfuric acid. In the case of glycerol, the resulting solution was colorless, and no absorption and fluorescence peaks were observed (Figure 3-1A). In contrast, for triolein (50 mM), a dark brown solution was obtained after the reaction, and an absorption band at 265 nm and a shoulder band at around 320 nm were obsedrved, attributed to the $\pi \rightarrow \pi^*$ and $n \rightarrow \pi^*$ transition of C=C and C=O bonds due to carbonization and oxidation, respectively (Figure 3-1B(a)). The as-formed TO-C dots (Figure 3-2) show excitation wavelength-dependent fluorescence emission properties (Figure 3-1B(b)), mainly due to the polycyclic aromatic domains formed with different sizes, surface and/or crystal defects, and existence of various surface functional groups [35]. The average particle diameter of TO-C dots is 6.0 ± 1.3 nm ($n = 50$) as measured by the TEM (Figure 3-2A). The FT-IR spectra of glycerol and triolein before and after reacting with concentrated sulfuric acid are shown in Figure 3-3(a–d). Glycerol after reacting with concentrated sulfuric acid shows four new peaks at 2910, 2820, 1650, and 1350 cm^{-1}, which are assigned to Fermi resonance of aldehydic C–H stretching, overtone of the C–H bending peak, C=C stretching, and S=O stretching vibrations, respectively [51]. The

doi:10.6342/NTU202300566

formation of these functional groups is mainly through partial carbonization, oxidation, and sulfonation of glycerol. In the case of hydrophobic TO-C dots, the peaks at around 3500, 2910/2820, 1750, 1350, and 1260 cm^{-1} correspond to O–H, alkane/C−H, C=O, S=O, and C−O stretching vibrations, respectively. When compared to curve (b), the prominent peaks of C=O, S=O, and C−O in the hydrophobic TO-C dots (curve d) reveal stronger oxidization and sulfonation. Moreover, the peak at 1699 cm^{-1} due to the aromatic C=C bond indicates carbonization occurred during the formation of the TO-C dots [52]. Deconvoluted XPS spectra (Figure 4-4) reveal the presence of C–C/C=C (284.8 eV, 78.4%), C–S (285.8 eV, 7.8%), C–O (286.6 eV, 10.6%) and C=O (288.8 eV, 3.1%) (C1s); O–S (531.6 eV, 16.8%), O=C (532.1 eV, 48.3%) and O–C (533.4 eV, 34.9%) (O1s), and –C–SO$_3$ 2p$^{3/2}$ (168.6 eV (2p$_{3/2}$), 64.2%) and 2p$^{1/2}$ (170.1 eV (2p$_{1/2}$), 35.8%) (S2p), which further evidence the oxidization, sulfonation and carbonization processes during the formation of the TO-C dots.

Scheme 3-1 presents the proposed formation mechanism of the TO-C dots from triolein at ambient temperature. During the reaction with sulfuric acid, triolein undergoes acylization to form acyl cations [53]. The acyl cations, as the electrophilic group, further go through electrophilic addition with alkenyl groups on triolein to form ketones containing carbocations. The carbocation-containing ketones follow two reactions: (1)

formation of carbocation-containing ketones with more alkyl groups (i.e., polymeric carbocation-containing ketones) through stepwise electrophilic addition with alkenyl groups, and (2) formation of alkenes by acid-catalyzed aldol condensation with other carbocation-containing ketones [54]. Besides, the formation of alkyl hydrogensulphates with sulfonyl groups is as a result of the sulfuric acid-mediated sulfonation of alkenes. Subsequently, TO-C dots are formed by a process of polymerization through repeated electrophilic addition and condensation followed by carbonization and surface passivation.

3.3.2 Effect of triolein and sulfuric acid concentration

We studied the effect of triolein concentration with a fixed sulfuric acid concentration and *vice versa*, on the formation of TO-C dots. Figure 3-5(A–C) displays the absorption spectra of products from the reactions of different concentrations of triolein (5–200 mM) and 6.75 M sulfuric acid for 3 h. The absorbance at 260 nm increased with increase in the concentration of triolein, while the fluorescence intensity at 370 nm only increased upon increasing the concentration of triolein up to 50 mM. Upon further increasing its concentration to 200 mM, the fluorescence intensity decreased significantly. The TEM images (Figure 3-6A) reveal that the average particle sizes (n = 100) of

doi:10.6342/NTU202300566

hydrophobic TO-C dots consistently increased from 6.0 ± 1.5 nm to 115.1 ± 42.6 nm with the increase in the concentration of triolein from 5 to 200 mM, which may be due to the increase in the degree of polymerization and carbonization. The larger particle size and core-shell structure are due to the incomplete carbonization, leading to a polymer-like shell capped on the carbonized core. The highest QY was observed (23.2%) when the concentration of triolein was 50 mM. Figure 3-5b shows the effect of concentration of sulfuric acid (0.09–9.00 M) used in the preparation of hydrophobic TO-C dots using 50 mM triolein as the precursor. The absorbance at 260 nm increased upon increasing the concentration of sulfuric acid. The fluorescence intensity at 370 nm increased with increase in the sulfuric acid concentration up to 6.75 M. Further increasing sulfuric acid concentration, significant carbonation led to formation of large particles with weak fluorescence. Thus, the optimal sulfuric acid concentration for the synthesis of carbon dots was set as 6.75 M on the basis of fluorescence intensity. The TEM images (Figure 3-6B) also reveal the significant change in the size and morphology of TO-C dots with the increase in sulfuric acid concentration. The TO-C dots with a core-shell structure is formed only at the concentration of sulfuric acid < 4.50 M, and the size of TO-C dots decreased from 161.7 ± 47.6 nm to 7.48 ± 2.86 nm upon increasing sulfuric acid concentration from 4.50 to 6.75 M.

3.3.3 Concentration-dependent optical properties of TO-C dots

The hydrophobic TO-C dots prepared in ethyl acetate exhibit concentration-dependent fluorescence behavior (Figure 3-7); as their concentration increased from 0.66 to 33 mg mL^{-1}, the maximum excitation/emission wavelengths shifted from 320/370 to 440/540. This concentration-dependent fluorescence of hydrophobic TO-C dots was also prominent in other polar organic solvents such as ethanol, dimethyl sulfoxide, and toluene (Figure 3-8). The concentration-dependent shift in the maximum excitation/emission wavelengths, irrespective of the organic solvents, implies the aggregation of CDs at higher concentration. The aggregation of TO-C dots at a high concentration is supported by the TEM images (Figure 3-2A and 3-2B). At a lower concentration (0.66 mg mL^{-1}), the average diameter of TO-C dots was ca. 2.8 nm, while at a higher concentration (33 mg mL^{-1}), the aggregated size increased to ca. 110 nm. The fluorescence emission process of CDs is dominated not only by core crystal structure but also surface states [54]. In the TO-C dots, the surface states are regulated by the graphene-core edge as well as surface ligands such as alkylene, sulfonyl, and carbonyl groups. The aggregation of TO-C dots can extent the π-electron conjugation system. Therefore, an increase in the aggregation of TO-C dots could significantly lower the electronic bandgap, causing a red-shift in the

doi:10.6342/NTU202300566

maximum excitation/emission wavelengths [55].

3.3.4 Fluorescence detection of sodium copper chlorophyllin (SCC) by hydrophobic TO-C dots

First we tested hydrophobic TO-C dots for the detection of sodium copper chlorophyllin (SCC). SCC could quench the fluorescence of TO-C dots significantly (Figure 3-9A). To minimize the interference from sample matrix, the detection was conducted at the excitation/emission wavelengths of 400/500 nm. Figure 3-9B shows that the relative fluorescence decrease $[(I_{F0}–I_F)/I_{F0}]$ of TO-C dots in ethyl acetate:acetone (5:1) solution increases upon increasing the concentration of SCC in the range of 1.0–100 μM. The TO-C dots probe exhibits linear response toward SCC over the concentration range of 1.0–10 μM ($R^2 = 0.97$), with a LOD (signal-to-noise ratio of 3) of 0.61 μM (38.7 ppb for copper) at a signal-to-noise ratio of 3. The LOD is much lower than the maximum allowable level (64 ppm for copper) of SCC in non-alcoholic flavored drinks defined by TFDA [56]. Since SCC does not possess absorption bands over the range of 400 to 600 nm in ethyl acetate:acetone solvent (Figure 3-10), we can exclude the possibility of inner filter effect and FRET for the fluorescence quenching. A recent report by Ji *et al.* reveals that copper chlorophyllin interacts with CDs and significantly declines their fluorescence *via* electron transfer and FRET [57]. The different observation could be due to different types of CDs used. Figure 3-11 displays the fluorescence decay of TO-C dots in the absence and presence of SCC measured by time-correlated single-photon counting, with excitation and emission wavelengths of 375 and 460 nm, respectively. The average fluorescence lifetimes of the hydrophobic TO-C dots in the absence and presence of SCC are 3.701 and 3.167 ns, respectively, suggesting that photoinduced electron transfer (PET) mainly contributes to the SCC-induced fluorescence quenching of TO-C dots [58]. The copper ion is chelated by chlorophyllin as an electron acceptor for PET, and chlorophyllin moiety facilitates its access to the surfaces of TO-C dots. Furthermore, the hydrophobic TO-C dots were highly specific in the determination of Cu-based complexes. No fluorescence quenching of TO-C dots was observed in the presence of chlorophyll (chlorophyllin magnesium complex) (Figure 3-9A), which suggests that the fluorescence quenching of TO-C dots is highly related to their interaction with metal ions in the complex, rather than the organic part of the molecule.

We further employed hydrophobic TO-C dots to determine the concentration of SCC in non-alcoholic flavored drinks by applying a standard addition method. Table 3-1 shows percent recovery (%R) values of 98–103% and RSDs of <1.2% for the pretreated samples after spiked with SCC over the concentration range from 1.0 to 10 μM. The concentrations

doi:10.6342/NTU202300566

of SCC determined by the hydrophobic TO-C dots and ICP-MS were found to be 5.90 (±0.22) and 5.80 (±0.15) μM (n = 3), respectively. The t-test value and F-test value obtained by correlating the two methods were 1.40 (critical t-test value of 2.78 at a 95% confidence level) and 3.77 (critical F-test value of 19 at a 95% confidence level), respectively, revealing insignificant difference in the two results.

Hydrophobic TO-C dots are highly soluble in organic solvent, which is suitable for the analysis of hydrophobic analyte SCC, which can eliminate the interference from water-soluble interferents such as copper ions or other metal ions. As can be seen in Figure 3-12, Cu^{2+} ions did not quench the fluorescence of hydrophobic TO-C dots in ethyl acetate:acetone solvent, revealing their high selectivity toward SCC. In addition, SCC did not exhibit the UV-visible absorption in the 400–600 nm range (Figure 3-10), which excluded the inner filter effect. Copper chlorophyllin is widely used as a coloring agent in oils such as olive oil. The hydrophobic TO-C dots are very suitable for the detection of copper chlorophyllin in oil samples due to their hydrophobic characteristic, which are otherwise difficult with hydrophilic CDs. Whereas the hydrophilic TO-C dots selectively interact with Cu^{2+} ions *via* sulfonyl groups, leading to the formation of complex and fluorescence quenching, while other metal ions did not form complex or quenching. Therefore, we believe the synthesis strategy and analysis method design are quite different from other reported methods.

3.3.5 Preparation of hydrophilic CDs and detection of Cu^{2+} ions

The hydrophilic TO-C dots were obtained by NaOH-mediated hydrolysis of the hydrophobic TO-C dots. The dispersibility of hydrophilic TO-C dots in water (solubility > 20 mg mL^{-1}) is greatly enhanced as a result of the formation of carboxylate groups through hydrolysis of ester groups (curve e in Figure 3-3). Hydrophilic TO-C dots' excitation and emission characteristics are similar to that of hydrophobic TO-C dots; however, the fluorescence intensity of hydrophilic TO-C dots is about 10-fold lower than that of hydrophobic TO-C dots, due to solvent effect in the aqueous medium (Figure 3-13). After the conversion of hydrophobic TO-C dots into hydrophilic TO-C dots, the interaction of the surface functional groups with the polar solvent has a significant effect on their surface-related fluorescence properties [59]. Their average size (18.5 ± 5.0 nm) is larger than that (6.0 ±1.3 nm) of the hydrophobic TO-C dots, since the TO-C dots are aggregated through surface interaction while transferred into water phase. The contact angle of hydrophilic TO-C dots (12°) on a glass slide is much smaller than that of the hydrophobic TO-C dots (79°), which confirms the conversion of the hydrophobic TO-C dots to hydrophilic TO-C dots after NaOH treatment. To show the potential application of the hydrophilic TO-C dots, they were employed in the detection of various metal ions. Our results show that the TO-C dots is highly selective toward Cu^{2+} ions, as evident from its significant fluorescence quenching over that induced by the other tested ions (Figure 3-14A). The multidentate complexation of surface ligands of TO-C dots, such as carboxylate, hydroxyl, and sulfonyl with the Cu^{2+} ions lead to aggregation and thus PET, i.e., the excited electrons from the TO-C dots translate to the free *d*-orbital of Cu^{2+} ions, and thereby inducing fluorescence quenching. The fluorescence quenching induced by Cu^{2+} increases upon increasing the pH value up to 8.0, revealing that the deprotonated carboxylate and sulfonate groups play a vital role in the coordination to Cu^{2+} (Figure 3-15). Compared to other CDs for detecting Cu^{2+} ions [60–62], the use of hydrophilic TO-C dots shows minimum interference from other metal ions such as Co^{2+} and Ni^{2+} ions, mainly attributed to their sulfonyl groups present on the surfaces [43]. Figure 3-16 shows the decrease in the peaks at 1560 cm^{-1} (C=O stretching) and 1380 cm^{-1} (S=O stretching) upon the addition of Cu^{2+} ions into the TO-C dots, which strongly supports sulfonyl groups participate in their coordination with Cu^{2+} ions. Also, after incubating with Cu^{2+} ions, the TO-C dots shows aggregation as evident from the TEM images (Figure 3-2D). The increase in the size of TO-C dots (from 18.5 ± 5.0 nm; $n = 100$ to 30.4 ± 11.3 nm; $n = 50$) in the presence of Cu^{2+} further confirms that Cu^{2+} caused the aggregation of the

doi:10.6342/NTU202300566

TO-C dots, due to the electrostatic interaction between the Cu^{2+} ions and the highly cationic (zeta potential = –69.3 mV) hydrophilic TO-C dots [63]. The shorter average fluorescence lifetime of hydrophilic TO-C dots after reacting with Cu^{2+} (4.462 ns *vs.* 2.486 ns) demonstrates PET also contributes to the fluorescence quenching (Figure 3-17).

Figure 3-14B shows that the relative fluorescence change of hydrophilic TO-C dots increases with Cu^{2+} ion concentration in the range of 0.5–100 μM. The TO-C dots exhibits linear response toward Cu^{2+} ions over the concentration range of 0.5–10 μM ($R^2 = 0.99$), with a LOD of 0.21 μM (13.3 ppb), which is lower than the permitted maximum level of copper in drinking water (20 μM, 1.27 ppm) set by US Environmental Protection Agency (EPA) [64]. A comparison of various CDs-based probes for Cu^{2+} ion detection (Table 3-2) shows the superior nature of hydrophilic TO-C dots probe with a lower LOD [65−70]. The highly selective TO-C dots probe is a potential candidate for the detection of Cu^{2+} ions in real samples with complex matrixes.

The practicality of hydrophilic TO-C dots probe was confirmed by the quantitatation of Cu in the soil sample (Montana Soil, SRM2710). We first evaluated the tolerance of the TO-C dots probe to higher metal content (interfering ions) in the soil sample. When sensing Cu^{2+} ions using the TO-C dots probe, the tolerance concentrations of common interfering ions in the soil sample were at least 10 times the Cu^{2+} concentrations (within a relative error of ± 5%) (Table 3-3). By applying an standard addition method, the concentration of Cu^{2+} ions in the Montana Soil sample (certified value 2.95 mg g^{-1}) determined by our TO-C dots probe was 2.89 ± 0.06 mg g^{-1} (n = 5), showing a nonsignificant difference at 95% confidence level (Table 3-4). Therefore, with high sensitivity, selectivity, and great tolerance, the hydrophilic TO-C dots probe is suitable for quantifying Cu^{2+} ions in soil samples.

3.4 Conclusions

A one-step chemical oxidation approach was applied for synthesizing hydrophobic carbon dots (TO-C dots) at ambient temperature by a strong oxidation reaction of triolein with concentrated sulfuric acid. The hydrophobic TO-C dots exhibit concentration- and excitation-dependent emission characteristics. Deprotonation of carboxylic acid groups on the surface of hydrophobic TO-C dots through a simple hydrolysis reaction in NaOH solution yielded hydrophilic TO-C dots. The presence of sulfonyl groups on their surface enhances their selectivity toward Cu^{2+} ions. Chlorophyllin moiety on the surface of hydrophobic TO-C dots facilitates the access and interaction of SCC, and induced fluorescence quenching through PET. On the other hand, upon coordination with the surface groups of the hydrophilic TO-C dots, Cu^{2+} ions induced their aggregation and thus caused fluorescence quenching. The hydrophobic and hydrophilic TO-C dots probes

doi:10.6342/NTU202300566

were validated by the quantitation of SCC in non-alcoholic flavored drinks and Cu^{2+} ions in a soil sample, respectively. Our results show great potential of the highly sensitive and selective probes for rapid screening of Cu^{2+} ions and copper-based complexes in environmental samples and foods.

3.5 References

[1] J. Liu, R. Li, B. Yang, Carbon Dots: A new type of carbon-based nanomaterial with wide applications. ACS Cent. Sci. 6 (2020) 2179–2195.

[2] H. Li, X. Yan, D. Kong, R. Jin, C. Sun, D. Du, Y. Lin, G. Lu, Recent advances in carbon dots for bioimaging applications. Nanoscale Horiz. 5 (2020) 218–234.

[3] Y. Song, S. Zhu, B. Ying, Bioimaging based on fluorescent carbon dots. RSC Adv. 4 (2014) 27184–27200.

[4] H.-W. Chu, B. Unnikrishnan, A. Anand, Y.-W. Lin C.-C. Huang, Carbon quantum dots for the detection of antibiotics and pesticides. J. Food Drug Anal. 28 (2020) 539–557.

[5] X. Sun, Y. Lei, Fluorescent carbon dots and their sensing applications. Trends Anal. Chem. 89 (2017) 163–180.

[6] D. Xu, Q. Lin, H.-T. Chang, Recent advances and sensing applications of carbon dots. Small Methods 4 (2020) 1900387.

[7] R. Wang, K.-Q. Lu, Z.-R. Tang, Y.-J. Xu, Recent progress in carbon quantum dots: synthesis, properties and applications in photocatalysis. J. Mater. Chem. A 5 (2017) 3717–3734

doi:10.6342/NTU202300566

[8] A. Alaghmandfard, O. Sedighi, N.T. Rezaei, A.A. Abedini, A.M. Khachatourian, M.S. Toprak, A. Seifalian, Recent advances in the modification of carbon-based quantum dots for biomedical applications. Mater. Sci. Eng. C 120 (2021) 111756.

[9] H. Ding, X.-X. Zhou, J.-S. Wei, X.-B. Li, B.-T. Qin, X.-B. Chen, H.-M. Xiong, Carbon dots with red/near-infrared emissions and their intrinsic merits for biomedical applications. Carbon 167 (2020) 322–344.

[10] F. Huo, P. G. Karmaker, Y. Liu, B. Zhao, X. Yang, Preparation and biomedical applications of multicolor carbon dots: recent advances and future challenges. Part. Part. Syst. Charact. 37 (2020) 1900489.

[11] S. Ross, R.-S. Wu, S.-C. Wei, G.M. Ross, H.-T. Chang, The analytical and biomedical applications of carbon dots and their future theranostic potential: A review. J. Food Drug Anal. 28 (2020) 677–695.

[12] M.L. Liu, B.B. Chen, C.M. Li, C.Z. Huang, Carbon dots: synthesis, formation mechanism, fluorescence origin and sensing applications. Green Chem. 21 (2019) 449–471.

[13] M. Liu, Y. Xu, F. Niu, J.J. Gooding, J. Liu, Carbon quantum dots directly generated from electrochemical oxidation of graphite electrodes in alkaline alcohols and the

applications for specific ferric ion detection and cell imaging. Analyst 141 (2016) 2657–2664.

[14] J. Peng, W. Gao, B.K. Gupta, Z. Liu, R. Romero-Aburto, L. Ge, L. Song, L.B. Alemary, X. Zhan, G. Gao, S.A. Vithayathil, B.A. Kaipparettu, A.A. Marti, T. Hayashi, J.-J. Zhu, P.M. Ajayan, Graphene quantum dots derived from carbon fibers. Nano Letters. 12 (2012) 844–849.

[15] D. Sun, R. Ban, P.-H. Zhang, G.-H. Wu, J.-R. Zhang, J.-J. Zhu, Hair fiber as a precursor for synthesizing of sulfur- and nitrogen-co-doped carbon dots with tunable luminescence properties. Carbon. 64 (2013) 424–434.

[16] M. Vedamalai, A.P. Periasamy, C.-W. Wang, Y.-T. Tseng, L.-C. Ho, C.-C. Shih, H.-T. Chang, Carbon nanodots prepared from o-phenylenediamine for sensing of Cu^{2+} ions in cells. Nanoscale. 6 (2014) 13119–13125.

[17] R.K. Singh, R. Kumar, D.P. Singh, R. Savu, S.A. Moshkalev, Progress in microwave-assisted synthesis of quantum dots (graphene/carbon/semiconducting) for bioapplications: a review. Mater. Today Chem. 12 (2019) 282–314.

[18] D. Dong, L.V. Oers, A. Tukker, E.V.D. Voet, Assessing the future environmental impacts of copper production in China: Implications of the energy transition. J. Clean. Prod. 274 (2020) 122825.

doi:10.6342/NTU202300566

[19] E.I. Solomon, D.E. Heppner, E.M. Johnston, D.W. Cinsbach, J. Cirera, M. Qayyum, M.T. Kieber-Emmons, C.H. Kjaergaard, R.G. Hadt, L. Tian, Copper active sites in biology. Cham. Rev. 114 (2014) 3659–3853.

[20] E. Gaggelli, H. Kozlowski, D. Valensin, G. Valensin, Copper homeostasis and neurodegenerative disorders (Alzheimer's, prion, and Parkinson's diseases and amyotrophic lateral sclerosis). Cham. Rev. 106 (2006) 1995–2044.

[21] O. Bandmann, K.H. Weiss, S.G. Kaler, Wilson's disease and other neurological copper disorders. Lancet Neurol. 14 (2015) 103–113.

[22] A.M. Humphrey, Chlorophyll Food Chemistry. 5 (1980) 57–67.

[23] B. Gandul-Rojas, M. Roca, L. Gallardo-Guerrero, Detection of the color adulteration of green table olives with copper chlorophyllin complexes (E-141ii colorant). LWT-Food Sci. Technol. 46 (2012) 311–318

[24] EFSA ANS Panel (EFSA Panel on Food Additives and Nutrient Sources Added to Food). Scientific Opinion on re-evaluation of copper complexes of chlorophylls (E141(i)) and chlorophyllins (E141(ii)) as food additives. EFSA Journal. 13 (2015) 4151.

[25] JECFA. Purity specifications for chlorophyllins, copper complexes sodium and potassium salts.

http://www.fao.org/ag/agn/jecfaadditives/specs/monograph5/additive-127-m5.pdf (accessed 13 March 2017).

[26] FDA (United States Food and Drug Administration), Listing of color additives exempt from certification; sodium copper chlorophyllin. Federal Register. 67 (2002) 35429–35431.

[27] A. Mortensen, A. Geppel, HPLC–MS analysis of the green food colorant sodium copper chlorophyllin. Innov. Food Sci. Emerg. Technol. 8 (2007) 419–425.

[28] V. Chrastny, M. Komarek, Copper determination using ICP-MS with hexapole collision cell. Chem. Pap. 63 (2009) 512–519.

[29] S.-C. Wei, Y.-W. Lin, H.-T. Chang, Carbon dots as artificial peroxidases for analytical applications. J. Food Drug Anal. 28 (2020) 558–574.

[30] M. Batool, H.M. Junaid, S. Tabassum, F. Kanwal, K. Abid, Z. Fatima, A.T. Shah, Metal ion detection by carbon dots—a review. Crit. Rev. Anal. Chem. 52 (2022) 756–767.

[31] X. Gao, C. Du, Z. Zhuang, W. Chen, Carbon quantum dot-based nanoprobes for metal ion detection. J. Mater. Chem. C 4 (2016) 6927–6945.

doi:10.6342/NTU202300566

[32] A.-Q. Zheng, C.-X. Zhao, X.-J. Wang, Y. Shu, J.-H. Wang, Simultaneous detection and speciation of mono- and di-valent copper ions with a dual-channel fluorescent nanoprobe. Chem. Commun. 56 (2020) 15337–15340

[33] K.M. Omer, Highly passivated phosphorous and nitrogen co-doped carbon quantum dots and fluorometric assay for detection of copper ions. Anal Bioanal Chem 410 (2018) 6331–6336.

[34] A. Salinas-Castillo, D.P. Morales, A. Lapresta-Fernández, M. Ariza-Avidad, E. Castillo, A. Martínez-Olmos, A.J. Palma, L.F. Capitan-Vallvey, Evaluation of a reconfigurable portable instrument for copper determination based on luminescent carbon dots. Anal Bioanal Chem 408 (2016) 3013–3020.

[35] C. Li, W. Liu, X. Sun, W. Pan, G. Yu, J. Wang, Excitation dependent emission combined with different quenching manners supports carbon dots to achieve multi-mode sensing. Sens. Actuators B Chem. 263 (2018) 1–9.

[36] J.-H. Liu, S.-T. Yang, X.-X. Chen, H. Wang, Fluorescent carbon dots and nanodiamonds for biological imaging: preparation, application, pharmacokinetics and toxicity. Curr Drug Metab. 13 (2012) 1046–1056.

doi:10.6342/NTU202300566

[37] S. Chowdhury, B. Rooj, A. Dutta, U. Mandal, Review on Recent Advances in Metal Ions Sensing Using Different Fluorescent Probes. J Fluoresc 28 (2018) 999–1021.

[38] Y.-S. Lin, Y. L. Lin, A. P. Periasamy, J. S. Cang, H.-T. Chang, Parameters affecting synthesis of carbon dots for quantitation copper ions. Nanoscale adv. 1 (2019) 2553–2561.

[39] T. Boobalan, M. Sethupathi, N. Sengottuvelan, P. Kumar, P. Balaji, B. Gulyás, P. Padmanabhan, S. T. Selvan, A. Arun, Mushroom-derived carbon dots for toxic metal ion detection and as antibacterial and anticancer agents. ACS Appl. Nano Mater. 3 (2020) 5910–5919

[40] Y. Dong, R. Wang, G. Li, C. Chen, Y. Chi, G. Chen, Polyamine-Functionalized carbon quantum dots as fluorescent probes for selective and sensitive detection of copper ions. Anal. Chem. 84 (2012) 6220–6224.

[41] J. Zong, X. Yang, A. Trinchi, S. Hardin, I. Cole, Y. Zhu, C. Li, T. Muster, G. Wei, Carbon dots as fluorescent probes for “off–on” detection of Cu^{2+} and l-cysteine in aqueous solution. Biosens. Bioelectron. 51 (2014) 330–335.

doi:10.6342/NTU202300566

[42] J. Ci, Y. Tian, S. Kuga, Z. Niu, M. Wu, Y. Huang, One-pot green synthesis of nitrogen-doped carbon quantum dots for cell nucleus labeling and copper(II) detection. Asian J. Chem. 12 (2017) 2916–2921.

[43] D.D. Perrin, Stability of Metal Complexes with Salicylic Acid and Related Substances. Nature 182 (1958) 741–742.

[44] K. Yin, D. Lu, L. Wang, Q. Zhang, J. Hao, G. Li, H. Li, Hydrophobic Carbon Dots from Aliphatic Compounds with One Terminal Functional Group. J. Phys. Chem. C 123 (2019) 22447–22456.

[45] L. Lu, C. Feng, J. Xu, F. Wang, H. Yu, Z. Xu, W. Zhang, Hydrophobic-carbon-dot-based dual-emission micelle for ratiometric fluorescence biosensing and imaging of Cu^{2+} in liver cells. Biosens. Bioelectron. 92 (2017) 101–108.

[46] H. Peng, J. Travas-Sejdic, Simple aqueous solution route to luminescent carbogenic dots from carbohydrates. Chem. Mater. 21 (2009) 5563–5565.

[47] TFDA, Method of Identification for Sodium Copper Chlorophyllin in Foods. Taiwan Food and Drug Administration, 2013.

[48] U.S. Epa, Test methods for evaluating solid waste—physical chemical methods, SW-846. Washington [DC]: US Environmental Protection Agency, 1997.Q. Qiu, L. Lai, J. Cheng, J. Wu, Recent advances in the sulfonylation of alkenes with the

insertion of sulfur dioxide via radical reactions. Chem. Commun. 54 (2018) 10405–10414.

[49] L.P. Kuhn, A.H. Corwin, The behavior of organic acids and esters in sulfuric acid. J. Am. Chem. Soc. 70 (1948) 3370–3375.

[50] C.S. Estes, A.Y. Gerard, J.D. Godward, S.B. Hayes, S.H. Liles, J.L. Shelton, T.S. Stewart, R.I. Webster, H.F. Webster, Preparation of highly functionalized carbon nanoparticles using a one-step acid dehydration of glycerol. Carbon. 142 (2019) 547–557.

[51] C. S. Hiremath, J. Tonannavar, Vibrational assignments and effect of aldehyde rotation on substituents in some trisubstituted benzaldehydes. Spectrochim. Acta A Mol. Biomol. Spectrosc. 73 (2009) 388–397.

[52] J.C. Vinci, I.M. Ferrer, N.W. Guterry, V.M. Colon, J.F. Destino, F.V. Bright, L.A. Colon, Spectroscopic characteristics of carbon dots (C-dots) derived from carbon fibers and conversion to sulfur-bridged C-dots nanosheets. Appl. Spectrosc. 69 (2015) 1082–1090.

[53] K.M. Chan, D.D. Huang, Y.J. Li, M.N. Chan, J.H. Seinfeld, C.K. Chan, Oligomeric products and formation mechanisms from acid-catalyzed reactions of methyl vinyl ketone on acidic sulfate particles. J. Atmos. Chem. 70 (2013) 1–18.

[54] H. Ding, S.-B. Yu, J.-S. Wei, H.-M. Xiong, Full-Color Light-Emitting Carbon dots with a surface-state-controlled luminescence mechanism. ACS Nano. 10 (2016) 484–491.

[55] T. Song, Y. Zhao, K. Matras-Postolek, P. Yang, Color-tunable carbon dots via control the degree of self-assembly in solution at different concentration. J. Lumin. 212 (2019) 69–75

[56] TFDA, The use range and limit of food additives. Taiwan Food and Drug Administration, 2019.

[57] T.-H. Ji, X.-L. Li, Y. Mao, Z. Mei, Y. Tian, Electron/energy co-transfer behavior and reducibility of Cu-chlorophyllin-bonded carbon-dots. RSC Adv. 10 (2020) 31495–31501.

[58] X. Zheng, W. Liu, Q. Gai, Z. Tian, S. Ren, A carbon-dot-based fluorescent probe for the sensitive and selective detection of copper(II) ions. ChemistrySelect 4 (2019) 2392–2397.

[59] N. Papaioannou, A. Marinovic, N. Yoshizawa, A.E. Goode, M. Fay, A. Khlobystov, M.-M. Titirici, Structure and solvents effects on the optical properties of sugar-derived carbon nanodots. Sci Rep 8 (2018) 6559.

[60] Y. Kuang, L. Chen, J. Lu, C. Yang, Y. Li, L. Lu, Y. Nie, A carbon-dot-based dual-emission probe for ultrasensitive visual detection of copper ions. New J. Chem. 42 (2018) 19771–19778.

[61] X. Ma, S. Lin, Y. Dang, X. Zhang, F. Xia, Carbon dots as an “on-off-on” fluorescent probe for detection of Cu(II) ion, ascorbic acid, and acid phosphatase. Anal. Bioanal. Chem. 411 (2019) 6645–6653.

[62] Y.X. Mu, Q.F. Zhuang, S.P. Huang, M.Y. Hu, Y. Wang, Y.N. Ni, Adenine-stabilized carbon dots for highly sensitive and selective sensing of copper(II) ions and cell imaging. Spectrochim. Acta A 239 (2020) 118531.

[63] N. Chaudhary, P.K. Gupta, S. Eremin, P.R. Solanki, One-step green approach to synthesize highly fluorescent carbon quantum dots from banana juice for selective detection of copper ions. J. Environ. Chem. Eng 8 (2020) 103720.

[64] United States Environmental Protection Agency, National Primary Drinking Water Regulations. https://www.epa.gov/ground-water-and-drinking-water/national-primary-drinking-water-regulations#Inorganic (accessed 14 July 2021).

[65] X. Ma, Y. Dong, H. Sun, N. Chen, Highly fluorescent carbon dots from peanut shells as potential probes for copper ion: The optimization and analysis of the synthetic process. Mater. Today Chem. 5 (2017) 1–10.

doi:10.6342/NTU202300566

[66] L. Liu, H. Gong, D. Li, L. Zhao, Synthesis of carbon dots from pear juice for fluorescence detection of Cu^{2+} ion in water. J. Nanosci. Nanotechnol. 18 (2018) 5327–5332.

[67] M.-C. Rong, K.-X. Zhang, Y.-R. Wang, X. Chen, The synthesis of B, N-carbon dots by a combustion method and the application of fluorescence detection for Cu^{2+}. Chin. Chem. Lett. 28 (2017) 1119–1124.

[68] X.F. Hou, F. Zeng, F.K. Du, S.Z. Wu, Carbon-dot-based fluorescent turn-on sensor for selectively detecting sulfide anions in totally aqueous media and imaging inside live cells. Nanotechnology 24 (2013) 335502.

[69] L. Zhao, H. Li, Y. Xu, H. Liu, T. Zhou, N. Huang, Y. Li, L. Ding, Selective detection of copper ion in complex real samples based on nitrogen-doped carbon quantum dots. Anal. Bioanal. Chem. 410 (2018) 4301–4309.

[70] Y. Wang, W.-T. Wu, M.-B. Wu, H.-D. Sun, H. Xie, C. Hu, X.-Y. Wu, J.-H. Qiu, Yellow-visual fluorescent carbon quantum dots from petroleum coke for the efficient detection of Cu^{2+} ions. New Carbon Mater. 30 (2015) 550–559.

doi:10.6342/NTU202300566

Table 3-1. Determination of SCC in non-alcoholic flavored drinks.

Sample	Concentration (μM)	Added (μM)	Total concentration (μM)	Recovery (%, n=3)	RSD[d] (%, n=3)
1[a]	1.17	1.57	2.71	98	0.9
	1.17	3.15	4.33	100	1.2
	1.20	4.72	6.06	103	1.0
2[b]	ND[c]	1.57	1.62	103	1.1
	ND[c]	3.15	3.19	101	1.1
	ND[c]	4.72	4.81	102	1.1

[a] green milk tea containing SCC was diluted 5-fold.

[b] green milk tea without containing SCC was diluted 5-fold.

[c] not detected.

[d] RSD value of triplicate experiments of standard addition

doi:10.6342/NTU202300566

Table 3-2. Comparison of the detection of Cu^{2+} ions using CDs prepared from different precursors.

Precursor	Sensing Mechanism	Linear range (μM)	LOD (μM)	Ref.
Peanut shells	Static quenching	0–50	4.8	65
Pear juice	Not provided	1.6–787	1.6	66
Aminophenylboronic acid	Static quenching	1–25	0.3	67
Citric acid	Static quenching	5.16–20	1.72	68
Citric acid and histidine	Dynamic quenching	0.6–30	0.19	69
Petroleum coke	PET*	0.25–10	0.029	70
Triolein	PET	0.5–10	0.21	This study

PET: photoinduced electron transfer

doi:10.6342/NTU202300566

Table 3-3. Tolerance of hydrophilic TO-C dots with interfering ions in soil sample in the presence of 10 μM Cu^{2+} ions.

Interfering ions	Adding concentration (μM)	RSD[a] (%, $n = 3$)
Al^{3+}	1000	2.2
Ca^{2+}	500	2.4
Fe^{3+}	300	2.3
Mg^{2+}	500	1.6
K^{+}	500	0.9
Zn^{2+}	500	2.1
Co^{2+}	100	1.9
Ni^{2+}	100	1.1
Cr^{3+}	100	1.7
Pb^{2+}	200	1.9

[a] RSD value of triplicate detections of Cu^{2+} ions in the presence of interfering ions.

doi:10.6342/NTU202300566

Table 3-4. Determination of Cu^{2+} in soil sample (Montana Soil, SRM 2710).

Sample	Amount (mg g^{-1})	Added (mg g^{-1})	Total amount (mg g^{-1})	Recovery (%, n=3)	RSD (%, n=3)
Montana Soil	2.93	2.95	5.81	97.7	1.01
	2.96	5.90	8.79	98.8	1.59
	2.97	8.85	11.7	98.4	2.04

Reference value of Cu in Montana Soil (SRM 2710) is 2.95 mg g^{-1}.

doi:10.6342/NTU202300566

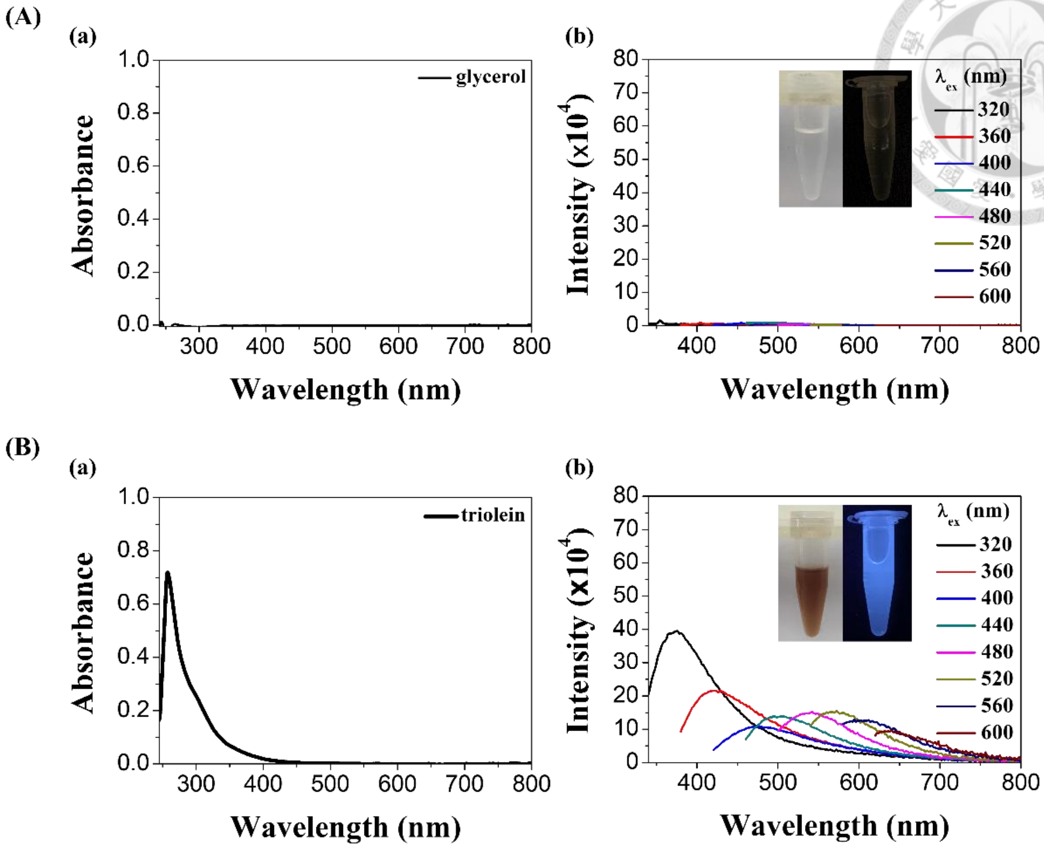

Figure 3-1. (a) UV-vis absorption and (b) fluorescence spectra under different excitation wavelengths (from 320 to 600 nm; in 40 nm increments) of (A) glycerol (50 mM) and (B) triolein (50 mM) after reacting with sulfuric acid (6.75 M) in ethyl acetate for 3 h. The obtained products were diluted 200-fold in ethyl acetate prior to the measurements. Insets to (b): photographs of the corresponding solutions upon excitation with a hand-held UV lamp (365 nm).

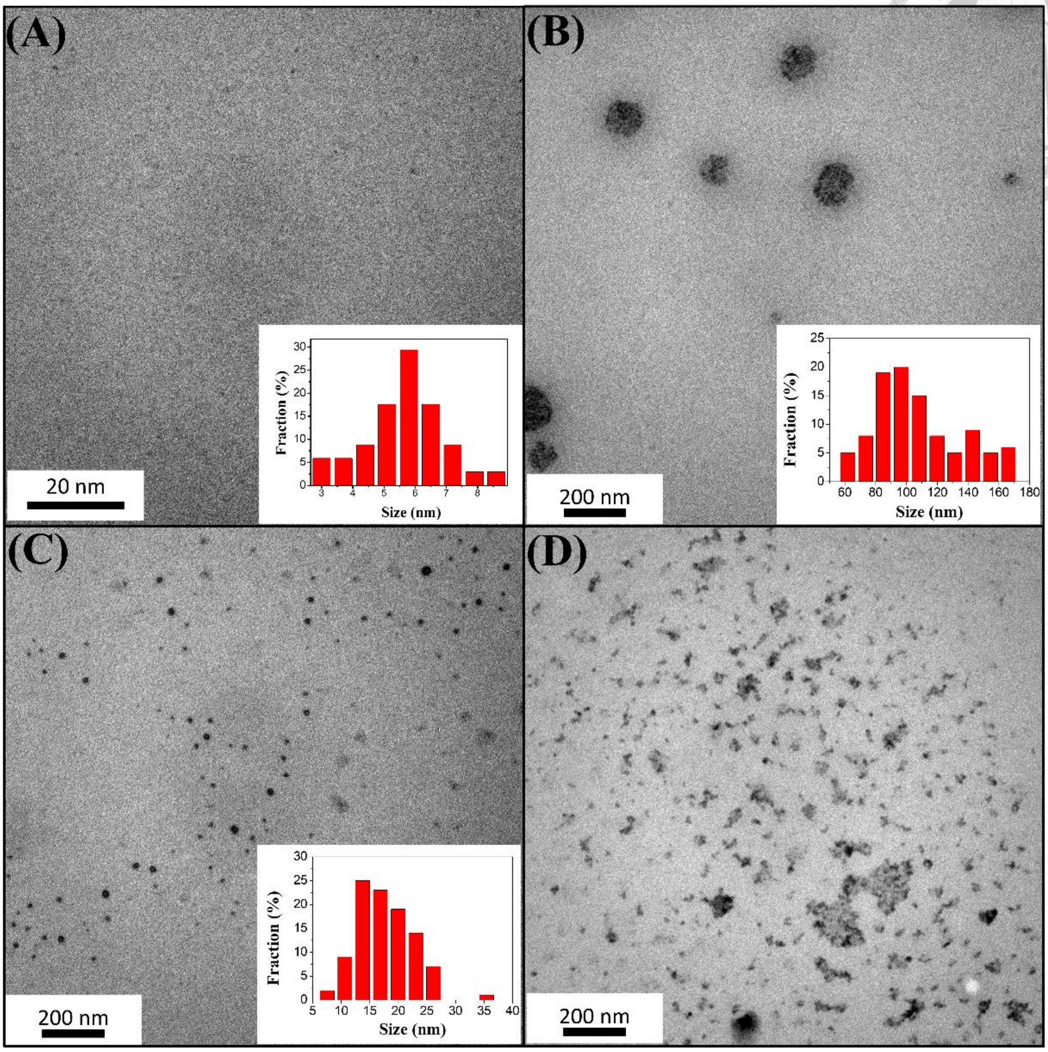

Figure 3-2. TEM images of hydrophobic TO-C dots at the concentration of (A) 0.66 mg mL^{-1} and (B) 33 mg mL^{-1} in ethyl acetate. (C) and (D) hydrophilic TO-C dots (100 μg mL^{-1}) in the absence and presence of 10 μM Cu^{2+} ions in sodium phosphate buffer (10 mM, pH 8.0).

doi:10.6342/NTU202300566

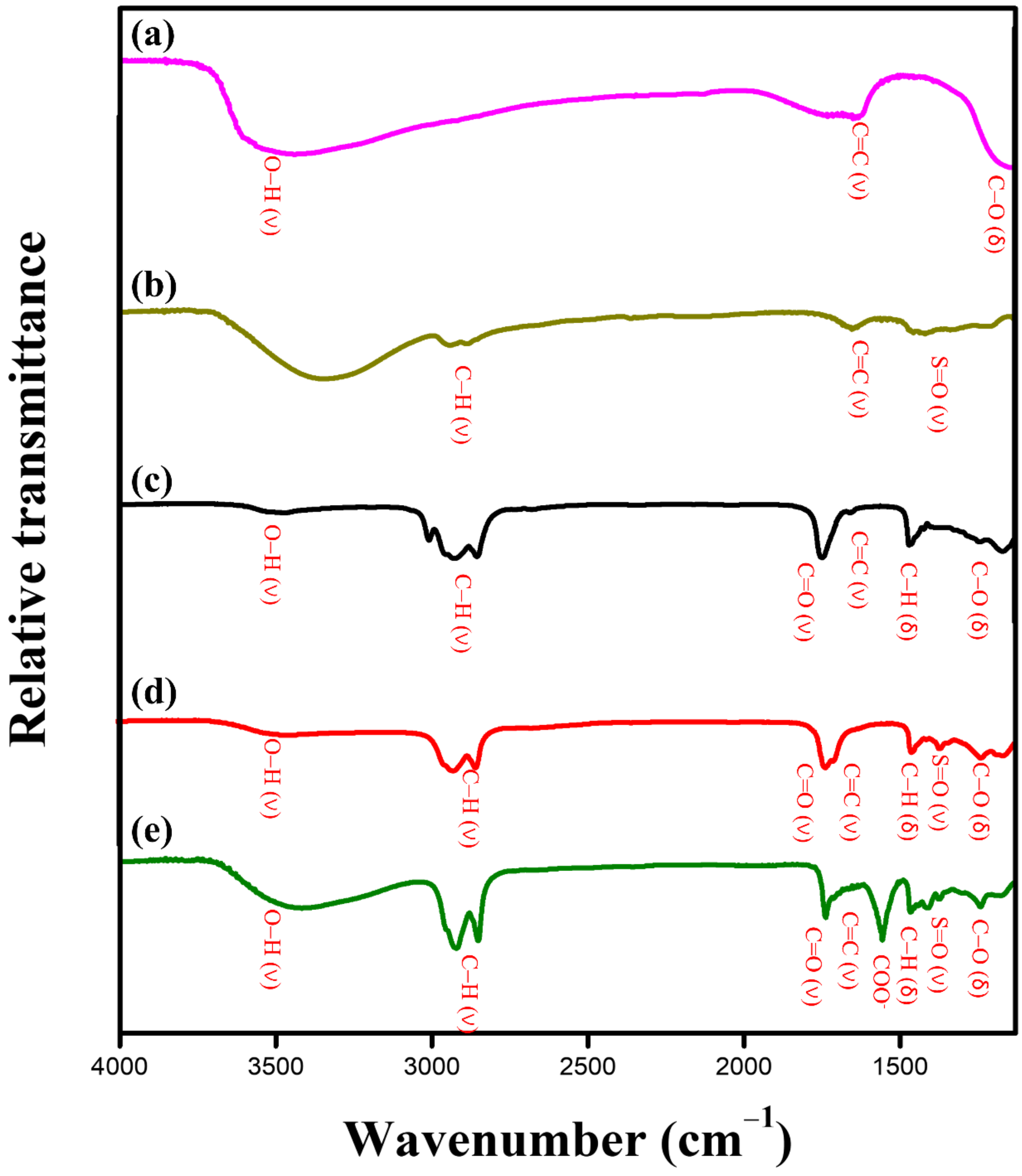

Figure 3-3. FTIR spectra of (a) glycerol, (b) the products of glycerol reacted with H_2SO_4, (c) triolein, (d) hydrophobic TO-C dots, and (e) hydrophilic TO-C dots.

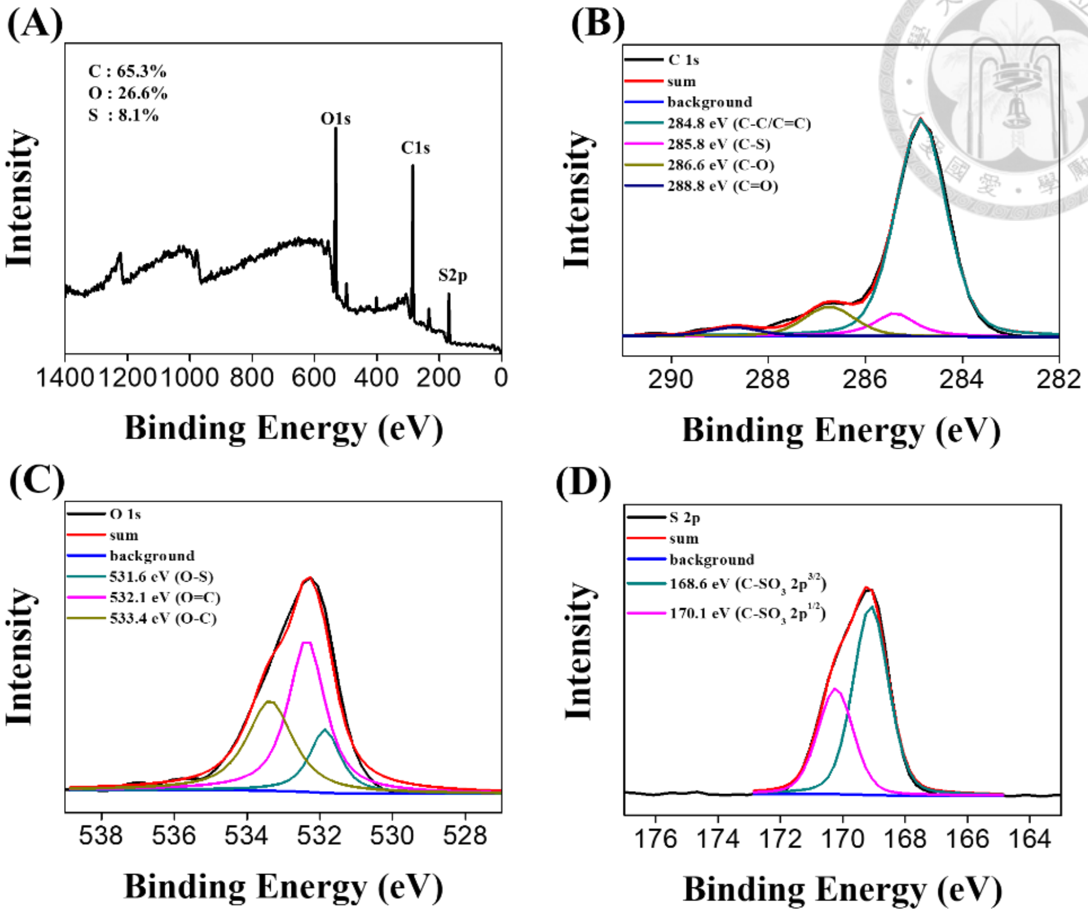

Figure 3-4. (A) Survey XPS spectrum, (B–D) deconvoluted spectra of (B) C1s, (C) O1s, and (D) S2p core level XPS spectra of hydrophobic TO-C dots.

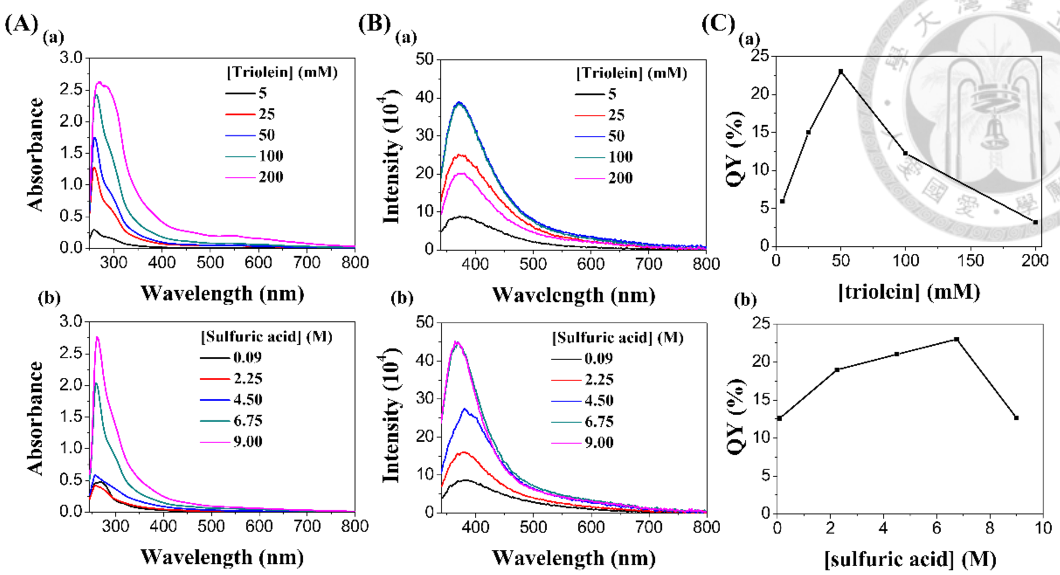

Figure 3-5. (A) UV-vis absorption and (B) fluorescence spectra, and (C) QY of hydrophobic TO-C dots prepared from the triolein reacted with sulfuric acid at the concentration of (a) sulfuric acid (6.75 M)/triolein (5–200 mM) and (b) sulfuric acid (0.09–9.00 M)/triolein (50 mM). The excitation wavelength is 320 nm for the collection of fluorescence spectra.

doi:10.6342/NTU202300566

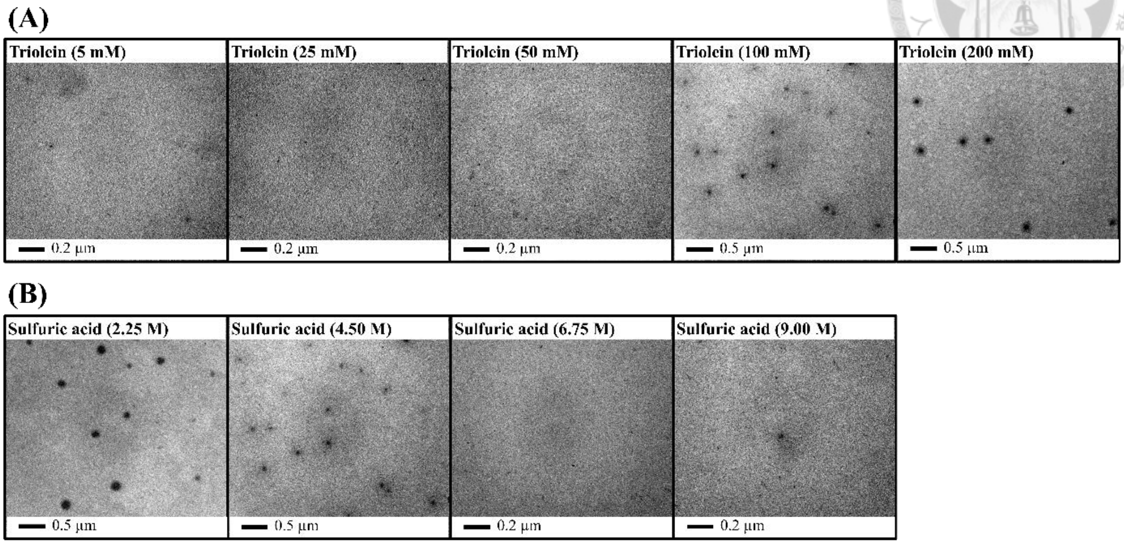

Figure 3-6. TEM images of TO-C dots obtained from triolein reacted with sulfuric acid; (A) sulfuric acid (6.75 M)/triolein (5–200 mM) and (B) sulfuric acid (2.25–9.00 M)/triolein (50 mM). The obtained CDs were dispersed in ethyl acetate.

doi:10.6342/NTU202300566

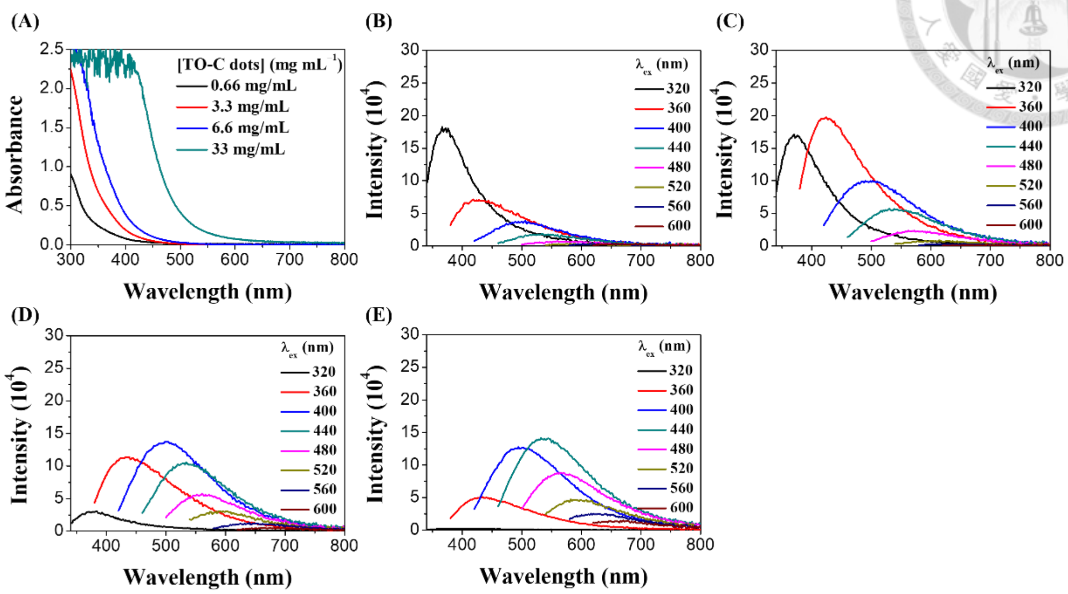

Figure 3-7. (A) UV-vis absorption spectra of hydrophobic TO-C dots (0.66–33 mg mL^{-1}). (B–E) Fluorescence spectra of hydrophobic TO-C dots at the concentrations of (B) 0.66, (C) 3.3, (D) 6.6, and (E) 33 mg mL^{-1} under different excitation wavelengths (from 320 to 600 nm; in 40 nm increments). The hydrophobic TO-C dots were dispersed in ethyl acetate.

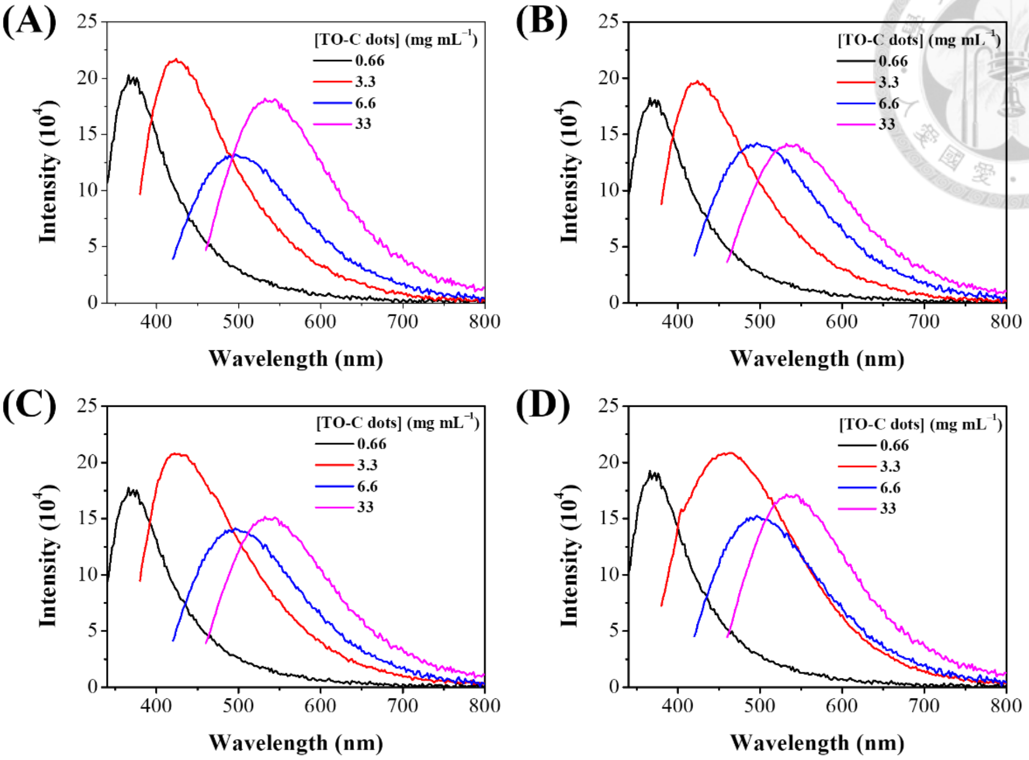

Figure 3-8. Concentration-dependent fluorescence properties of hydrophobic TO-C dots over the concentration range of 0.66–33 mg mL^{-1} in different solvents (A) toluene, (B) ethyl acetate, (C) dimethyl sulfoxide, and (D) ethanol.

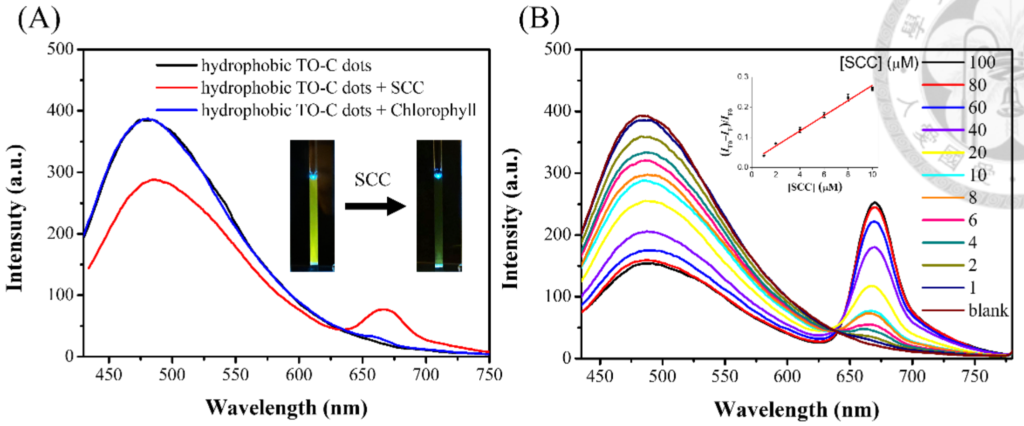

Figure 3-9. (A) Fluorescence spectra of hydrophobic TO-C dots in the absence (black curve) and presence of SCC (10 μM; red curve) or chlorophyll (10 μM; blue curve). (B) Fluorescence spectra of hydrophobic TO-C dots in the presence of different concentrations of SCC (0–100 μM) in ethyl acetate/acetone solution (5:1, v/v). The concentration of hydrophobic TO-C dots was 1.0 mg mL^{-1}. I_{F0} and I_F are the fluorescence intensities of hydrophobic TO-C dots at 500 nm in the absence and presence of SCC, respectively, at an excitation wavelength of 400 nm. Inset to (A) shows the photographs of TO-C dots solutions before and after adding SCC (10 μM).

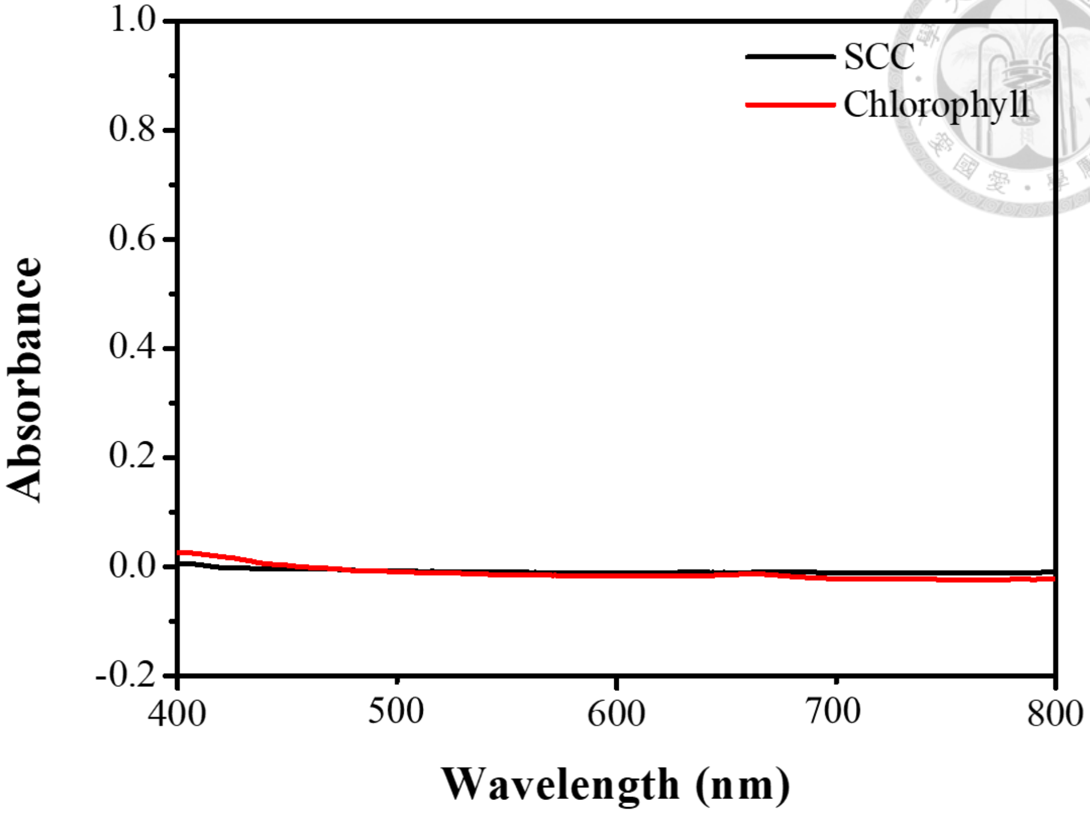

Figure 3-10. Absorption spectra of SCC (10 μM) and chlorophyll (10 μM) in ethyl acetate/acetone solution (5:1, v/v).

doi:10.6342/NTU202300566

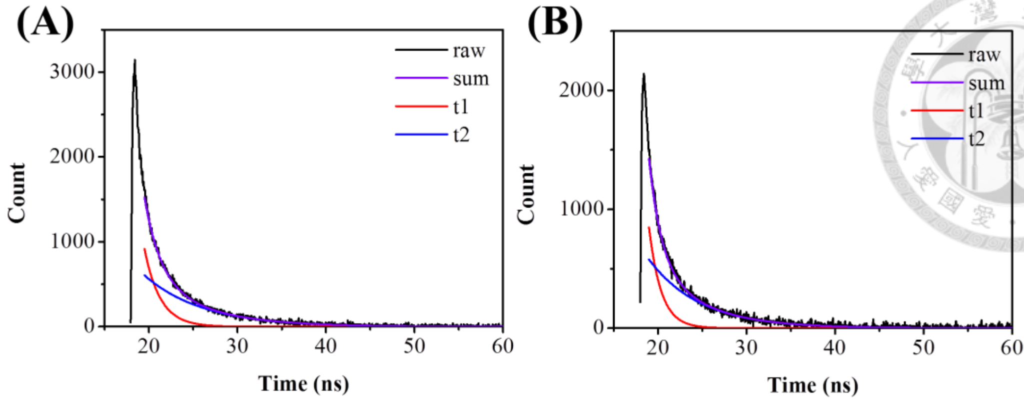

Figure 3-11. Fluorescence decay curves of hydrophobic TO-C dots (1.0 mg mL^{-1}) in ethyl acetate:acetone (5:1) solution in the (A) absence and (B) presence of SCC (10 μM) upon excitation using a 365-nm pulsed laser. The fluorescence decay was fitted to a biexponential decay and the lifetime of (A) and (B) were determined to be 1.788/6.594 ns (60.20/39.80%) and 1.383/5.781 ns (59.44/40.56%) (τ_1/τ_2).

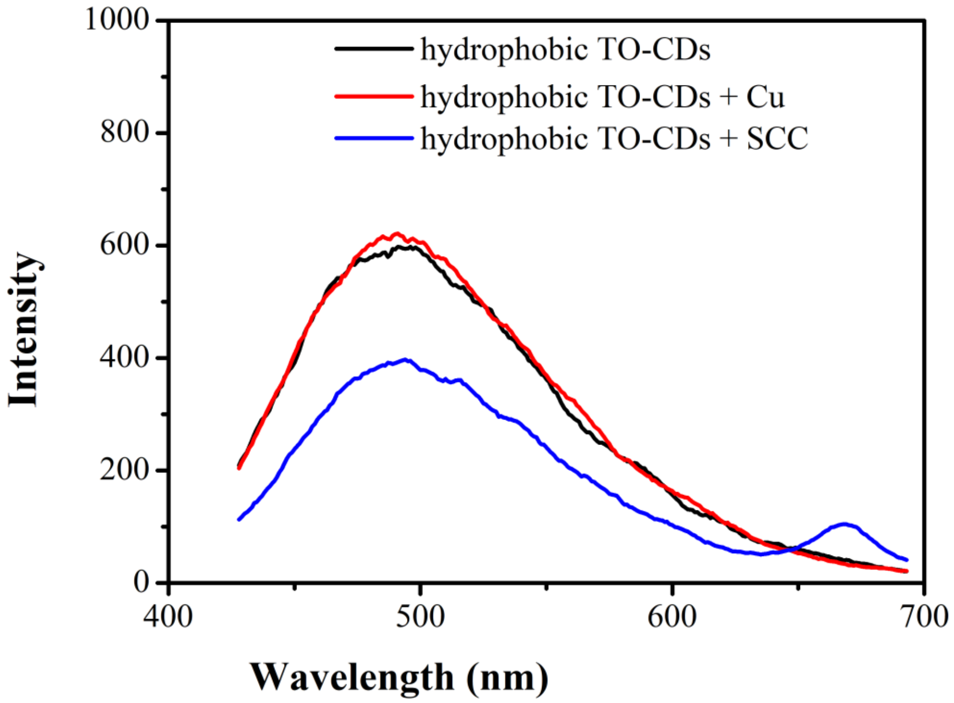

Figure 3-12. Fluorescence spectra of hydrophobic TO-C dots in the absence (black line) and in the presence of Cu^{2+} ions (10 μM; red line) or SCC (10 μM; blue line) in ethyl acetate/acetone solution (5:1, v/v).

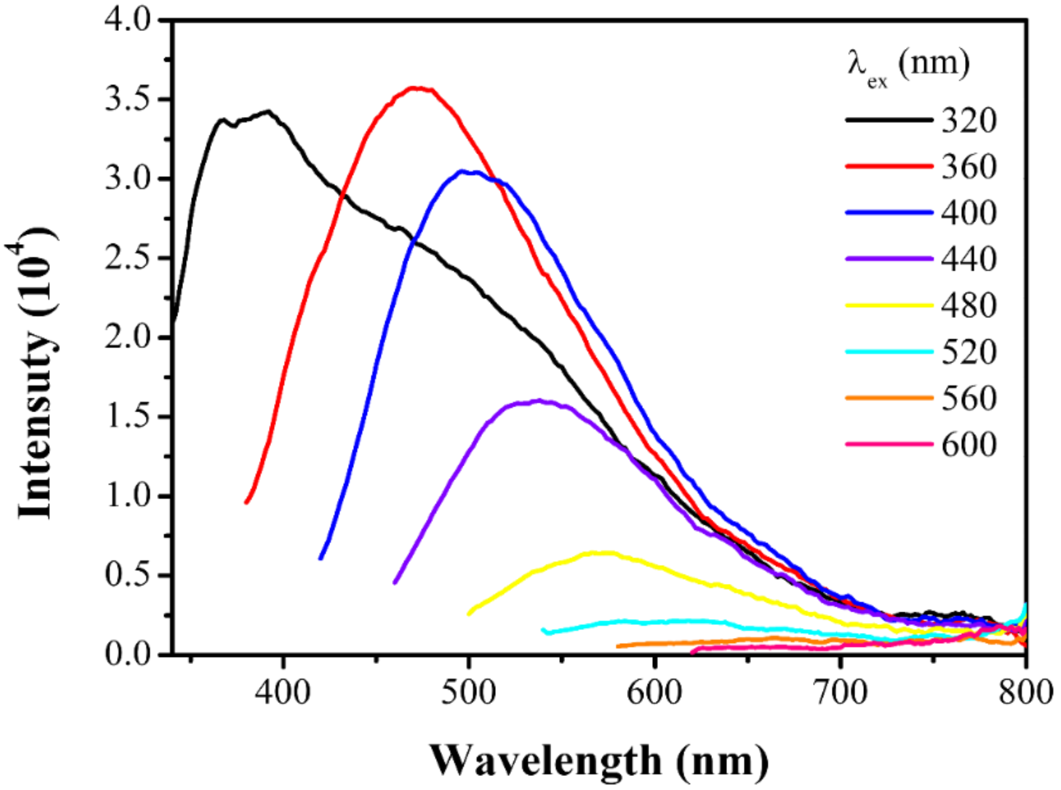

Figure 3-13. Fluorescence spectra of hydrophilic TO-C dots (0.1 mg mL^{-1}) in 10 mM sodium phosphate (pH 8.0) solution under excitation from 320 nm to 600 nm.

doi:10.6342/NTU202300566

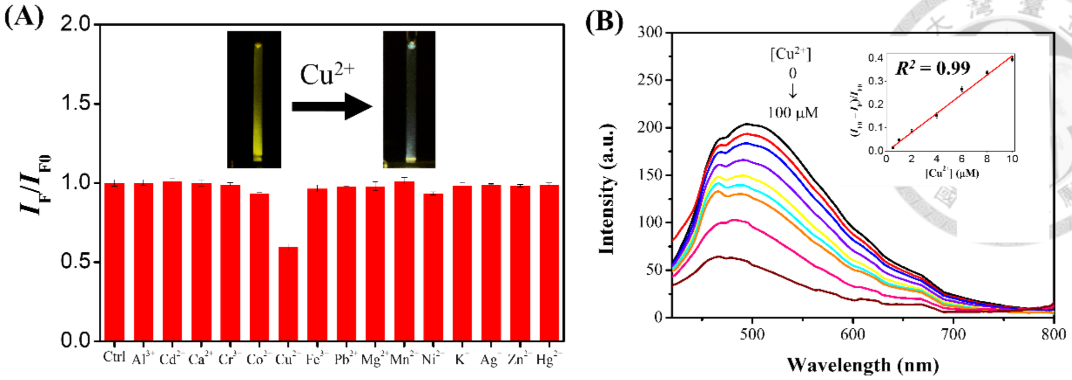

Figure 3-14. (A) Selectivity of the hydrophilic TO-C dots probe toward Cu^{2+} ions against other metal ions and (B) fluorescence spectra of the TO-C dots at various Cu^{2+} concentrations (0–100 μM) in sodium phosphate buffer (10 mM, pH 8.0). The concentrations of hydrophilic TO-C dots in (A) and (B) were both 100 μg mL^{-1}. I_{F0} and I_F are the fluorescence intensities of the TO-C dots at 500 nm in the absence and presence of Cu^{2+}, respectively, at an excitation wavelength of 400 nm. The concentrations of all metal ions in (A) are 10 μM. Inset to (A) shows the photographs of the hydrophilic TO-C dots solutions before and after adding $CuCl_2$ (10 μM) upon excitation with a hand-held UV lamp (365 nm). Error bars represent the standard deviations of experiments in triplicates.

doi:10.6342/NTU202300566

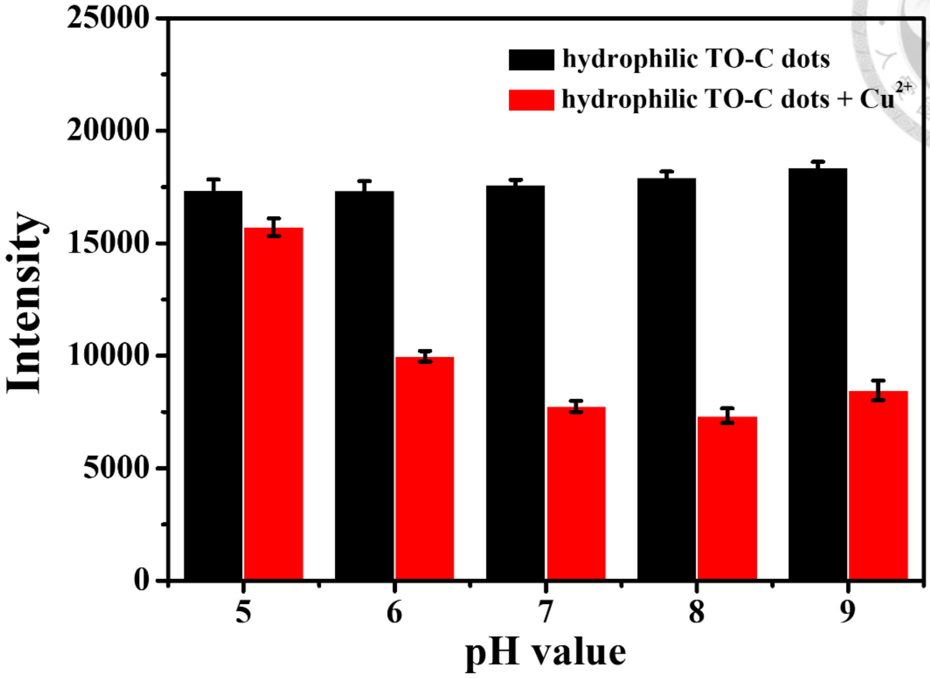

Figure 3-15. Fluorescence intensities of hydrophilic TO-C dots (100 μg mL^{-1}) in sodium phosphate buffer solution (10 mM, pH 5−9) at 500 nm in the absence and presence of Cu^{2+} ions (50 μM) when excited at 400 nm. Error bars represent the standard deviations of experiments in triplicate.

doi:10.6342/NTU202300566

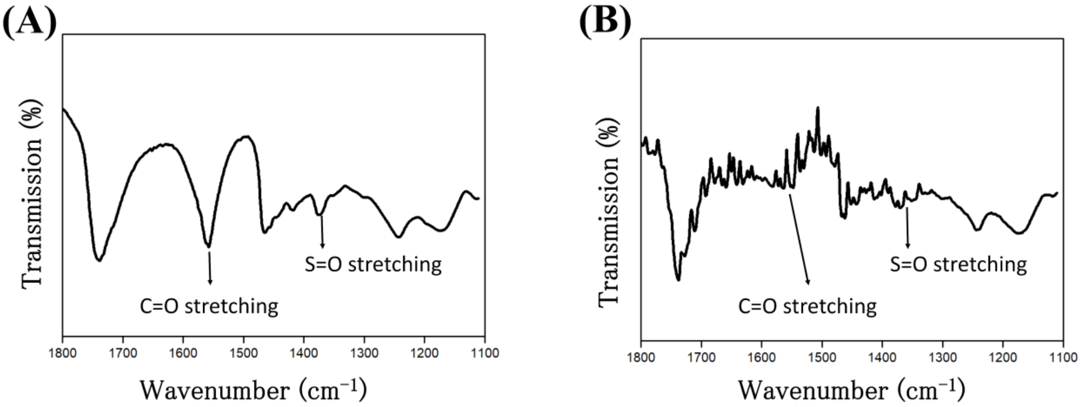

Figure 3-16. FT-IR spectra of hydrophilic TO-C dots (100 μg mL^{-1}) in the (a) absence and (b) presence of Cu^{2+} ions (10 μM).

doi:10.6342/NTU202300566

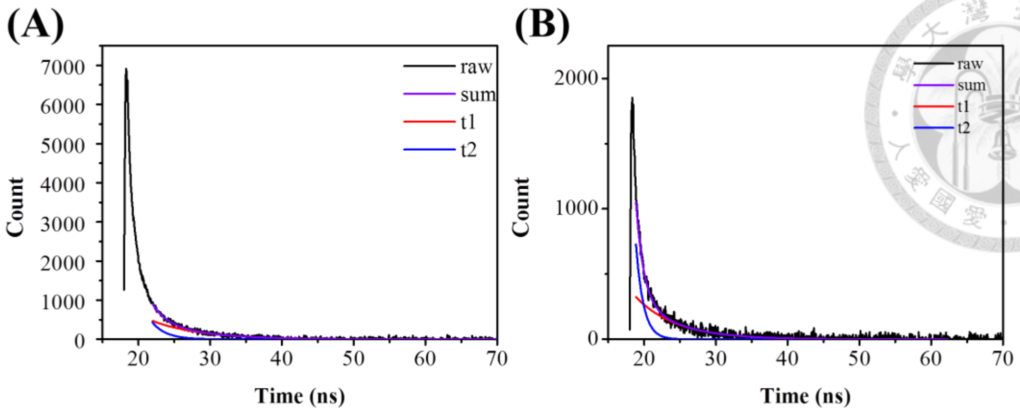

Figure 3-17. Fluorescence decay curves of hydrophilic TO-C dots (1.0 mg mL^{-1}) in the (a) absence and (b) presence of Cu^{2+} ions (10 μM) upon excitation using a 365-nm pulsed laser. The fluorescence decay was fitted to a biexponential decay and the lifetime of (a) and (b) were determined to be 1.943/6.773 ns (47.81/52.19%) and 1.055/5.711 ns (69.24/30.76%) (τ_1/τ_2).

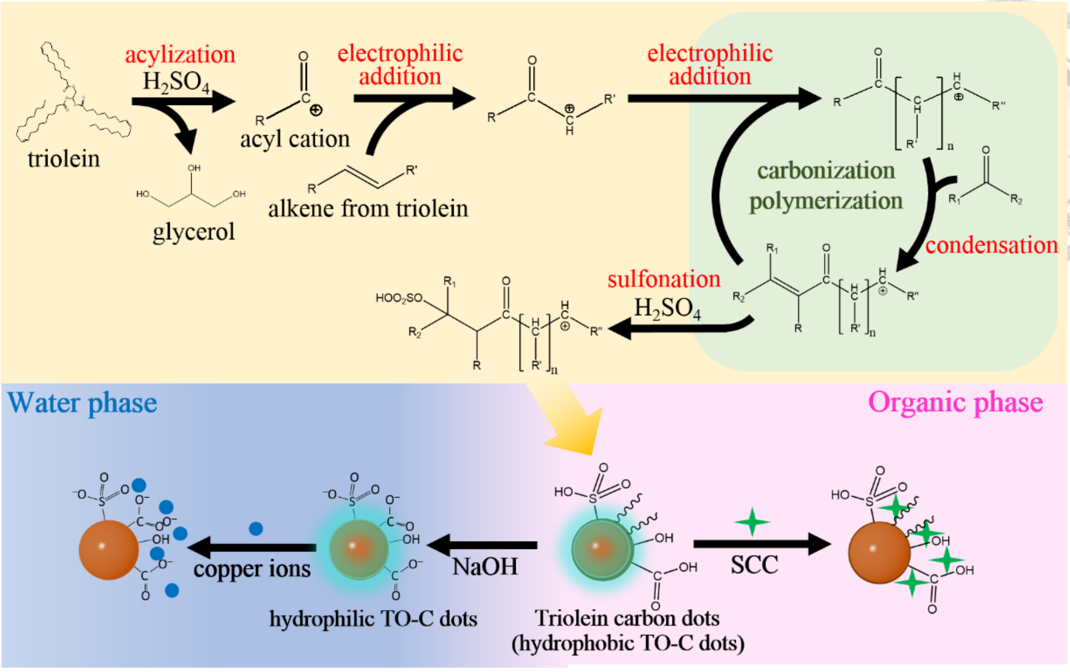

Scheme 3-1. Schematic representation of the preparation of hydrophobic TO-C dots from triolein and H_2SO_4 through a chemical oxidation route, and conversion of hydrophobic TO-C dots to hydrophilic TO-C dots through alkaline hydrolysis. Their separate applications for the detection of SCC and Cu^{2+} ions are also depicted.

Chapter 4 Development of fluorescent carbon nanoparticle-based probes for intracellular pH and hypochlorite sensing

The content in this chapter has been published to: Y.-S. Lin, L.-W. Chuang, Y.-F. Lin, S.-R. Hu, C.-C. Huang, Y.-F. Huang, H.-T. Chang, Development of Fluorescent Carbon Nanoparticle-Based Probes for Intracellular pH and Hypochlorite Sensing. Chemosensors 10 (2022) 64.

4.1 Introduction

Many biological functions such as respiratory acidosis[1], lysosomal functions[2], and tumor growth[3] are related to the intracellular pH value. Thus, variation of pH values in biological fluids is usually an index for physiological disorders. For example, the extracellular pH of tumor tissue is lower than that of normal tissue.[4] In addition to pH value, the level and species of reactive oxygen species (ROS) inside cells are also important to be carefully monitored because they have been shown related to cell signalling like apoptosis and gene expression.[5] Although high concentrations of ROS inside cells could induce carcinogenesis and cell damage, appropriate ROS level is essential for some cellular functions like differentiation. Hypochlorite is one of important ROS, which is produced from peroxidation of chloride ions catalyzed by myeloperoxidase (MPO) inside cells.[6] Although hypochlorite plays an important role in immune system, it at high levels might cause several diseases such as cancer and neuron degeneration.[6,7] Thus, techniques for monitoring of cellular pH value and ROS level are needed.

Many organic molecules and nanomaterials based fluorescent probes have been shown sensitive for monitoring of cellular pH values.[8] Most of the sensing strategies are based on the fact that the fluorescent properties of the probes are pH dependent. For example, we demonstrated a dual emission probe that uses BSA-Au/Ce nanoclusters to

doi:10.6342/NTU202300566

monitor cellular pH values, in which the fluorescence intensity of BSA-Ce complex at 410 nm is pH dependent, but that for Au NCs at 650 nm is pH independent.[9] The ratiometric fluorescence approach was validated by measuring the local pH values inside cancer cells. Chen et al. designed another fluorescent probe based on Förster resonance energy transfer (FRET) between a pH-insensitive fluorophore [poly(9,9-dioctylfluorenyl-2,7-diyl), λ_{em} = 439 nm] and a pH-sensitive fluorescent dye (fluorescein isothiocyanate, λ_{em} = 517 nm) in the semiconducting polymer dots (Pdots-PPF). Upon a single excitation at 380 nm, the Pdots-PPF exhibit ratiometric pH sensing ability within a wide range of pH value ranging from 3.0 to 8.0.[10] Recently, fluorescent carbon based-nanoparticles have received great interest due to their low chemical/cytotoxicity, good biocompatibility, multicolor luminescence tunability and resistance to photobleaching.[11-13] Carbon dots (CDs) prepared by a variety of carbon sources in facile methods have shown significantly improved behaviors and demonstrated as a suitable candidate for fluorescent pH sensing.[13-17]

Relatively, fluorescent probes for determining cellular hypochlorite contents are rare.[18-20] The sensing mechanism behind these probes mainly relies on the strong oxidation property of hypochlorite. For example, Zhong et al. developed an aggregation-induced emission probe based on benzothiazole derivatives (BTD) for hypochlorite detection.[21] The recognition of BTD by hypochlorite involves C=N

doi:10.6342/NTU202300566

cleavage and hydrolysis to aldehyde groups. A ratiometric fluorescent probe for hypochlorite was constructed by co-embedding aminocyanine dye and Rhodamine B within a silica nanoparticle to form a FRET pair. [22] It is hypothesized that the nitrogen substitution at the polymethine can be served as a better ROS chemosensor due to its lower oxidation potential. The pioneer work from Yin et al. reported the determination of hypochlorite in a dual-readout mode based on the blue emission CDs with down and up conversion luminesce characteristics.[23] Increasing efforts have been devoted to fabricate CDs with enhanced photoluminescence (PL) properties to detect hypochlorite in real samples.[24-27] It has been found that CDs doped with heteroatoms such as nitrogen or tethered to other functional units can lead to a red-shift in emission and greater reactivity toward hypochlorite.[28-31] It can provide sensitive and selective responses to the hypochlorite in biological systems.

Inspired by the above-mentioned circumstances, we synthesized fluorescent carbon nanoparticles (CNPs) from *m*-phenylenediamine (*m*-PD) and ascorbic acid (AA) through a hydrothermal route to monitor cellular pH and hypochlorite levels. The combination of *m*-PD and AA not only increases the diversity of functional groups, but also brings more active sites, thereby enhancing their responses to target analytes. We investigated several important factors, including molar ratio of *m*-PD/AA and synthesis temperature that affect the formation of the nanoparticles (mPA CNPs). At the optimal

doi:10.6342/NTU202300566

sensing conditions, mPA CNPs showed pH-dependent fluorescence properties over the range of 5.5-8.5, indicating that they are promising for monitoring pH fluctuations in living cells. Under the physiological condition, the probe also showed great sensitivity and selectivity for the quantitation of hypochlorite. We evaluated the possible fluorescence quenching mechanisms of mPA CNPs in response to changes in pH and hypochlorite. The probe was further validated by monitoring cellular pH values and hypochlorite levels, showing their greater potential for cell imaging and real-time sensing.

4.2 Experimental Section

4.2.1 Materials

Ammonium oxalate (>98%), L-(+)-ascorbic acid (AA, ≧99.8%), monosodium hydrogen phosphate (98%), *m*-phenylenediamine (*m*-PD, >99%), and sodium periodate (99%) were purchased from Acros Organics (Geel, Belgium). Disodium hydrogen phosphate (98%), sodium borohydride (≧98%), %), sodium phosphate (96%), 2'-7'dichlorofluorescin diacetate (DCFH-DA), Hoechst 33342, potassium nitrite (>96%), potassium dioxide (99%), hydrogen peroxide (36%), iron chloride (> 98.0%), dimethyl sulfoxide (DMSO, >99.5%) and sulfuric acid (95−98%) were purchased from Sigma-

doi:10.6342/NTU202300566

Aldrich (St. Louis, MO, USA). Sodium hydroxide (pellet, >98%) was purchased from Macron Fine Chemicals (Center Valley, PA, USA). Sodium nitrite was purchased from Thermo Fisher Scientific (Waltham, USA). Sodium hypochlorite (NaClO) (10-12%) was purchased from Aencore (Surrey Hills, Australia). Ultrapure water (18.2 MΩ cm) from a Milli-Q ultrapure system was used in this study.

Superoxide (O_2^-) was generated by dissolving KO_2 in DMSO. Hydroxyl radical ($^{\cdot}OH$) was generated by the Fenton reaction. Typically, hydrogen peroxide (H_2O_2, 10 eq) was added to $FeCl_2$ in ultrapure water. Peroxynitrite ($ONOO^-$) was prepared by adding 0.6 M KNO_2, 0.6 M HC1 and 0.7 M H_2O_2 to a 3 M NaOH solution at 0°C. The concentration of $ONOO^-$ was estimated by using the extinction coefficient of 1670 cm^{-1} M^{-1} at 302 nm in 0.1 M aqueous sodium hydroxide solutions. NaClO and H_2O_2 were diluted in ultrapure water.

4.2.2 Cells culture

Murine prostate cancer cell line Tramp C1 cells were cultured in Dulbecco’s modified Eagle medium (DMEM) containing fetal bovine serum (10%) and penicillin/streptomycin (1%) under a humidified atmosphere of 5% CO_2 in air at 37 °C. The medium was purchased from ThermoFisher Scientific (Waltham, Massachusetts, USA).

doi:10.6342/NTU202300566

4.2.3 Instruments

A monochromatic microplate spectrophotometer (Synerg H1) form Biotek Instruments, (Santa Clara, California, USA) was used for the fluorescence measurement. A transmission electron microscope (TEM) (H-7100) from Hitachi (Tokyo, Japan) was used to record TEM images of the synthetic products. Field emission transmission electron microscope (FE-TEM) (JEM-2100F) form JEOL (Akishima, Tokyo, Japan) was further used to record their images. Their X-ray photoelectron spectroscopy (XPS) spectra were taken with a system (PHI 5000 VersaProbe III) from ULVAC-PHI (Chigasaki, Kanagawa, Japan). A Fourier transform infrared (FT-IR) spectrophotometer (Varian640-IR) from Varian (Palo Alto, California, USA) was employed to record their FT-IR spectra. Their ultraviolet-visible (UV-Vis) absorption spectra were taken using a spectrophotometer (Evolution 220; from ThermoFisher Scientific (Waltham, Massachusetts, USA). Their fluorescence spectra were measured using a spectrofluorometer (SF5) from Edinburgh Instruments (Livingston, England). A FluoTime 300 system from PicoQuant (Berlin, Germany) with a diode laser emitting at 375 nm was used as the light source to record the fluorescence decay of mPA CNPs.

doi:10.6342/NTU202300566

4.2.4 Synthesis of mPA CNPs

A hydrothermal method at various temperatures (170–260 ˚C; 260 ˚C is the highest temperature allowed by our heating system) was applied for the synthesis of mPA CNPs from different amounts of *m*-PD (50 mM) and AA (25–100 mM). Based on the yield, stability, and optical properties of the product, reaction temperature at 260 °C for 2 h, 50 mM of *m*-PD, 50 mM of AA, and solution pH of 4.0 were selected. In brief, *m*-PD (54 mg, 0.5 mmol) and AA (88 mg, 0.5 mmol) were dissolved in 10 mL ultrapure water (adjusted with 1 M HCl to pH 4.0), which were then poured into a 50 mL teflon-lined stainless steel autoclave. After reaction at 260 ˚C for 2 h, the mixture was cooled to ambient temperature before conducting centrifugation at 3000 g under ambient temperature for 10 min. The pellet was discarded, and the supernatant (c.a. 4 mL) was subjected to dialysis with a dialysis bag (100–500 Da cut-off) against ultrapure water (1 L) for 24 h. Subsequently, the product (mPA CNPs) was collected. We also noticed that no changes in appearance, UV-Vis and FL spectra were observed by simply mixing m-PD (54 mg) and AA (88 mg) at pH 4 for 2 h without heating. As a control, *m*-PD (54 mg) or AA (88 mg) were dissolved in 10 mL of ultrapure water and subjected to the same hydrothermal synthesis and purification procedures. The purified products were then dispersed in ultrapure water before use.

4.2.5 Determination of fluorescence quantum yield and lifetime

Quantum yield (QY) of the mPD C-dots, AA NS and mPA CNPs were determined by a relative measuring method. Quinine sulfate (QY = 0.53 in 0.05 M sulfuric acid, λex = 385 nm) was chosen.

The obtained parameters were mentioned in the following:

$$\phi = \phi' \times \frac{A'}{I'} \times \frac{I}{A} \times \frac{n^2}{n'^2}$$

Where ϕ is the QY of the testing sample, A is the absorbance of the testing sample, I is the integrated fluorescence emission intensity of the testing sample, and n is the refractive index. The prime symbol ($'$) represent to the selected reference. To get the accurate results, the optical density of a series solutions of the testing samples and reference was adjusted to the range of 0–0.1. The fluorescence spectra were measured and the fluorescence areas were integrated. Finally, QY of the testing sample would be determined by the comparison of the integrated fluorescence area *versus* absorbance curves.

The fluorescence decay of mPA CNPs was fitted with a single-exponential decay:

$$I_t = I_0\, exp(\frac{-t}{\tau})$$

Where, I_0 and I_t are the intensity at time zero and certain time. τ is fluorescence life time defined as the time for the intensity drop to 37%. The sample concentration was 1.0 μg/ml. The rate constants (radiative rate, K_r; non-radiative rate, K_{nr}),

doi:10.6342/NTU202300566

fluorescence life time (τ) and quantum yield (ϕ) obey the following equation:

$$\tau = \frac{1}{k_r + k_{nr}}, \qquad \phi = \frac{k_r}{k_r + k_{nr}}$$

The radiative rate and non-radiative rate can be calculated by following equation:

$$\frac{\phi}{\tau} = \frac{k_r}{k_r + k_{nr}} \times (k_r + k_{nr}) = k_r, \qquad \frac{1}{\tau} - k_r = k_{nr}$$

4.2.6 pH sensing based on mPA CNPs

To study the pH responsiveness of mPA CNPs, various mPA CNPs (1 μg mL-1) solu-tions were prepared by mixing mPA CNPs (10 μg mL-1, 50 μL), ultrapure water (400 μL) and phosphate buffer (200 mM, 50 μL) with different pH values (pH 3.0–11.0) for 10 min. Their UV-Vis and fluorescence spectra were then recorded. To investigate the reversibility of pH response of mPA CNPs, the solutions containing 5-fold concentration of mPA CNPs at pH 3.0 were prepared in a similar manner, and then adjusted to various pH values by adding 0.1 M NaOH or HCl. To record the fluorescence microscopic images of mPA CNPs, mPA CNPs (100 μg mL-1, 10 μL) prepared at various pH values were applied separately to microslides and each slide was covered with a glass.

doi:10.6342/NTU202300566

4.2.7 Detection of ROS and anti-oxidants based on mPA CNPs

To determine the sensitivity of the assay for hypochlorite, various solutions were prepared by mixing mPA CNPs (5 μg mL^{-1}, 50 μL), phosphate buffer (200 mM, pH 7.4, 50 μL), and solutions (400 μL) containing different concentrations of sodium hypochlorite. The final concentration of hypochlorite is in the range of 0.125−1.25 μM. After equilibration at 25 °C for 1 h, the solutions were subjected to fluorescence measurement at 500 nm when excited at 400 nm.

Various solutions were separately prepared by mixing mPA CNPs (50 μg mL^{-1}, 50 μL), ultrapure water (350 μL), phosphate buffer (200 mM, pH 7.4, 50 μL) and tested substrates [1 mM of H_2O_2, O_2^-, $^{\cdot}OH$, $NaNO_2$, $(NH_4)_2C_2O_4$, and $NaBH_4$, 50 μL; 100 μM of $ONOO^-$ and NaClO, 50 μL]. After shaking at 160 rpm for 30 min at 25 °C, their fluorescence spectra were recorded under 400 nm excitation.

4.2.8 *In vitro* biocompatibility assessment

The cell viability was evaluated by conducting the Alamar blue assay. Tramp C1 cells seeded at a density of 8000 cells per 96-well plate were incubated overnight in DMEM (200 μL) for cells adhesion. Then, the cells were treated with various concentrations of mPA CNPs (0–20 μg mL^{-1}) for 2 h. The treated cells were then washed

doi:10.6342/NTU202300566

with phosphate buffer saline (PBS) and incubated with refreshed DMEM for 24 h. Next day, the medium was removed and replaced with 100 μL of diluted Alamar Blue agent (diluted 10 times with DMEM) for 2 h. The fluorescence intensity at 595 nm was measured under the excitation at a wavelength of 545 nm.

4.2.9 *In vitro* pH detection

To study the pH response of mPA CNPs in living cells, Tramp C1 cells seeded at a density of 1.0 × 10^5 cells per 24-well plate (with a round-shaped glass inside each well) were incubated overnight in DMEM (500 μL) for cells adhesion. Then, the medium was replaced with PBS of different pH values (pH 5.4, 6.4, 7.4 and 8.4) before adding mPA CNPs solutions (50 μg mL^{-1}, 50 μL). After 2-h incubation, the medium was replaced with PBS (500 μL). The cells were then treated with Hoechst 33342 (5 μg mL^{-1}) for 10 min, followed by multiple washes with PBS. A paraformaldehyde solution (PFA, 500 μL) was added to fix the cells for 15 min. Finally, the PFA solution was removed and the cells were washed with PBS (500 μL). The glass in each well was then taken out, dried, and placed on a microslide containing 10 μL of mounting medium. Fluorescence cell images were captured with the fluorescence microscope (excitation/emission filters: 470-490 nm band pass/520 nm long pass).

For the flow cytometry measurement, the treated cells were washed with PBS and detached from the plate by trypsin (0.25%, 200 μL). The medium (400 μL) were then added to inactivate trypsin. The cell pellet was collected by centrifugation at 500× g for 5 min and subjected to flow cytometry analysis.

4.2.10 *In vitro* hypochlorite detection

Similar to the above method, Tramp C1 cells were seeded at a density of 1.0×10^5 cells per 24-well plate and incubated overnight for cells adhesion. Afterwards, the medium with mPA CNPs solution (5 μg/mL) was replaced for 2-h incubation. The treated cells were then washed with PBS and incubated with PBS in the absence and presence of NaClO (10 μM). Fluorescence images were taken at different time spans from 0 to 30 min. Trypsinization was also performed to collect cells under different treatments, followed by flow cytometry analysis.

4.3 Results and Discussion

4.3.1 Characterization of mPA CNPs

We found that the yield, absorbance, and the fluorescence intensity of mPA CNPs increase upon elevating the hydrothermal temperature from 170 to 260 °C. For example, the fluorescence intensity ratio of mPA CNPs obtained at 170, 200, 230 and

doi:10.6342/NTU202300566

260 °C is 1:2.0:4.4:6.2. We noticed that temperature did not play a significant role in affecting their characteristic features of absorption and fluorescence spectra. For this reason, only the mPA CNPs prepared at 260 °C for 2 h were subjected to further characterization and used to develop sensitive probes. In addition, the products prepared separately from *m*-PD and AA have also been characterized to support the advantages of mPA CNPs over these two products.

The TEM image depicted in Figure 4-1A shows that mPA CNPs have spherical structures, with an average size of 232 ± 53 nm (50 counts). The surfaces of mPA CNPs are rough as shown in the inset of Figure 4-1A. When *m*-PD is the only precursor (Figure 4-2A), *m*-PD CDs with an average size of 7.5 ±1.4 nm and interlayer spacing of 0.31 nm were obtained, corresponding to the (002) plane lattice of graphite.[32] According to the literature, the *m*-PD CDs were formed through processes including oxidation, polymerization, carbonization, and passivation.[33] When AA was used as the precursor, irregular and flake-shaped materials were obtained as shown in Figure 4-2B. The three TEM images suggest that the AA should play a certain role in the formation of large-scale mPA CNPs. It has been reported that a fluorescent material can be produced through the condensation reaction between *m*-PD and AA at ambient condition.[34] The formation of large mPA CNPs may be caused by the subsequent condensation during the heating process. It is also important to highlight that lattice

doi:10.6342/NTU202300566

fringes were only observed in the m-PD CDs sample. This indicates that with the supply of AA, the graphitization of m-PD tends to be retarded, resulting in CNPs consisting of polymer chains with a slight degree of carbonization. In this study, we also found that the molar ratio of m-PD/AA only affects the absorbance and fluorescence intensity. The ratio of fluorescence intensities at 500 nm of the products prepared with the molar ratio of m-PD/AA of 0.5, 1, and 2 is 0.9:1:0.7. Figure 4-1B shows the absorption spectrum of mPA CNPs. There is a sharp peak at 242 nm and a broad band over 320 to 450 nm, which separately correspond to the π-π* transition in benzenoid rings and the higher conjugated polymer chains.[35] The fluorescence spectra of mPA CNPs depicted in Figure 5-1C exhibit both excitation-dependent/independent emission properties, with the strongest PL intensity at 500 nm when excited at the wavelength of 400 nm. The fluorescence QY, lifetime, radiative rate and non-radiative rate are approximately 10%, 7.91 ns, $1.26 \times 10^7\ s^{-1}$ and $1.14 \times 10^8\ s^{-1}$, respectively. These fluorescence properties are fairly close to the fluorescence carbon dot nature.[36] In contrast, m-PD CDs like most CDs show excitation-dependent emission properties as shown in the inset of Figure 4-2C,[11-14] with the strongest emission intensity in the blue region. Figure 4-2C shows a sharp absorption peak at 290 nm and a broadband at 320–350 nm of m-PD CDs, corresponding to the π-π* transition of aromatic C=C bonds and n-π* transition of C=O and C=N bonds at the edge of the carbon lattice, respectively.[37] As compared to the fully carbonized *m*-PD CDs, the bright green emission originated from mPA CNPs could be attributed to the crosstalk of multiple luminescence centers, including molecular-state, crosslink-enhanced-emission-effect-related state, sp^2 subdomains (carbon core state), and surface state.[38] The product obtained from AA only emits weakly at 395 nm when excited at 255 nm, so we will not discuss it hereafter.

The XPS spectra displayed in Figure 4-3 indicate that mPA CNPs and *m*-PD CDs are predominantly composed of carbon, nitrogen, oxygen. The high-resolution C_{1s} spectrum is deconvoluted into five individual component peaks, corresponding to –C–C/–C=C (284.6 eV), –C–N (285.3 eV), –C–O (286.0 eV), –C=O/–C=N (288.1 eV), and –COO (289.0 eV), respectively.[39,40] The signal of C–C/C=C in mPA CNPs is lower, but the sum of C–O, C=O and COO peak intensities is higher than *m*-PD CDs. This result is consistent with our findings shown in Figure 4-1A and Figure 4-2A, indicating that the engagement of AA leads to the successful incorporation of oxygen-containing residues into the polymer chains/carbon hybrid structures. The detection of a stronger –C=O (531.8 eV) signal over –C–O (532.8 eV) in mPA CNPs also confirms that they exhibit a higher oxidation state than *m*-PD CDs due to AA.[41,42] The N_{1s} XPS peaks at 399, 399.9 and 401.1 eV were assigned to pyridinic N, amino N and the sum of graphitic N and protonated amino N, respectively.[43,44] The aliphatic-to-aromatic N ratio signal detected in mPA CNPs is stronger than *m*-PD CDs, indicating that there are

doi:10.6342/NTU202300566

abundant amino groups decorated on the surface/polymer chains.

For the FT-IR spectra of mPA CNPs and *m*-PD CDs depicted in Figure 4-4, the peaks observed at 3408 and 3313 cm^{-1}, the broad band around 3212 cm^{-1}, and the peak at 3035 cm^{-1} were attributed to the stretching vibrations of N–H, O–H, and aromatic C–H, respectively.[45] The intense signal centered at around 1632 cm^{-1} conveyed signals from quinoid imine stretching, –C=C– ring stretching and $-NH_2$ bending, and the peaks registered at 1500 and 1334 cm^{-1} were separately assigned to the C=C and C–N stretching vibrations of benzenoid amine.[46,47] The characteristic peak of C=O stretching at 1701 cm^{-1} indicates the introduction of AA residues in mPA CNPs.[48] The spectral features of mPA CNPs are comparatively more apparent than those of *m*-PD CDs, further confirming the greater retention of pyrolytic *m*-PD/AA polymers.

4.3.2 pH sensing based on mPA CNPs

As illustrated in Figure 4-5A, the PL intensity of mPA CNPs (1.0 $\mu g\ mL^{-1}$) at 500 nm decreases upon increasing pH values from 3.0 to 11.0. The UV-Vis spectra displayed in the inset of Figure 4-5A also show blue shifts of the peaks from 260 to 240 nm and 400 to 350 nm upon increasing the pH value. Figure 4-5B shows that the fluorescence intensity of mPA CNPs exhibit a linear response to pH over the range of 5.5 to 8.5 ($R^2 = 0.989$), revealing their potential for pH sensing of biological samples. It is expected

doi:10.6342/NTU202300566

that the pH responsiveness of mPA CNPs is resulted from the protonation/deprotonation of the amino and carboxyl groups, respectively.[49,50] As depicted in Table 4-1, the zeta potential of mPA CNPs becomes less positive as pH increases, which supports our hypothesis. Meanwhile, mPA CNPs undergo aggregation, as demonstrated in the fluorescence microscopic images in Figure 4-5C and the corresponding hydrodynamic sizes detected by dynamic light scattering were 352 ± 15, 803 ± 104, and 1157 ± 224 nm, at pH values of 3.0, 7.0, and 11.0, respectively. Due to the aggregation behaviour, non-radiative energy transfer such as photoinduced electron transfer (PET) can readily occur through the close proximity of neighboring amine groups.[51,52] The fluorescence lifetimes of mPA CNPs were investigated and the average values at pH 3.0 (8.19 ns), 7.0 (7.91 ns) and 11.0 (7.02 ns) were obtained from the fluorescence decay curves in Figure 4-6. The reduced lifetime indicates that the mPA CNPs undergoes an ultra-fast electron transfer process when excited at higher pH values. This combined dynamic and static quenching mechanism based on the fluorescence quenching of mPA CNPs can be adopted to develop high-efficiency pH sensors. We further investigated the reversibility of the pH response of mPA CNPs by alternately changing the pH value of the solution from 3.0 to 11.0 in three consecutive cycles (3.0-11.0-3.0). The results shown in Figure 4-5D demonstrates that the fluorescence intensity of mPA CNPs is reversible under cycling various pH. In addition, the inset photograph also shows that

doi:10.6342/NTU202300566

the color of the solution becomes lightter but cloudy under alkaline conditions.

Encouraged by the results mentioned above, mPA CNPs were applied for intracellular pH monitoring. As displayed in Figure 5-7, the fluorescence intensity of mPA CNPs in Tramp C1 cells progressively decreased with the pH increasing from 5.4 to 8.4. The average intensity of fluorescent from each event was further quantified using the flow cytometry (Figure 4-8), and the fluorescence of mPA CNPs is pH-dependent in living cells, corresponding to that in the fluorescence spectra (Figure 4-5A and B). Compared with other CDs previously reported (Table 4-2)[16,39,49,50,53-55], mPA CNPs are effective for cell staining as satisfactory and reliable cell images can be achieved with a relatively reduced dose (5 μg mL^{-1} for 2 h). It should also be noted that mPA CNPs exhibit eligible biocompatibility. It can be found that under the same cultivation conditions, more than 80 % of cells survived as the dose of mPA CNPs is less than 20 μg mL^{-1} (Figure 4-9). Taken together, mPA CNPs are competent for intracellular pH sensing.

4.3.3 Hypochlorite sensing based on mPA CNPs

Hypochlorite can induce the fluorescence quenching of mPA CNPs (0.5 μg mL^{-1}) at 500 nm, and the intensity exhibits a linear relationship (R^2 = 0.985) with the concentration in the range of 0.125–1.25 μM in phosphate buffer at pH 7.4 (Figure 5-

10A). The limit of detection (LOD) was estimated to be 0.029 μM based on the signal-to-noise ratio of 3. Table 4-3 shows that mPA CNPs provides comparable sensitivity to hypochlorite when compared to the other reported methods based on CDs.[24-27,29,31,56] It is well accepted that the surface functional groups such as aromatic amines possess a high tendency to oxidize when hypochlorite is introduced.[28,31] In this sensing process, static fluorescence quenching occurs due to the generation of less or non-fluorescent ground state complexes. In view of this, the FT-IR spectra of mPA CNPs versus hypochlorite was explored. As depicted in Figure 4-11, the characteristic absorption peaks at 3200 and 1334 cm^{-1} corresponding to N–H and C–N stretching vibrations were reduced, while the peak at 1632 cm^{-1} increased due to the appearance of more quinoid imine after the introduction of hypochlorite. The selectivity of mPA CNPs (5 μg mL^{-1}) toward hypochlorite (NaClO) over common ROS (H_2O_2, O_2^-, $ONOO^-$, $^{\cdot}OH$) and various antioxidants [$NaNO_2$, $(NH_4)_2C_2O_4$, and $NaBH_4$] was further investigated. Figure 4-10B shows that hypochlorite (10 μM) caused significant fluorescence quenching of mPA CNPs, while the effects of other substances (100 μM) were almost negligible. Only a slight fluorescence quenching of mPA CNPs was found in the presence of OH radical (100 μM). From Table 4-4, it can be observed that the one electron redox potential of NaClO (1.49 eV) is the highest except for OH radical (2.33 eV)[57-59]. In addition, the negatively charged nature of hypochlorite also makes them readily accessible to the mPA CNPs surface via electrostatic interactions, resulting in a superior propensity for oxidation. The performance of mPA CNPs on hypochlorite detection was further compared with DCFH-DA, which is a commercial dye commonly used to detect various ROS. As Figure 4-10C displayed, mPA CNP provides a more selective response to hypochlorite than DCFH-DA. These findings confirm the promising bioapplicability of mPA CNP in the detection of hypochlorite in living cells.

Subsequently, mPA CNPs was employed as a fluorescent probe for specific detection of hypochlorite in Tramp C1 cells. As shown in Figure 4-12, cells emit green fluorescence when they were stained with 5 μg mL^{-1} of mPA CNPs for 2 h. After the introduction of NaClO (10 μM), the fluorescence intensity decreased gradually and demonstrates an effective diminish after 30 min. In addition, the fluorescence intensity of mPA CNPs after 30 min of stimulus was also detected by flow cytometry (Figure 4-13). The bar graph shows that the fluorescence of mPA CNPs was reduced by approximately 25% after hypochlorite treatment. On the contrary, after co-treatment with *N*-acetylcysteine (NAC, 10 mM), an ROS scavenger, no fluorescence quenching of mPA CNPs was detected since the hypochlorite-mediated oxidation was inhibited. Therefore, mPA CNPs developed herein can be regarded as a potential probe for real-time detecting hypochlorite changes in cells stimulated by different pharmaceuticals.

doi:10.6342/NTU202300566

4.4 Conclusions

In the study, we developed a novel type of fluorescent probe, mPA CNPs with pH sensing and hypochlorite detection capabilities. Through a one-pot hydrothermal process using two different carbon sources, green emission fluorescent CNPs with a quantum yield of 10% were generated. Due to the existence of effective functional groups, the as-prepared mPA CNPs exhibited favorably responsiveness toward pH and hypochlorite. In response to higher pH values, the fluorescence of mPA CNPs decreased through a combination of static and dynamic quenching mechanisms due to the deprotonation of amino groups. In addition, hypochlorite with high oxidation potential for aromatic amines was capable of reducing the PL of mPA CNPs based on static quenching. The mPA CNPs have been successfully applied to cell imaging owing to their high efficiency of cell uptake and good biocompatibility. With the pH-sensitive response in the range of 5.5–8.5 and high selectively to hypochlorite among other interfering analytes, mPA CNPs further demonstrated their promising potential for fluorescence sensing of pH values and hypochlorite in Tramp C1 living cells.

doi:10.6342/NTU202300566

4.5 References

[1] A.I. Arieff, A. Kerian, S.G. Massry, J. DeLima, Intracellular pH of brain: alterations in acute respiratory acidosis and alkalosis. Am. J. Physiol. 230 (1976) 804–812.

[2] H. Tapper, R. Sundler, Role of lysosomal and cytosolic pH in the regulation of macrophage lysosomal enzyme secretion. Biochem. J. 272 (1990) 407–414.

[3] E. Persi, M. Duran-Frigola, M. Damaghi, W.R. Roush, P. Aloy, J.L. Cleveland, R.J. Gillies, E. Ruppin, Systems analysis of intracellular pH vulnerabilities for cancer therapy. Nat. Commun. 9 (2018) 2997.

[4] Y. Kato, S. Ozawa, C. Miyamoto, Y. Maehata, A. Suzuki, T. Maeda, Y. Baba, Acidic extracellular microenvironment and cancer. Cancer Cell Int. 13 (2013) 89.

[5] F. Weinberg, N. Ramnath, D. Nagrath, Reactive oxygen species in the tumor microenvironment: an overview. Cancers (Basel). 11 (2019) 1191.

[6] P. Chen, Z. Zheng, Y. Zhu, Y. Dong, F. Wang, G. Liang, Bioluminescent turn-on probe for sensing hypochlorite in vitro and in tumors. Anal. Chem. 89 (2017) 5693–5696.

[7] C. Nusshold, M. Kolllroser, H. Kofeler, G. Rechberger, H. Reicher, A. Ullen, E. Bernhart, S. Waltl, I. Kratzer, A. Hermetter, H. Hackl, Z. Trajanoski, A. Hrzenjak, E. Malle, W. Sattler, Hypochlorite modification of sphingomyelin

doi:10.6342/NTU202300566

generates chlorinated lipid species that induce apoptosis and proteome alterations in dopaminergic PC12 neurons in vitro. Free Radic. Biol. Med. 48 (2010) 1588–1600.

[8] J.T. Hou, W.X. Ren, K. Li, J. Seo, A. Sharma, X.Q. Yu, J.S. Kim, Fluorescent bioimaging of pH: from design to applications. Chem. Soc. Rev. 46 (2017) 2076–2090.

[9] Y.-N. Chen, P.-C. Chen, C.-W. Wang, Y.-S. Lin, C.-M. Ou, L.-C. Ho, H.-T. Chang, One-pot synthesis of fluorescent BSA–Ce/Au nanoclusters as ratiometric pH probes. Chem. Commun.50 (2014) 8571–8574.

[10] P. Chen, I. Ilyas, S. He, Y. Xing, Z. Jin, C. Huang, Ratiometric pH sensing and imaging in living cells with dual-emission semiconductor polymer dots. Molecules 24 (2019) 2923.

[11] H.-W. Chu, B. Unnikrishnan, A. Anand, Y.-W. Lin, C.-C. Huang, Carbon quantum dots for the detection of antibiotics and pesticides. J. Food Drug Anal. 28 (2020) 539–557.

[12] A. Han, S. Hao, Y. Yang, X. Li, X. Luo, G. Fang, J. Liu, S. Wang, Perspective on recent developments of nanomaterial based fluorescent sensors: applications in safety and quality control of food and beverages. J. Food Drug Anal. 28 (2020) 486–507.

[13] D. Xu, Q. Lin, H.-T. Chang, Recent advances and sensing applications of carbon dots. Small Methods 4 (2020) 1900387.

[14] H. Ehtesabi, Z. Hallaji, S. Najafi Nobar, Z. Bagheri, , Carbon dots with pH-responsive fluorescence: a review on synthesis and cell biological applications. Microchim. Acta 287 (2020) 150.

[15] W. Song, W. Duan, Y. Liu, Z. Ye, Y. Chen, H. Chen, S. Qi, J. Wu, D. Liu, L. Xiao, C. Ren, X. Chen, Ratiometric detection of intracellular lysine and pH with one-pot synthesized dual emissive carbon dots. Anal. Chem. 89 (2017) 13626–13633.

[16] X. Ye, Y. Xiang, Q. Wang, Z. Li, Z. Liu, A red emissive two-photon fluorescence probe based on carbon dots for intracellular pH detection. Small 15 (2019) 1901673.

[17] M. Zhang, R. Su, J. Zhong, L. Fei, W. Cai, Q. Guan, W. Li, N. Li, Y. Chen, L. Cai, Q. Xu, Red/orange dual-emissive carbon dots for pH sensing and cell imaging. Nano Res. 12 (2019) 815–821.

[18] D. Li, Y. Feng, J. Lin, M. Chen, S. Wang, X. Wang, H. Sheng, Z. Shao, M. Zhu, X. Meng, A mitochondria-targeted two-photon fluorescent probe for highly selective and rapid detection of hypochlorite and its bio-imaging in living cells. Sens. Actuators B Chem. 222 (2016) 483–491.

[19] M. Vedamalai, D. Kedaria, R. Vasita, I. Gupta, Oxidation of phenothiazine based fluorescent probe for hypochlorite and its application to live cell imaging. Sens. Actuators B Chem. 263 (2018) 137–142.

[20] Y. Feng, S. Li, D. Li, Q. Wang, P. Ning, M. Chen, X. Tian, X. Wang, Rational design of a diaminomaleonitrile-based mitochondria – targeted two-photon fluorescent probe for hypochlorite in vivo: solvent-independent and high selectivity over Cu^{2+}. Sens. Actuators B Chem. 254 (2018) 282–290.

[21] X. Zhong, Q. Yang, Y. Chen, Y. Jiang, Z. Dai, Aggregation-induced fluorescence probe for hypochlorite imaging in mitochondria of living cells and zebrafish. J. Mater. Chem. B 8 (2020) 7375–7381.

[22] G. Chen, F. Song, J. Wang, S. Sun, J. Fan, X. Qiang, X. Wang, B. Dou, X. Peng, FRET spectral unmixing: a ratiometric fluorescent nanoprobe for hypochlorite. Chem. Commun. 48 (2012) 2949–2951.

[23] B. Yin, J. Deng, X. Peng, Q. Long, J. Zhao, Q. Lu, Q. Chen, H. Li, H. Tang, Y. Zhang, S. Yao, Green synthesis of carbon dots with down- and up-conversion fluorescent properties for sensitive detection of hypochlorite with a dual-readout assay. Analyst 138 (2013) 6551–6557.

doi:10.6342/NTU202300566

[24] Y. Hu, J. Yang, L. Jia, J.-S. Yu, Ethanol in aqueous hydrogen peroxide solution: Hydrothermal synthesis of highly photoluminescent carbon dots as multifunctional nanosensors. Carbon 93 (2015) 999–1007.

[25] E.F.C. Simoes, L.P. Silva, J.C.G.E. Silva, J.M.M. Leitao, Hypochlorite fluorescence sensing by phenylboronic acid-alizarin adduct based carbon dots. Talanta 208 (2020) 120447.

[26] H. Wang, L. Zhang, X. Guo, W. Dong, R. Wang, S. Shuang, X. Gong, C. Dong, Comparative study of Cl,N-Cdots and N-Cdots and application for trinitrophenol and ClO− sensor and cell-imaging. Anal. Chim. Acta 1091 (2019) 76–87.

[27] L. Wang, J. Jana, J.S. Chung, S.H. Hur, High quantum yield aminophenylboronic acid-functionalized N-doped carbon dots for highly selective hypochlorite ion detection. Spectrochim. Acta A Mol. Biomol. Spectrosc. 260 (2021) 119895.

[28] L. Ma, S. Sun, Y. Wang, K. Jiang, J. Zhu, J. Li, H. Lin, A graphene quantum dot-based fluorescent nanoprobe for hypochlorite detection in water and in living cells. Microchim. Acta 184 (2017) 3833–3840.

[29] Y. Meng, H. Zhang, W. Li, Y. Liu, X. Gong, S. Shuang, C. Dong, A facile synthesis of long-wavelength emission nitrogen-doped carbon dots for intracellular pH variation and hypochlorite sensing. Biomater. Sci. 9 (2021) 2255–2261.

doi:10.6342/NTU202300566

[30] F. Yan, Z. Bai, T. Ma. X. Sun, F. Zu, Y. Luo, L. Chen, Surface modification of carbon quantum dots by fluorescein derivative for dual-emission ratiometric fluorescent hypochlorite biosensing and in vivo bioimaging. Sens. Actuators B Chem. 296 (2019) 126638.

[31] Y. Jiao, Y. Meng, W. Lu, Y. Gao, Y. Liu, X. Gong, Y. Liu, S. Shuang, C. Dong, Design of long-wavelength emission carbon dots for hypochlorous detection and cellular imaging. Talanta 219 (2020) 121170.

[32] S.A. Hill, D. Benito-Alifonso, S.A. Davis, D.J. Morgan, M. Berry, M.C. Galan, Practical three-minute synthesis of acid-coated fluorescent carbon dots with tuneable core structure. Sci. Rep. 8 (2018) 12234.

[33] C.-I. Wang, W.-C. Wu, A. P. Periasamy, H.-T. Chang, Electrochemical synthesis of photoluminescent carbon nanodots from glycine for highly sensitive detection of hemoglobin. Green Chem. 16 (2014) 2509–2514.

[34] X. Wu, Y. Diao, C. Sun, J. Yang, Y. Wang, S. Sun, Fluorimetric determination of ascorbic acid with o-phenylenediamine. Talanta 59 (2003) 95–99.

[35] J. Stejskal, Polymers of phenylenediamines. Prog. Polym. Sci. (2015) 41, 1–31.

[36] Z.X. Liu, Z.L. Wu, M.X. Gao, H. Liu, C.Z. Huang, Carbon dots with aggregation induced emission enhancement for visual permittivity detection. Chem. Commun. 52 (2016) 2063–2066.

doi:10.6342/NTU202300566

[37] A. Sharma, T. Gadly, S.S. Neogy, K. Ghosh, M. Kumbhakar, Molecular origin and self-assembly of fluorescent carbon nanodots in polar solvents. J. Phys. Chem. Lett. 8 (2017) 1044–1052.

[38] Q. Zeng, T. Feng, S. Tao, S. Zhu, B.Yang, Precursor-dependent structural diversity in luminescent carbonized polymer dots (CPDs): the nomenclature. Light Sci. Appl. 10 (2021) 1–13.

[39] Y.X. Jiao, G.H. Han, Y. Gao, W. Lu, Y. Liu, M. Xian, S. Shuang, C. Dong, Facile synthesis of orange fluorescence carbon dots with excitation independent emission for pH sensing and cellular imaging. Anal. Chim. Acta 1042 (2018) 125–132.

[40] A.M. Craciun, A. Diac, M. Focsan, C. Socaci, K. Magyari, D. Maniu, I. Mihalache, L. M. Veca, S. Astilean, A. Terec, Surface passivation of carbon nanoparticles with p-phenylenediamine towards photoluminescent carbon dots. RSC Adv. 6 (2016) 56944–56951.

[41] M. Vedamalai, A.P. Periasamy, C.-W. Wang, Y.-T. Tseng, L.-C. Ho, C.-C. Shih, H.-T. Chang, Carbon nanodots prepared from o-phenylenediamine for sensing of Cu^{2+} ions in cells. Nanoscale 6 (2014) 13119–13125.

doi:10.6342/NTU202300566

[42] A. Dutta, S.T.Y. Trolles-Cavalcante, A. Cleetus, V. Marks, A. Schechter, R. D. Webster, A.Borenstein, Surface modifications of carbon nanodots reveal the chemical source of their bright fluorescence. Nanoscale Adv. 3 (2021) 716–724.

[43] O.L. Li, S. Chiba, Y. Wada, G. Panomsuwan, T. Ishizaki, Synthesis of graphitic-N and amino-N in nitrogen-doped carbon via a solution plasma process and exploration of their synergic effect for advanced oxygen reduction reaction. J. Mater. Chem. A 5 (2017) 2073–2082.

[44] T. Pillar-Little, D.Y. Kim, Differentiating the impact of nitrogen chemical states on optical properties of nitrogen-doped graphene quantum dots. RSC Adv. 7 (2017) 48263–48267.

[45] R. Gupta, S. Sanotra, H.N. Sheikh, B.L. Kalsotra, Room temperature aqueous phase synthesis and characterization of novel nano-sized coordination polymers composed of copper (II), nickel (II), and zinc (II) metal ions with p-phenylenediamine (PPD) as the bridging ligand. J. Nanostructure Chem. 3 (2013) 1–9

[46] L. Zhang, H. Wang, W. Yu, Z. Su, L. Chai, J. Li, Y. Shi, Facile and large-scale synthesis of functional poly (m-phenylenediamine) nanoparticles by Cu^{2+}-assisted method with superior ability for dye adsorption. J. Mater. Chem. A 22 (2012 18244–18251.

doi:10.6342/NTU202300566

[47] F. Limosani, E. M. Bauer, D. Cecchetti, S. Biagioni, V. Orlando, R. Pizzoferrato, P. Prosposito, M. Carbone, Top-down N-doped carbon quantum dots for multiple purposes: heavy metal detection and intracellular fluorescence. Nanomaterials 11 (2021) 2249.

[48] K.I. Takei, R. Takahashi, T. Noguchi, Correlation between the hydrogen-bond structures and the C=O stretching frequencies of carboxylic acids as studied by density functional theory calculations: Theoretical basis for interpretation of infrared bands of carboxylic groups in proteins. J. Phys. Chem. B 112 (2008) 6725–6731.

[49] S. Li, X. Song, Y. Wang, Z. Hu, F. Yan, G. Feng, Developed a ratiometric fluorescence pH nanosensor based on label-free carbon dots for intracellular lysosome imaging and water pH monitoring with a smartphone. Dyes Pigm. 193 (2021) 109490.

[50] S. Song, J. Hu, M. Li, X. Gong, C. Dong, S. Shuang, Fe^{3+} and intracellular pH determination based on orange fluorescence carbon dots co-doped with boron, nitrogen and sulfur. Mater. Sci. Eng. C 118 (2021) 111478

[51] T. Ghosh, S. Chatterjee, E. Prasad, Photoinduced electron transfer from various aniline derivatives to graphene quantum dots. J. Phys. Chem. A 119 (2015) 11783–11790.

[52] D. Escudero, Revising intramolecular photoinduced electron transfer (PET) from first-principles. Acc. Chem. Res. 49 (2016) 1816–1824.

[53] S. Zhang, X. Ji, J. Liu, Q. Wang, L. Jin, One-step synthesis of yellow-emissive carbon dots with a large Stokes shift and their application in fluorimetric imaging of intracellular pH. Spectrochim. Acta A Mol. Biomol. Spectrosc. 227 (2020) 117677.

[54] Q. Wang, H. Yang, Q. Zhang, H. Ge, S. Zhang, Z. Wang, X. Ji, Strong acid-assisted preparation of green-emissive carbon dots for fluorometric imaging of pH variation in living cells. Mikrochim Acta 186 (2019) 1–9.

[55] J. Shangguan, D. He, X. He, K. Wang, F. Xu, J. Liu, J. Tang, X. Yang, J. uang, Label-free carbon-dots-based ratiometric fluorescence pH nanoprobes for intracellular pH sensing. Anal. Chem. 88 (2016) 7837–7843.

[56] Z. Wei, H. Li, S. Liu, W. Wang, H. Chen, L. Xiao, C. Ren, X. Chen, Carbon dots as fluorescent/colorimetric probes for real-time detection of hypochlorite and ascorbic acid in cells and body fluid. Anal. chem. 91 (2019) 15477–15483.

[57] S. Losada-Barreiro, C. Bravo-Diaz, Free radicals and polyphenols: The redox chemistry of neurodegenerative diseases. Eur. J. Med. Chem. 133 (2017) 379–402.

doi:10.6342/NTU202300566

[58] P. Nguema, M. jun, Application of ferrate (VI) as disinfectant in drinking water treatment processes: a review. Int. J. Microbiol. Res. 7 (2016) 53–62.

[59] R.M.G. Berg, K. Møller, D. M.Bailey, Neuro-oxidative-nitrosative stress in sepsis. J. Cereb. Blood Flow Metab. 31 (2011) 1532–1544.

doi:10.6342/NTU202300566

Table 4-1. Zeta potentials of mPA CNPs (1 μg mL^{-1}) at various pH values.

pH	Zeta potential (mV)
3.0	16.3 ± 1.3
5.0	11.7 ± 1.8
7.0	6.5 ± 0.6
9.0	-2.1 ± 1.5
11.0	-4.7 ± 1.4

doi:10.6342/NTU202300566

Table 4-2. **Comparison of the in vitro fluorescence behavior of mPA CNPs with other CD-based pH sensors.**

Materials	Precursors	Linear pH range	Dosage (μg mL^{-1})	Labeling time (h)	Reference
pH-CDs	*p*-phenylenediamine, *o*-phenylenediamine and dopamine	3.5–6.5	20	0.5	16
N-CDs	*p*-phenylenediamine	2.6–4.6; 5.0–6.8	600	0.5	38
CDs	anthranilic acid and o-phenylenediamine	3.0–8.0[a]	400	4	48
BNSCDs	4-carboxyphenylboronic acid and 2,5-diaminobenzenesulfonic acid	1.6–7.0	500	0.5	49
Y-CDs	*o*-phenylenediamine	4.0–8.2	40	4	52
G-CDs	***m***-phenylenediamine	6–10	40	5	53
CDs	citric acid and basic	5.2–8.8	500	2	54

	fuchsin				
mPA CNPs	***m***-phenylenediamine and ascorbic acid	5.5–8.5	5	2	This work

[a] non-linear

Table 4-3. Comparison of the fluorescence behavior of mPA CNPs with other CD-based hypochlorite sensors.

Materials	Precursors	Linear range (μM)	LOD (nM)	Reference
CDs	ethanol and H_2O_2	0.1–10	80	24
CDs	3-aminophenylboronic acid and alizarin red S	0–200	4470	25
Cl,N-CDs	dried shaddock peel and concentrated HCl	3.24–216	2880	26
GAAP-CDs	glutaric acid and 3-aminophenylboronic acid	0.1–100	500	27
N-CDs	neutral red and glutamine	1.5–112.5; 112.5–187.5	270	29
N, P-CDs	safranine T and phosphoric acid	0.74–5.93; 5.93–25.93	46.1	31
RD-CDs	2,5-diaminobenzenesulfonic acid	0.1–100	83	55
mPA CNPs	***m***-phenylenediamine and	0.125–1.25	29	This work

doi:10.6342/NTU202300566

ascorbic acid

Table 4-4. **One electron redox potential of ROS and antioxidants**.

Redox couple	$\mathbf{\mathit{E}^0/V}$
$^{\cdot}OH, H^+/ H_2O$	2.33
$OCl^-, 2H^+/ Cl^-, H_2O$	1.49
$ONOO^-, 2H^+/ NO_2^{\cdot}, H_2O$	1.4
$O_2^{\cdot}, 2H^+/ H_2O_2$	0.94
$H_2O_2, H^+/ {}^{\cdot}OH, H_2O$	0.38
$NO_2^-, H_2O/ NO, 2OH^-$	-0.46
$C_2O_4^{2-}/ 2CO_2$	-0.59
$BH_4^-, 8OH^-/ H_2BO_3, 5H_2O$	-1.24

doi:10.6342/NTU202300566

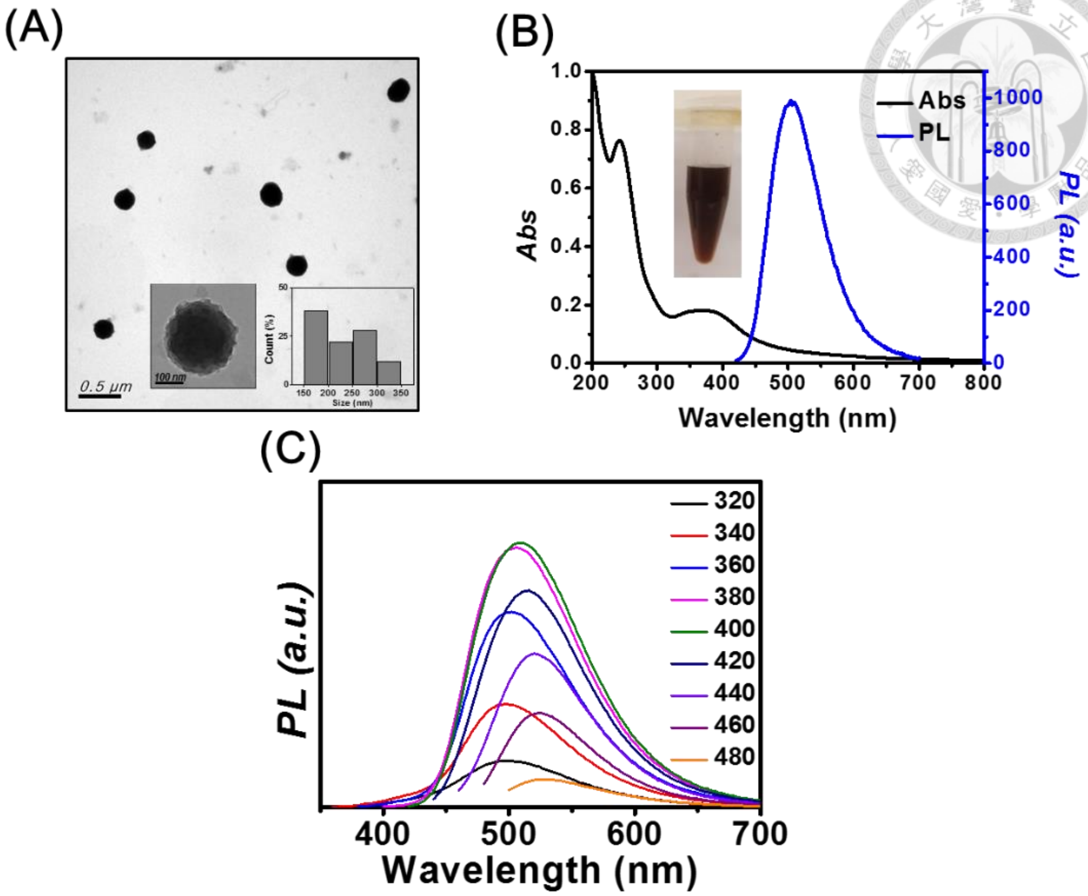

Figure 4-1. (A) TEM image of mPA CNPs. Inset: high resolution TEM image and size distribution analysis. (B) UV-Vis absorption and fluorescence spectra of *m*-PD CDs excited at 400 nm. Inset: photograph of 1 mg mL^{-1} mPA CNPs solution. (C) Fluorescence spectra of mPA CNPs in aqueous solution as a function of excitation wavelength from 320 nm to 480 nm.

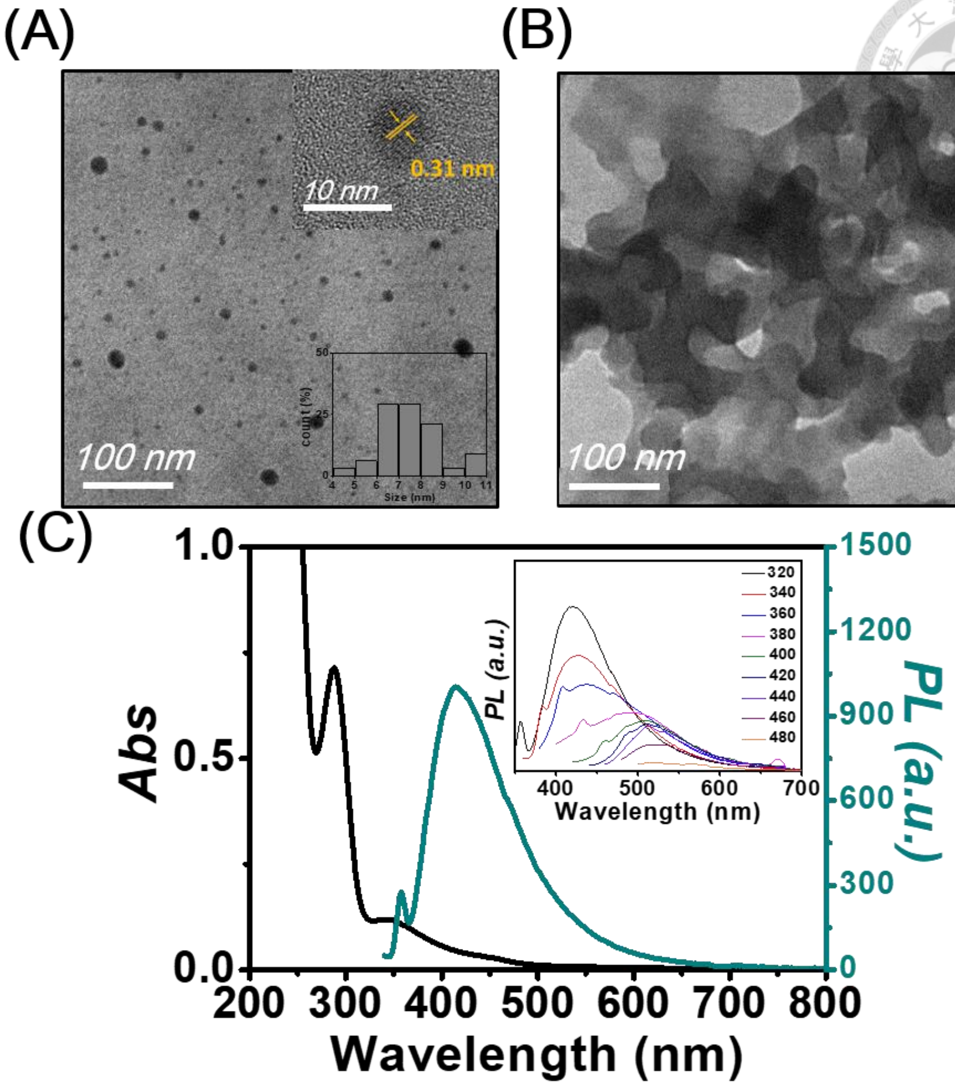

Figure 4-2. TEM images of (A) *m*-PD CDs (insets: high-resolution TEM image and size distribution analysis) and (B) AA nanoparticulates. (C) UV-Vis absorption and fluorescence spectra of *m*-PD CDs. Inset: fluorescence spectra of *m*-PD CDs in aqueous solution as a function of excitation wavelength.

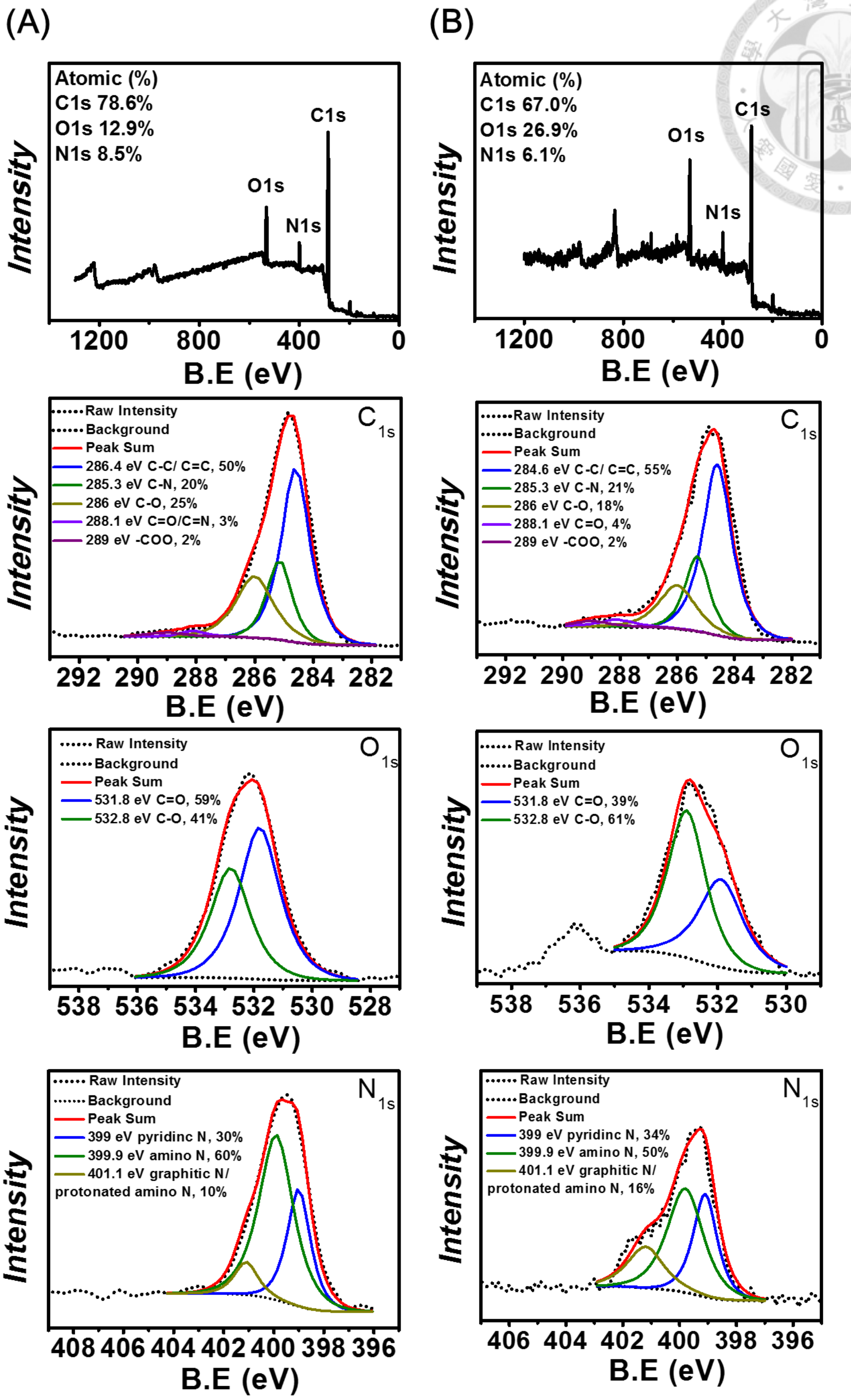

Figure 4-3. XPS survey spectra and high-resolution XPS scan spectra over C_{1s}, O_{1s} and N_{1s} of (A) mPA CNPs and (B) *m*-PD CDs.

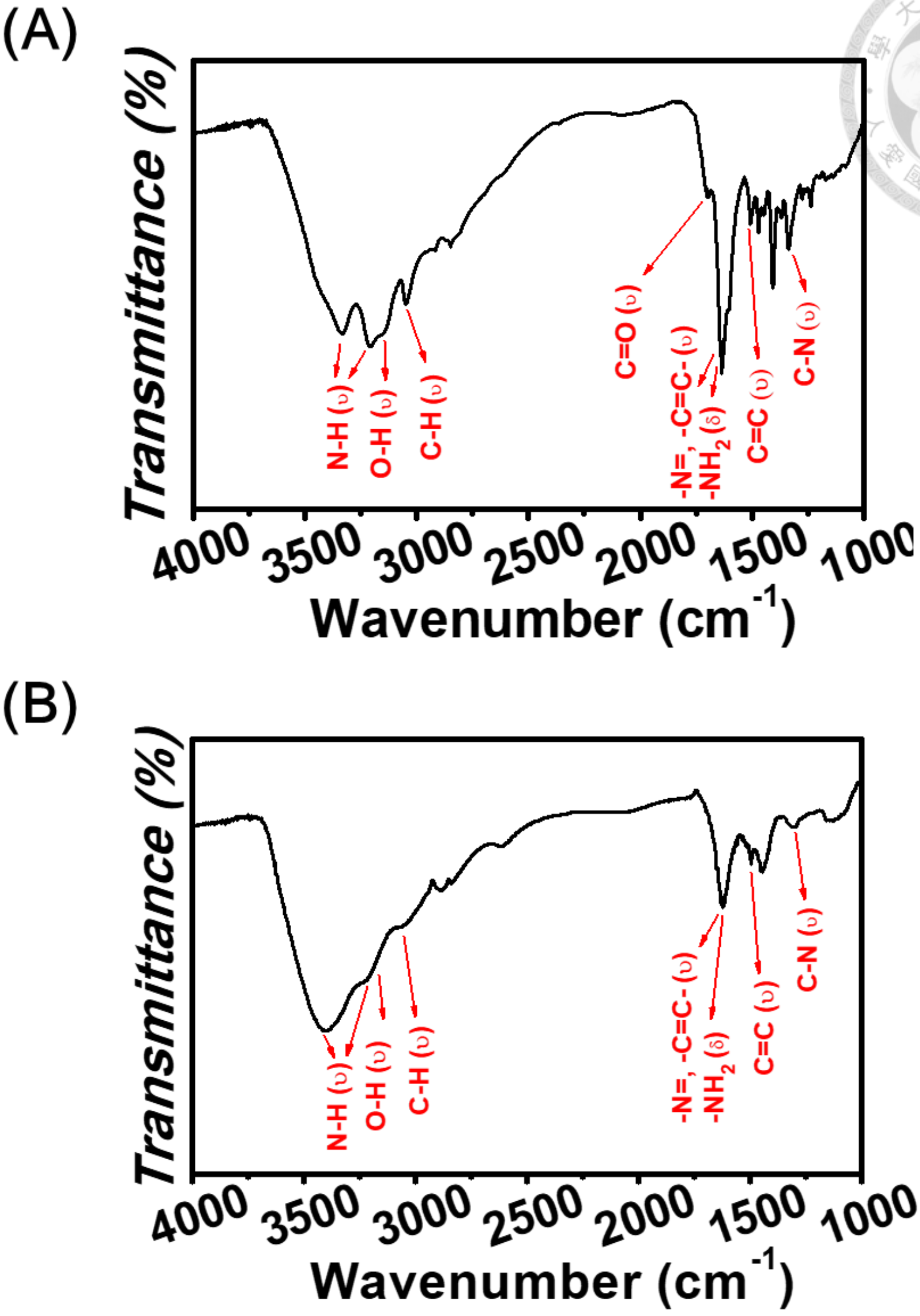

Figure 4-4. FT-IR spectra of (A) mPA CNPs and (B) *m*-PD CDs (ν: stretching, δ: bending).

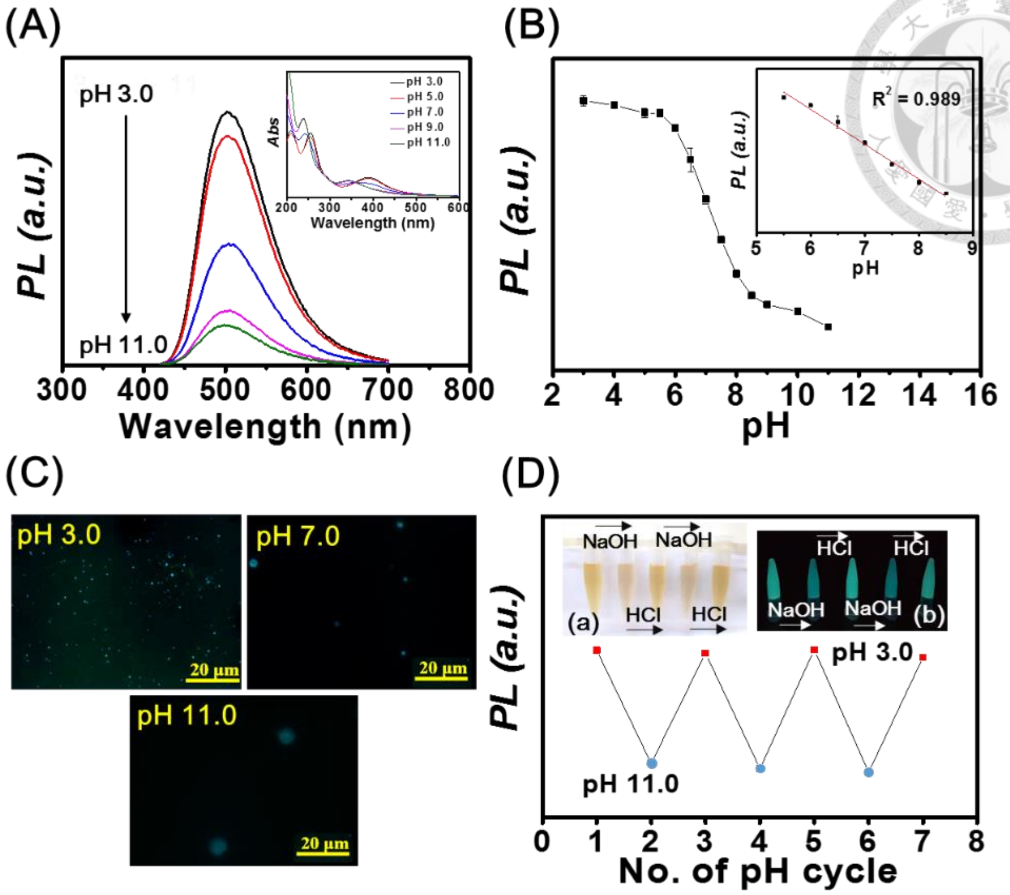

Figure 4-5. (A) Fluorescence spectra of mPA CNPs (1 μg mL^{-1}) at pH values of 3.0, 5.0, 7.0, 9.0, and 11.0. Inset: Corresponding UV-Vis spectra of mPA CNPs (1 μg mL^{-1}). (B) Plot of the fluorescence intensity at 500 nm versus pH values. (C) Fluorescence microscopic images of mPA CNPs at pH 3.0, 7.0 and 11.0. (D) The fluorescence intensity of mPA CNPs at 500 nm cycled between pH 3.0 and 11. 0. Inset: Corresponding photographs under (a) white light and (b) UV light. The pH of the mPA CNPs solution is switched back and forth between 3.0 and 11.0 by using 0.1 M HCl or NaOH solutions, respectively. Excitation and emission wavelengths are 400 and 500 nm, respectively.

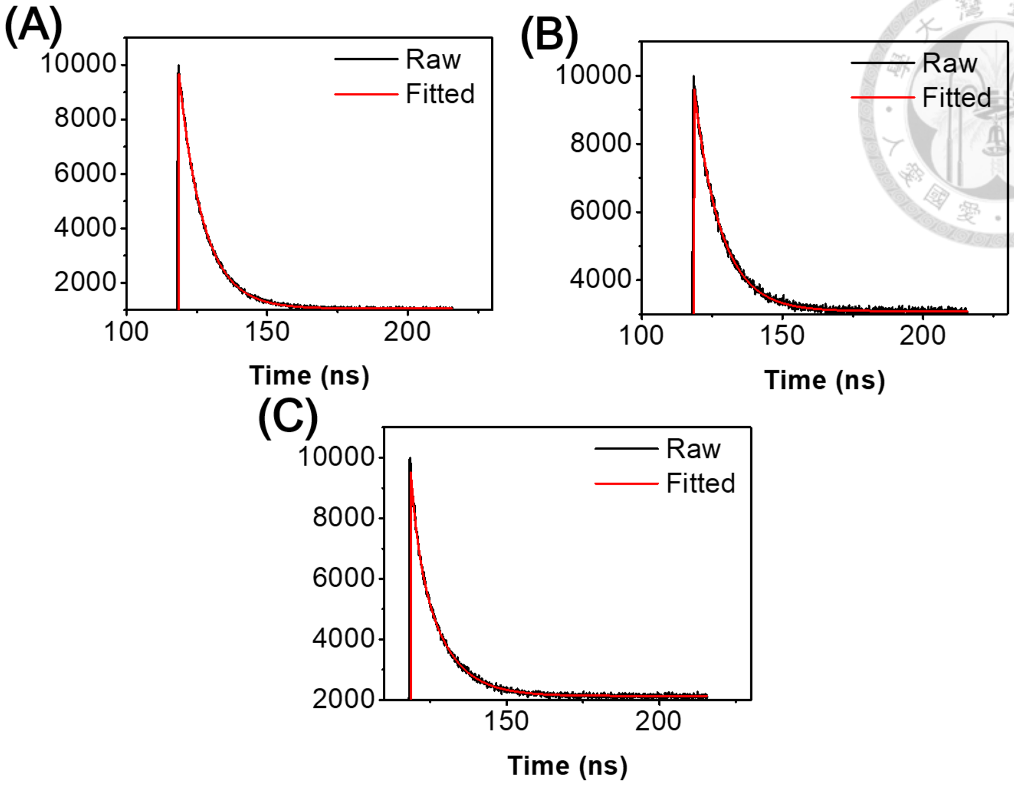

Figure 4-6. Fluorescence decay curves of mPA CNPs (1.0 µg mL^{-1}) at pH (A) 3.0, (B) 7.0 and, (C) 11.0 upon excitation using a 365-nm pulsed laser.

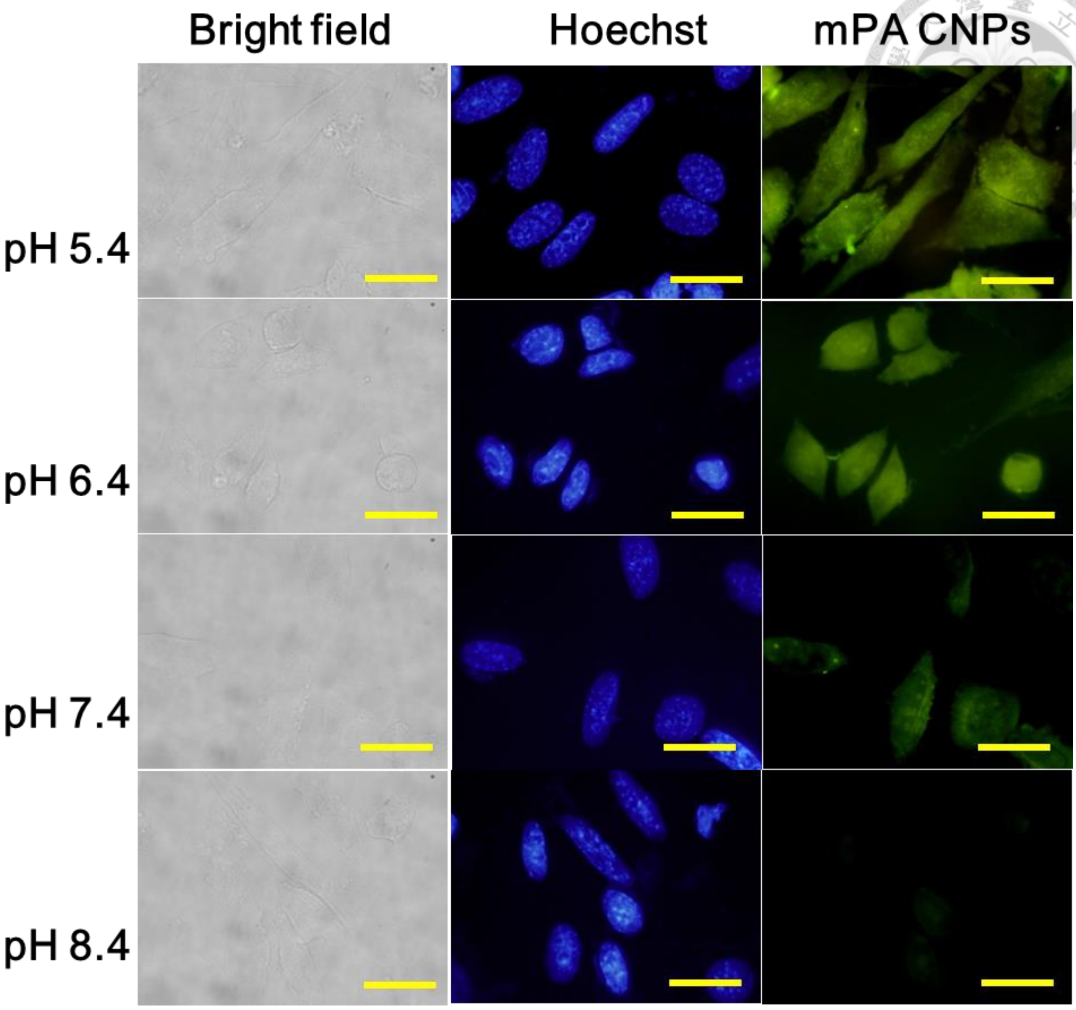

Figure 4-7. Fluorescence microscopic images of Tramp C1 cells stained with mPA CNPs (5 μg mL^{-1}) were exposed to various PBS solutions at pH 5.4, 6.4, 7.4, and 8.4 for 2 h**.** From left to right were different channels: bright field, blue channel (λ_{ex} = 350–380 nm, λ_{em} = 420 nm) and green channel (λ_{ex} = 470–490 nm, λ_{em} = 520 nm). The scale bar denotes 20 μm.

doi:10.6342/NTU202300566

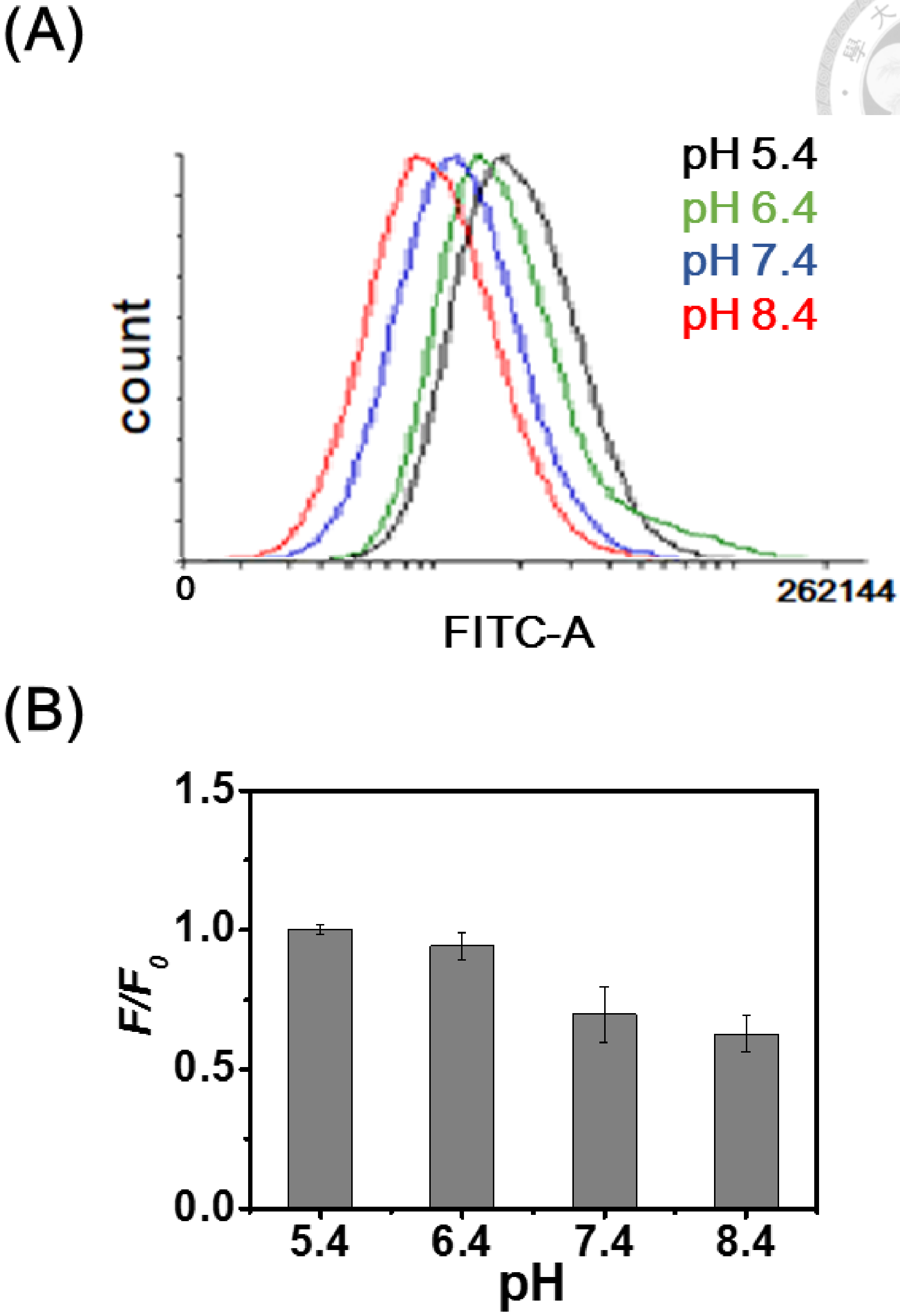

Figure 4-8. Flow cytometry analysis of Tramp C1 cells treated with mPA CNPs (5 μg mL^{-1}) at various pH values for 2 h. (A) A histogram (number of events versus FITC channel signal) and (B) The bar graph representing the relative fluorescence intensity (F/F_0) versus the pH value. F_0 and F denote the mean fluorescence intensities of mPA

CNPs in Tramp C1 cells at pH 5.4 and other specific pH values, respectively.

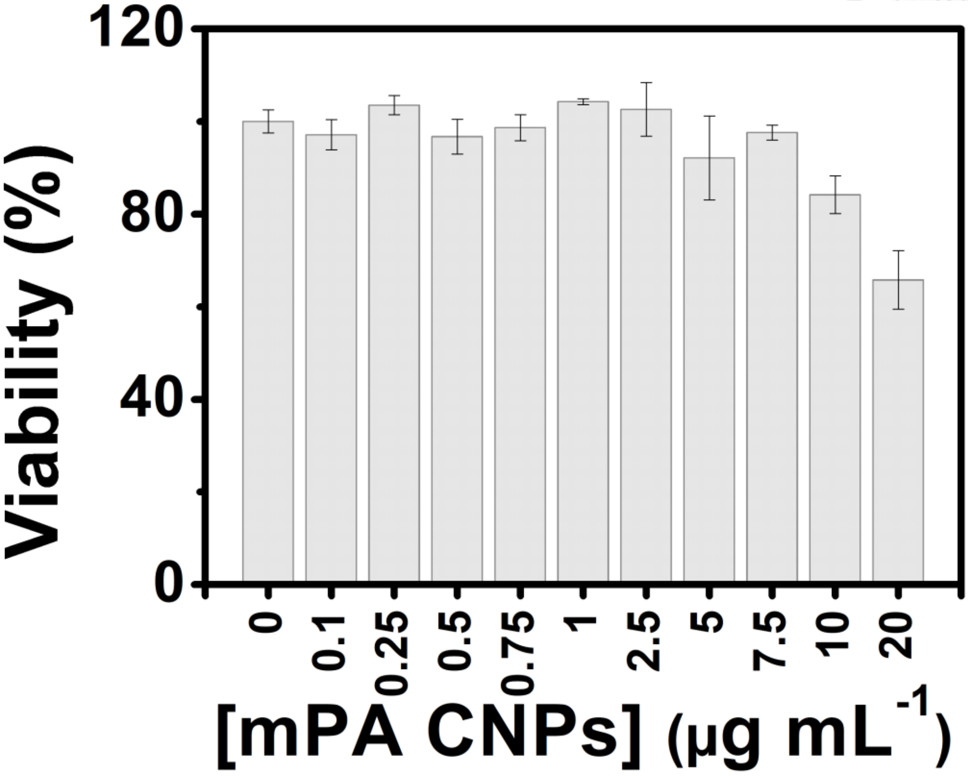

Figure 4-9. Cell viability for Tramp C1 cells in the presence of a series of concentrations of mPA CNPs.

doi:10.6342/NTU202300566

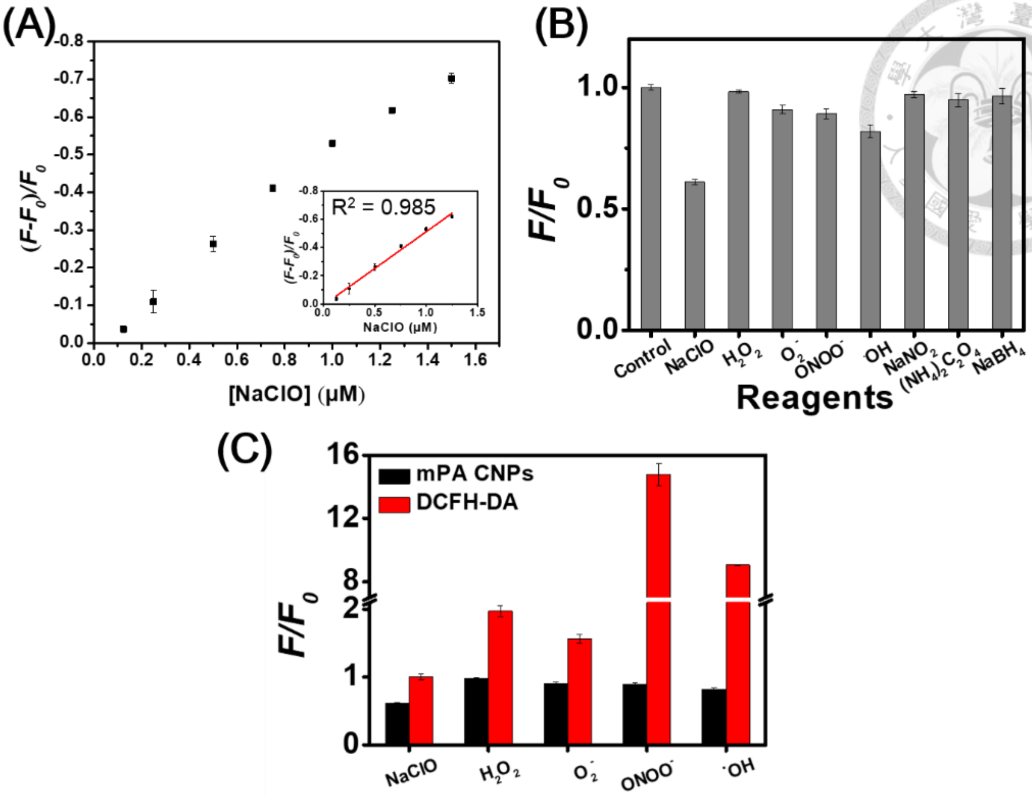

Figure 4-10. (A) Plot of the fluorescence reduction of mPA CNPs versus hypochlorite concentration. The linear relationship between $(F - F_0)/F_0$ and NaClO concentration ranges from 0.125 to 1.5 μM. F_0 and F denote the fluorescence intensities of mPA CNPs at 500 nm in the absence and presence of hypochlorite. Excitation wavelength is 400 nm. (B) Effects of potential interferences on fluorescence intensities of mPA CNPs (5 μg mL^{-1}) at 500 nm in 20 mM phosphate buffer (pH 7.4). The concentrations of NaClO and ONOO$^-$ are both 10 μM and the concentrations of H_2O_2, O_2^-, $^\cdot$OH, $NaNO_2$, $(NH_4)_2C_2O_4$, and $NaBH_4$ are all 100 μM. (C) Fluorescence intensity changes of mPA CNPs (5 μg/ mL) or DCFH-DA (25 μM) in 20 mM phosphate buffer (pH 7.4) toward various ROS and ONOO$^-$. F_0 and F denote separately the fluorescence intensities of

respective probe in the absence and presence of different analytes. DCF fluorescence is detected by using excitation and emission wavelengths of 485 and 535 nm, respectively.

doi:10.6342/NTU202300566

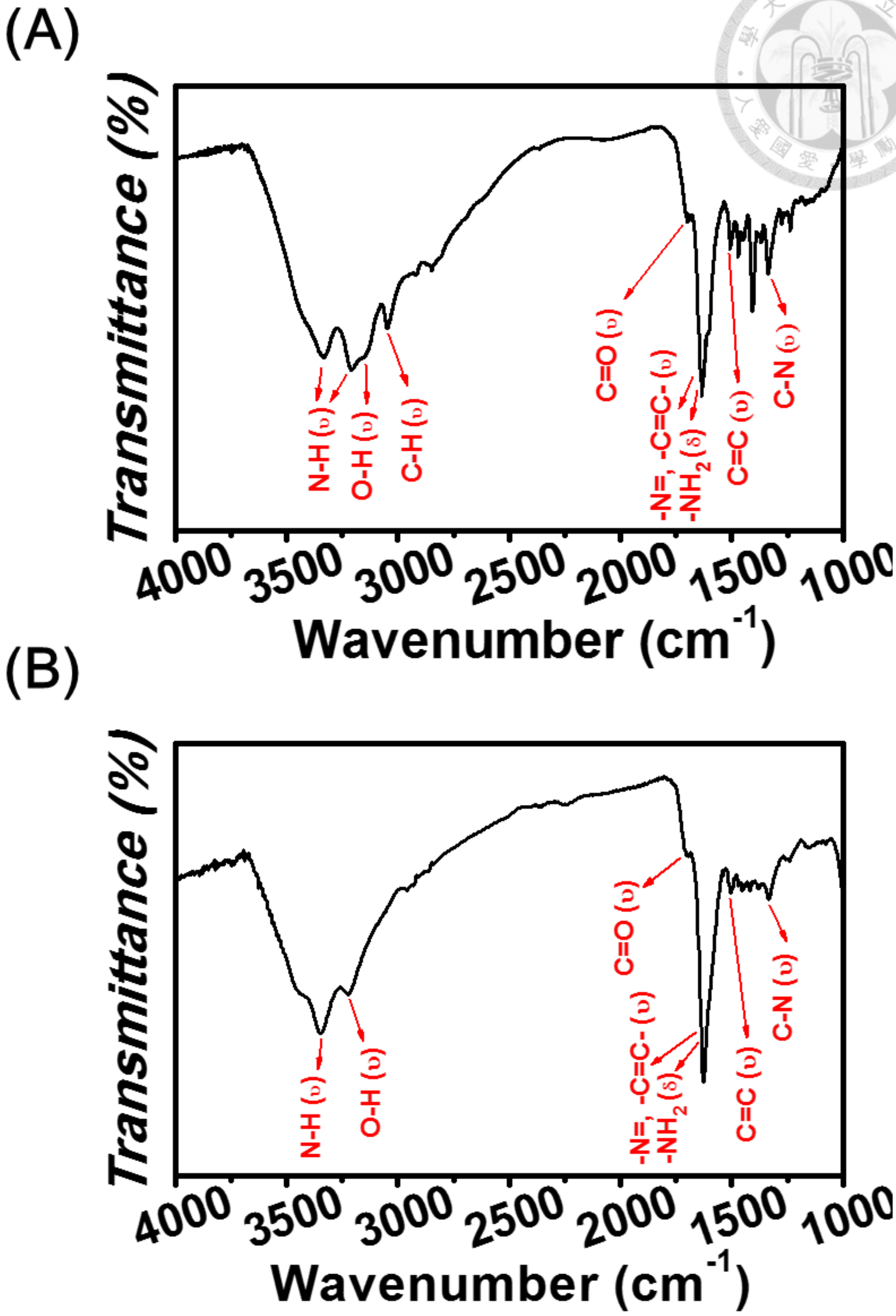

Figure 4-11. FT-IR spectra of mPA CNPs in the (A) absence and (B) presence of NaClO (100 μM).

doi:10.6342/NTU202300566

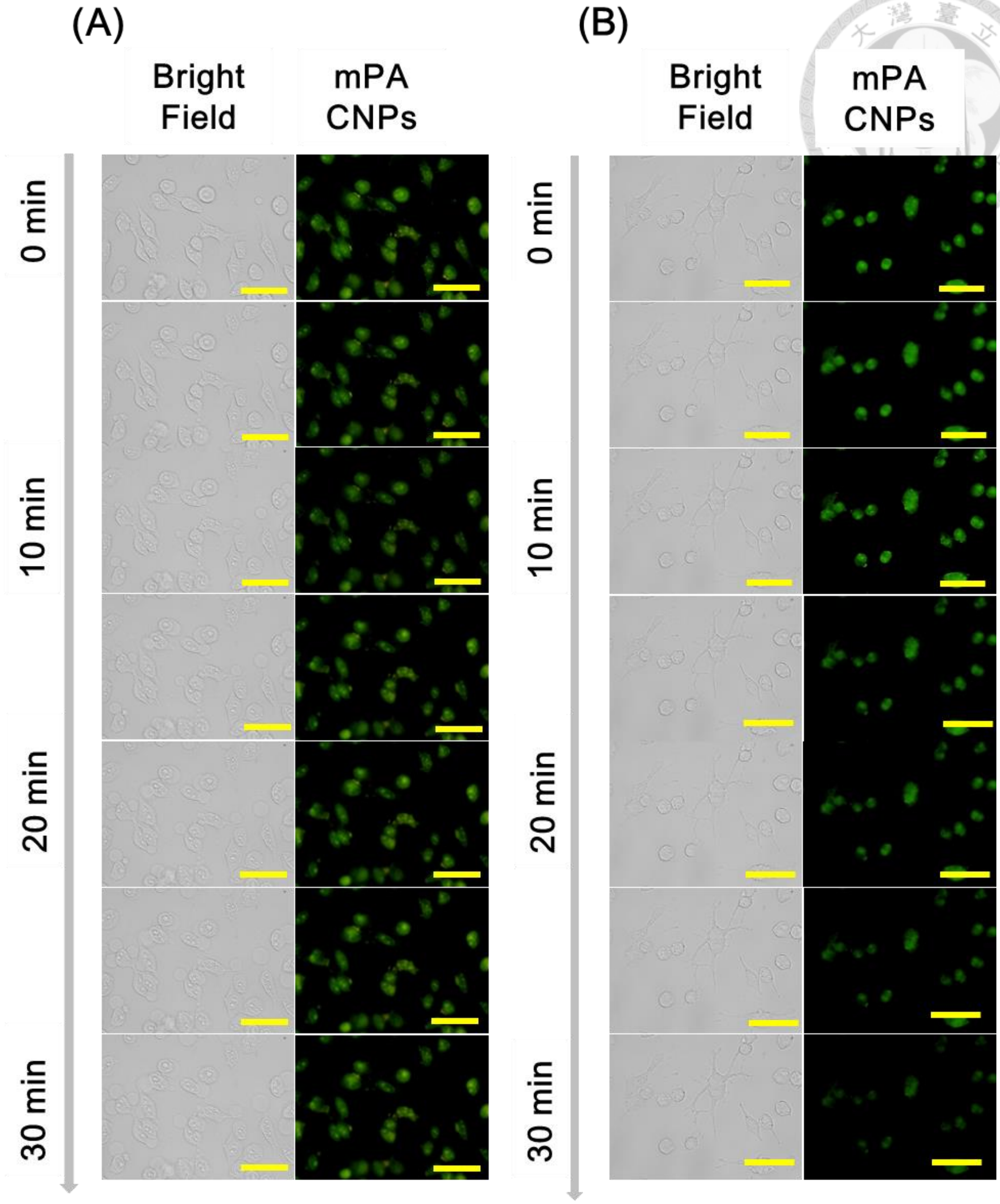

Figure 4-12. Fluorescence microscopic images of Tramp C1 cells incubated with mPA CNPs (5 μg mL^{-1}) in DMEM medium (pH 7.4) for 2 h. Afterwards, the stained cells were stimulated with PBS in (A) the absence of and (B) the presence of 10 μM NaClO. Fluorescence images were collected at different time spans from 0 to 30 min. From left to right are different channels: bright field and green channel (λ_{ex} = 470–490 nm, λ_{em} =

doi:10.6342/NTU202300566

520 nm). The scale bar denotes 32 μm.

doi:10.6342/NTU202300566

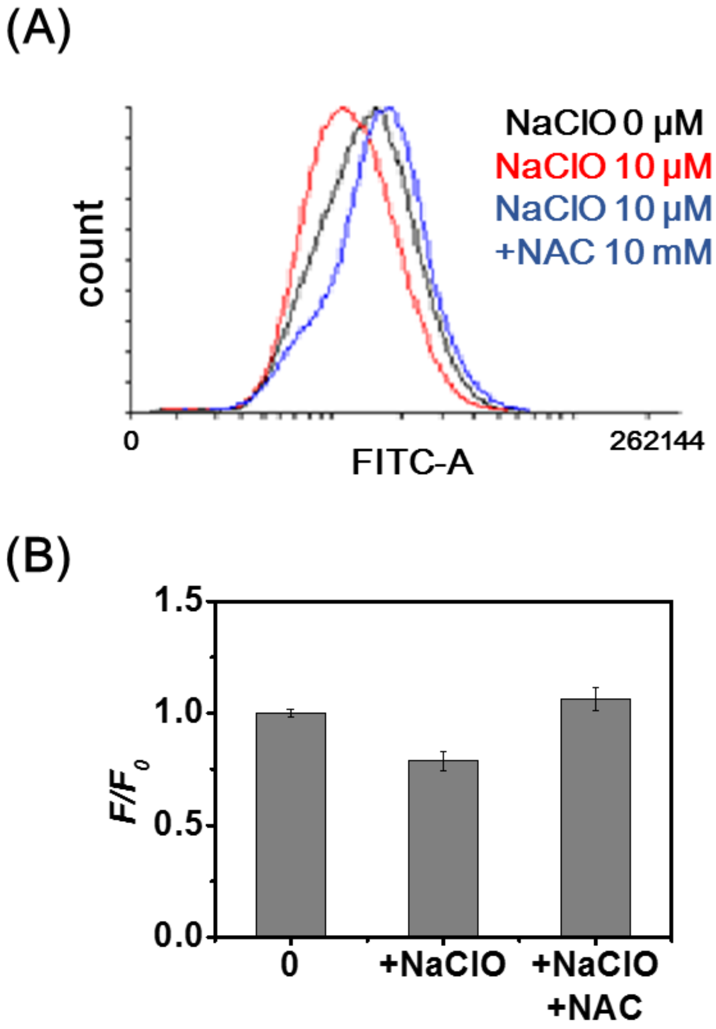

Figure 4-13. Flow cytometry analysis of Tramp C1 cells stained with mPA CNPs (5 μg mL^{-1}) incubated with NaClO (10 μM) or NaClO/NAC (10 μM and 10 mM, respectively) for 30 min. (A) A histogram (number of events versus FITC channel signal) and (B) The bar graph representing the relative fluorescence intensity (F/F_0) versus different treatments. F_0 and F denote the mean fluorescence intensities of mPA CNPs in Tramp C1 cells in the absence and presence of hypochlorite.

doi:10.6342/NTU202300566

Chapter 5　Polymer/glutathione Au nanoclusters for detection of sulfides

The content in this chapter has been published to: Y.-S. Lin, L.-W. Chuang, B.-Y. Wu, Y.-H. Lin, H.-T. Chang, Polymer/glutathione Au nanoclusters for detection of sulfides. Sens. actuators. B Chem. 333 (2021) 129356

doi:10.6342/NTU202300566

5.1 Introduction

Gold nanoclusters (Au NCs) with sizes smaller than 3 nm emit light in the visible to near-infrared (NIR) region when excited by UV light, but they do not show strong absorption in the visible region as found for larger-sized gold nanoparticles [1-3]. A ligand-to-metal charge transfer (LMCT) mixed with a ligand-to-metal–metal charge transfer (LMMCT) has been suggested for the fluorescence properties of Au NCs, meaning that their fluorescence is dependent on the core and surface properties [4]. More specifically, the emission wavelength and quantum yield for Au NCs are related to their sizes, structures, oxidation states, and surface ligands [5]. Owing to their ease in preparation, biocompatibility, long lifetime, and large Stokes shift, Au NCs have been widely used in sensing of important analytes and cell imaging [6, 7]. Most Au NC based sensing and imaging systems take advantage of analyte-induced fluorescence quenching. To provide higher sensitivity and reproducibility for quantitation of important analytes such as glucose, thrombin, trypsin, H_2O_2, NO_2^-, H_2S, Hg^{2+}, Pb^{2+}, Cu^{2+} in biological and environmental samples, template (surface ligand) species and concentration, temperature, pH, and ionic strength must be optimized [8-13].

A variety of approaches have been demonstrated for the synthesis of Au NCs in aqueous solution. Many thiol compounds such as cysteine, glutathione (GSH), para-mercaptobenzoic acid (p-MBA), 11-mercaptoundecanonic acid, lipoic acid,

doi:10.6342/NTU202300566

phenylethylthiolate have been commonly used for the preparation of Au NCs, mainly because of their reducing ability and strong bonding with gold under alkaline conditions [14-19]. In addition, these compounds act as protecting agents to control the size of the Au NCs and minimize their aggregation [20]. The surface thiol ligands possess different electronic structures, and, thus, also affect the absorption and photoluminescence properties of Au NCs [21-23]. Interestingly, the emission wavelength and quantum yield of Au NCs can be tuned by using two different small thiol compounds such as glutathione and cysteine as reducing and capping agents, mainly through controlling thier oxidation states, surface properties, and structures [24-26]. A ligand-induced etching approach using thiol compounds such as 11-mercaptoundecanonic acid has been applied to the preparation of Au NCs from Au nanoparticles under alkaline conditions [27]. At pH > 9.0, the thiol compounds oxidize the surface Au atoms and then form Au-thiol complexes to stabilize the Au NCs. One feature of this approach is that the size and optical properties of the Au NCs can be easily tuned by selecting various thiol compounds. However, the as-prepared Au NCs are unstable against high concentration of salt (e.g., >10 mM NaCl) and photoirradiation.

Ligand-exchange approaches using polymers such as poly(N-isopropylacrylamide-acrylicacid-2-hydroxyethylacrylate) and poly(amidoamine) (PAMAM) as templates are useful for the preparation of polymer-capped Au NCs from thiol-capped Au nanoparticles [28-30]. However, such preparation processes are tedious and slow and are usually problematic. Alternatively, Au NCs have been prepared from Au^{3+} using proteins such as bovine serum albumin (BSA) as templates under alkaline conditions [31]. At pH > 12.0, proteins with tyrosine residues provide strong reduction strength to reduce Au^{3+} ions to form Au NCs. In addition, the proteins protect as-formed Au NCs to minimize their contact with quenchers such as oxygen and salt. However, use of a large quantity of proteins is required. To minimize the amount of proteins use, a thiol-assisted approach has been employed for the preparation of Au NCs in the presence of proteins [32]. For example, GSH was used to reduce Au^{3+} to Au^{+} ions, which are further reduced to form Au atoms by proteins such as BSA and transferrin. It is important to point out that the protein-protected Au NCs are much more stable against salt and photoirradiation over small thiol-capped Au NCs.

Herein, a thiol-assisted approach using GSH in the presence of polydiallyldimethylammonium (PDDA) or polystyrene sulfonate (PSS) was applied to the preparation of Au NCs from Au^{3+}. We investigated several important factors such as the charge and concentration of polymers, reaction time, as well as pH on the formation of Au NCs, and, thus, their optical properties and stability. Our study found that PDDA over PSS is more suitable for the preparation of Au NCs. The as-prepared PDDA/GSH-Au NCs were found to be sensitive and selective for quantitation of sulfide.

doi:10.6342/NTU202300566

Practicality of this simple, rapid, sensitive, and selective assay was validated by the quantitation of sulfide ions in samples of spring water.

5.2 Experimental Section

5.2.1 Materials

Hydrogen tetrachloroaurate(III) trihydrate ($HAuCl_4$) was obtained from Alfa Aesar (Heysham, England). Glutathione (GSH), PDDA (molecular weight 100,000–200,000), potassium chromate, PSS (molecular weight 70,000), sodium salts of acetate, bromide, carbonate, chloride, fluoride, iodide, nitrate, phosphate, sulfate, sulfide, and thiosulfate were obtained from Sigma-Aldrich (St. Louis, MO, USA). Monobasic, dibasic, and tribasic sodium salts of phosphate, phosphoric acid, as well as sodium hydroxide were obtained from J.T. Baker (New Jersey, USA). Ultrapure water (18.2 MΩ cm) from a Milli-Q system (Millipore, Billerica, MA, USA) was used in all experiments.

5.2.2 Synthesis of PDDA/GSH-Au NCs

Stock solutions of PDDA (10 wt%) and GSH (30 mM) were simply prepared in ultrapure water. Various amounts of PDDA (final concentrations, 0.1−1 wt%), GSH

doi:10.6342/NTU202300566

(final concentrations, 2−4 mM), and $HAuCl_4$ (final concentration, 2 mM) were used to prepare PDDA/GSH-Au NCs. One example of the mixture used for the preparation of PDDA/GSH-Au NCs was prepared by mixing PDDA (1 wt%, 100 μL), GSH (30 mM, 100 μL), and ultrapure water (685.5 μL) at 25 ℃ to form a PDDA-GSH mixture. $HAuCl_4$ (20 mM, 100 μL) was then added to the mixture, which was then subjected to vigorous stirring for 10 min. Next, the mixture was pre-heated at 70°C for 5 min prior to adjustment of the solution pH to a value of 11.0 by adding 1 M NaOH, with a final mixture volume of 1.0 mL. The reaction was carried out at 70°C for 6 h. Similar procedures, besides a reaction time of 24 h, were applied for the preparation of PDDA/GSH-Au NCs at various pH values, including 2.0, 5.0, and 8.0. The final pH values were adjusted via the addition of 1.0 M HCl or NaOH. The PDDA/GSH-Au NCs were stored in the dark at 4°C and their concentrations are denoted as 1X for simplicity. A 35 kDa cut-off dialysis bag was used to purify the as-prepared PDDA/GSH-Au NCs (2 mL) against 2 L of ultrapure water for 6 h prior to further characterization.

5.2.3 Synthesis of PSS/GSH-Au NCs

Stock solutions of PSS (10 wt%) and GSH (30 mM) were simply prepared in ultrapure water. Various amounts of PSS (final concentrations, 0.1−1 wt%), GSH (final concentrations, 2−4 mM), and $HAuCl_4$ (final concentration, 2 mM) were used to

doi:10.6342/NTU202300566

prepare PSS/GSH-Au NCs under similar conditions to that used for the preparation of PDDA/GSH-Au NCs. The PSS/GSH-Au NCs were stored in the dark at 4°C and their concentration are denoted as 1X for simplicity. A 35 kDa cut-off dialysis bag was used to purify the as-prepared PSS/GSH-Au NCs (2 mL) against 2 L of ultrapure water for 6 h prior to characterization.

5.2.4 Synthesis of GSH-Au NCs

Freshly prepared aqueous solutions of $HAuCl_4$ (20 mM, 100 μL) and GSH (30 mM, 100 μL) were mixed with ultrapure water at 25°C. Aliquots of 1 M HCl or NaOH were added separately to the mixtures to separately adjust their pH values to 2.0, 5.0, 8.0 and 11.0. The mixtures were reacted at 70°C for 24 h. The as-formed GSH-Au NCs were stored in the dark at 4°C and their concentrations are denoted as 1X for simplicity. A 35 kDa cut-off dialysis bag was used to purify the as-prepared GSH-Au NCs (2 mL) against 2 L of ultrapure water for 6 h before being subjected to characterization.

5.2.5 Characterization

The fluorescence emission spectra for as-prepared PDDA/GSH-Au NCs, PSS/GSH-Au NCs, and GSH-Au NCs were recorded with a Synergy 4 microplate

doi:10.6342/NTU202300566

reader (BioTek, Winooski, VT, USA) with an excitation wavelength of 365 nm. The fluorescence lifetimes were recorded using a time-resolved absorption and emission spectrometer (NS010; Pascher Instrument, Sweden) using a diode laser emitting at 350 nm as the light source. A μ-Quant microplate UV-Vis spectrophotometer (BioTek, Winooski, VT, USA) was employed to record the absorption spectra. The Fourier transform infrared (FT-IR) spectra of PDDA, GSH-Au NCs, and PDDA/GSH-Au NCs were recorded using a Varian 640 FTIR spectrophotometer (Palo Alto, CA, USA). Transmission electron microscopy (TEM) images of the Au NCs were taken by using a JSM-1200EX II microscope (JEOL, Tokyo, Japan). The zeta potentials for the Au NCs were measured using a dynamic light scattering analyzer (DLS) from Nano ZS (Malvern, Worcestershire, UK). Prior to X-ray photoelectron spectroscopy (XPS) measurements, the Au NC samples were drop cast onto Si substrates and the solvents allowed to evaporate at ambient temperature (25°C) and pressure. X-ray photoelectron spectroscopy (XPS) measurements were conducted using an ESCA Model: PHI 5000 VersaProbe from VG Scientific (West Sussex, UK). The binding energies were corrected with the C 1s peak at 284.6 eV as a standard.

5.2.6 Detection of sulfides

Phosphate buffer (PB, 200 mM, pH 10.0, 20 μL) and PDDA/GSH-Au NCs (1X,

doi:10.6342/NTU202300566

20 μL) prepared at pH 11.0 in the presence of 0.1% PDDA were added to aqueous solutions containing Na_2S (0-200 μM). The mixtures (final volume, 400 μL) were equilibrated for 30 min at 25°C in the dark prior to fluorescence measurements.

5.2.7 Analysis of real sample

Two bottles (120 mL) of spring water were collected from a local hot spring hotel in Beitou, Taipei, Taiwan. Zinc acetate (1 M, 50 μL) was added into one of the two bottles. Both samples were adjusted to pH 10.0 immediately after collection, and then stored at 4°C. The sample containing zinc acetate was used for the quantitation of sulfide ions by applying a methylene blue method approved by the American Public Health Association (APHA) [33]. For quantitation of sulfide ions using PDDA/GSH-Au NCs, aliquots (40 μL) of the sample were spiked separately with various concentrations of Na_2S (40 μL), with final concentrations of 0-10 μM. Phosphate buffer (200 mM, pH 10.0, 20 μL), PDDA/GSH-Au NCs (1X, 20 μL), spiked water sample (40 μL), and ultrapure water (320 μL) were mixed together and reacted at 25°C for 30 min. Then, each of the mixtures (final volume 400 μL) was centrifuged (9000 g, 5 min) and the supernatant taken out for the fluorescence measurements.

5.3 Results and discussion

5.3.1 Preparation of PDDA/GSH-Au NCs

In accordance with the literature [32], the reaction temperature in this study was set at 70°C for a fast reaction. The concentration of Au^{3+} mainly affects the amount of Au NCs produced but not their optical properties; its concentration was kept constant (2 mM). However, the concentrations of PDDA as a template and GSH as a reducing agent are prominent in determining the formation of PDDA/GSH-Au NCs. It is important to note that a GSH/Au^{3+} molar ratio of 1.5 allows for the preparation of GSH-Au NCs with high fluorescence [34]. At molar ratios higher than 1.5, precipitation and formation of larger Au nanoparticles are problematic. We investigated the effects of PDDA concentration, reaction time, and pH on the formation of PDDA/GSH-Au NCs from Au^{3+} (2 mM) and GSH (3 mM). Figure 5-1 shows the fluorescence spectra measured for PDDA/GSH-Au NCs prepared separately at pH values of 2.0, 5.0, 8.0 and 11.0. Figure 5-2 shows the TEM images of PDDA/GSH-Au NCs synthesized at aforementioned pH values. At pH 5.0 and pH 8.0, the fluorescence intensities are weak and the PDDA/GSH-Au NCs are unstable. At these two pH values, PDDA is positively charged and GSH is negatively charged. The strong electrostatic interaction leads to the precipitation of the PDDA/GSH Au NCs, as shown in Figure 5-2. Relatively, the

doi:10.6342/NTU202300566

fluorescence intensities for the PDDA/GSH Au NCs prepared at pH 2.0 and pH 11.0 are stronger. It is interesting to note that the fluorescence spectral profiles for these NCs are quite different. The emission wavelengths for PDDA/GSH-Au NCs prepared at pH 2.0 and pH 11.0 are located at 620 nm and 690 nm, respectively, when excited at 365 nm. At pH 2.0, GSH and PDDA are both positive charges, and thus only GSH-Au NCs are existent, revealing that the fluorescence peak at 620 nm is assigned for GSH-Au NCs. On the other hand, at pH 11.0, GSH is negative, GSH-Au NCs are further stabilized by the neutral and hydrophilic PDDA through hydrogen bonding. As a result, PDDA/GSH-Au NCs are formed. Through hydrogen bonding of PDDA molecules, the PDDA/GSH-Au NCs got closer, leading to the appearance of a new peak at 690 nm. The emission wavelength of Au NCs usually undergoes a redshift with increasing size [35]. The TEM images (Figure 5-2) of PDDA/GSH-Au NCs show that the particle size of PDDA/GSH-Au NCs prepared at pH 11.0 are larger than that (GSH-Au NCs) prepared at pH 2.0, supporting that the red-shifted emission is due to increasing size as a result of aggregation. In addition, at pH 2.0, the fluorescence spectra measured for PDDA/GSH-Au NCs and GSH-Au NCs are similar, supporting our reasoning. The FT-IR spectra of PDDA, GSH-Au NCs, and PDDA/GSH-Au NCs are displayed in Figure 5-3. In the presence of PDDA, the peaks at 1225 cm^{-1} and 1725 cm^{-1}, which are assigned to C–O bending and C=O stretching from the carboxylic acid group of GSH, decreased,

doi:10.6342/NTU202300566

supporting strong electrostatic interactions between PDDA and GSH. In addition to the size effect, the surface change due to PDDA capping is also responsible for the observed difference in the fluorescence [36]. The reaction time to reach a maximum fluorescence intensity is shorter (6 h) at pH 11.0 than that (24 h) at the other pH values, mainly because of the stronger reducing strength of GSH (pI = 5.93) at pH 11.0 [37]. GSH serves as a reducing agent and is oxidized to GSSG, as shown in equation (1). The oxidation potential for the 2GSH/GSSG half-reaction increases upon increasing pH value as shown in equation (2).

$$2\text{GSH} \rightarrow \text{GSSG} + 2e^- + 2\text{H}^+ \quad (1)$$

$$E_{\text{pH}} = 240 + [(\text{pH} - 7.0) \times 59.1]\ \text{mV} \quad (2)$$

Because $HAuCl_4$ is dominant under acidic conditions (< pH 3.0), while $Au(OH)_4^-$ is formed under alkaline conditions (> pH 11.0), the reduction potential for Au^{3+} decreases upon increasing pH value. Thus, Au^{3+} is easier to be reduced under acidic conditions than alkaline conditions [38]. The redox potentials for the formation of GSH-Au NCs were calculated to be approximately 0.9 V and 1.1 V at pH 2.0 and pH 11.0, respectively. Thus, a pH value of 11.0 is favorable for the preparation of GSH-Au NCs.

The fluorescence intensity for PDDA/GSH-Au NCs prepared at pH 11.0 increases upon increasing PDDA concentration from 0% to 1.0%. For a PDDA concentration lower than 0.01%, some aggregates were found, as verified by the observation of weak

doi:10.6342/NTU202300566

fluorescence at a wavelength of approximately 800 nm. Aggregates are mainly formed because of increased attraction between/among PDDA/GSH-Au NCs, as verified by a decreased zeta potential (Table 5-1). Upon further increasing the PDDA concentration, the zeta potential increases, leading to stronger repulsion among the Au NCs, and, thus, a higher stability for the PDDA/GSH-Au NCs. This result shows that PDDA stabilizes the as-formed GSH-Au NCs. At pH 2.0, the effect of PDDA concentration on the fluorescence from PDDA/GSH-Au NCs is negligible, mainly because of electrostatic repulsion with GSH. PDDA and GSH both have positive charges at pH 2.0.

The fluorescence lifetimes determined for PDDA/GSH-Au NCs prepared at various conditions are listed in Table 5-2. These fluorescence lifetimes were calculated by using a two-exponential fitting [$I(t) = A_1 \exp(-t/\tau_1) + A_2 \exp(-t/\tau_2)$] [39]. The long lifetime component (τ_2) originates from LMCT and the short lifetime component (τ_1) is assigned to the singlet transition between the d band to sp band of the Au core [5, 40]. At pH 2.0, τ_1 is dominant for the PDDA/GSH-Au NCs and the PDDA concentration plays an insignificant role in determining the fluorescence lifetime, supporting an insignificant role for PDDA as a template. On the other hand, at pH 11.0, τ_2 values for the PDDA/GSH-Au NCs prepared separately in the presence of a PDDA concentration of 0.1% and 1% are much larger than the NCs prepared with a PDDA concentration of over 0.01%, supporting the template role for PDDA. The contribution from τ_2 is larger

doi:10.6342/NTU202300566

than that from τ_1 at a PDDA concentration higher than 0.1%, which further supports the notion that PDDA is involved in the preparation.

5.3.2 Preparation of PSS/GSH-Au NCs

The GSH-assisted approach was further applied to the preparation of PSS/GSH-Au NCs under similar conditions to that used for the preparation of PDDA/GSH-Au NCs. Like for the case with PDDA, PSS/GSH-Au NCs prepared at pH 2.0 and pH 11.0 have stronger fluorescence intensities compared to those prepared at pH 5.0 and pH 8.0, respectively, as shown in Figure 5-4. The fluorescence observed at 400 nm is from PSS, as verified by the observation of increased fluorescence intensity upon increasing PSS concentration. The reaction was also found to be faster at pH 11.0 as a result of the strong reducing strength of GSH. Unlike PDDA, PSS possesses negative charges at pH > 2.0 [41]. Under acidic conditions (pH < 6.0), PSS over PDDA likely has greater electrostatic interaction with GSH. When prepared in the presence of 0.1% and 1% PSS at pH 2.0, PSS/GSH-Au NCs show two fluorescence emission peaks at 620 nm and 820 nm; meanwhile, PDDA/GSH- and GSH-Au NCs both show only one fluorescence emission peak located at 620 nm [42]. The peaks at 620 and 820 nm are assigned to GSH-Au NCs and PSS/GSH-Au NCs, respectively. Because of the capping of PSS, GSH-Au NCs grow to bigger sizes, leading to a red-shift emission. The PSS/GSH-Au

doi:10.6342/NTU202300566

NCs prepared at pH 2.0 show similar PL emission peak profiles at various pH values over the pH range of 2.0-12.0, mainly because the GSH-Au NCs were capped and stabilized with PSS (pK_a 1.5). Their sizes and zeta potentials remain almost constant at various pH values in the studied range. The fluorescence lifetimes for the PSS/GSH-Au NCs at 620 nm are also listed in Table 5-2, which shows independence of PSS concentration. This result further supports our peak assignment. Because a system that allows for lifetime measurements at 820 nm is unavailable in our lab, the lifetimes for PSS/GSH-Au NCs at 820 nm were not obtained. The PSS/GSH-Au NCs prepared at pH 11.0 emit at 820 nm only in the presence of 1.0% PSS. This result suggests that some other forces such as hydrogen bonding and hydrophobic interaction between PSS and GSH are existent. When prepared in the presence of low PSS concentrations at pH 11.0, formation of $Au(OH)_4^-$ is the main reason to hinder the formation of GSH-Au NCs, and thus the fluorescence is quite weak.

5.3.3 Stability of PDDA/GSH-Au NCs and PSS/GSH-Au NCs

Since the PDDA/GSH-Au NCs prepared at pH 11.0 in the presence of 0.1% and 1.0% PDDA and PSS/GSH-Au NCs prepared at pH 2.0 show stronger fluorescence intensities, their stabilities at various pH values and NaCl concentrations was investigated. For comparison, GSH-Au NCs prepared at pH 2.0 were used. Figure 5-

doi:10.6342/NTU202300566

5A shows that their fluorescence intensities vary over the pH range of 2.0-12.0. In addition to PSS/GSH-Au NCs (at pH 2.0), the other three Au NCs show maximum fluorescence intensities at pH 10.0. At high pH values, PSS and GSH are both negatively charged, and the GSH/Au NCs are not well protected by PSS. Figure 5-5B shows that the four tested Au NCs are stable against NaCl up to a concentration of 500 mM.

5.3.4 Quantitation of sulfide ions

Since PDDA/GSH-Au NCs prepared at pH 11.0 in the presence of 0.1% and 1% PDDA show stronger fluorescence intensities and are stable, they are potential for analytical applications. To minimize the use of a large amount of PDDA and to reduce interference from anions, PDDA/GSH-Au NCs prepared at pH 11.0 in the presence of 0.1% PDDA were selected for quantitation of sulfide ions at pH 10.0. H_2S (pK_{a1} and pK_{a2} of 7.1 and 12.0, respectively) is a highly flammable and toxic gas [43], which has been recognized as a gaseous signal transmitter in many biological processes [44]. H_2S is also the subject of environmental concern as it is produced in many factories and can potentially lead to biological dysfunction. For example, H_2S may cause olfactory fatigue at a concentration of 20 ppm, and may even lead to fatal consequences at concentrations higher than 250 ppm [43]. At pH 10.0, HS^- is dominant, which can

doi:10.6342/NTU202300566

access the surface of PDDA/GSH-Au NCs and then react with surface Au ions and core Au atoms to form Au_2S ($K_{sp} = 1.58 \times 10^{-73}$) [45], leading to fluorescence quenching, as shown in Figure 5-6A. Figure 5-6A displays a fluorescence photograph of the two solutions; meanwhile, Figure 5-6B and its inset shows the TEM image and the size distribution of the PDDA/GSH-Au NCs, respectively. The average NC size was calculated to be 1.9 nm (100 counts). The TEM images displayed in Figure 5-6C verify the formation of large Au_2S particles in the presence of 10 μM Na_2S. The XPS spectra obtained for PDDA/GSH-Au NCs in the absence and presence of Na_2S (10 μM) shown in Figure 5-7 further support the formation of Au_2S. The binding energy (BE) for the Au 4f7/2 electrons in PDDA/GSH-Au NCs was determined to be 83.9 eV, which is located between 83.7 eV (Au (0)) and 84.3 eV (Au(I)), revealing the existence of Au (0) and Au(I) [34]. After reaction with Na_2S, the ratio of Au (0) to Au(I) changed from 1.43:1 to 0.47:1, supporting the formation of Au_2S. The inset of Figure 5-6D shows that the fluorescence ratio ($(I_{Fo} - I_{Fi})/I_{Fo}$) at 690 nm increases linearly against the Na_2S concentration over the range of 1−10 μM ($R^2 = 0.99$), in which I_{Fo} and I_{Fi} are the fluorescence intensities before and after Na_2S addition, respectively. The limit of detection (LOD) provided by this approach at a signal-to-noise ratio of 3 is 0.32 μM, which is much lower than the maximum level permitted in drinking water by the World Health Organization (15 μM). When compared to reported sensing systems, this

doi:10.6342/NTU202300566

approach provides comparable sensitivity for quantitation of sulfide, as listed in Table 5-3 [8, 46-51].

5.3.5 Selectivity and practicality

Before testing this approach for quantitation of sulfide ions in real samples, its selectivity and tolerance was investigated. Figure 5-8A shows that the selectivity of this approach toward H_2S (HS^-) over the test ions (SO_4^{2-}, $S_2O_3^{2-}$, CO_3^{2-}, CH_3COO^-, NO_3^-, F^-, Cl^-, Br^-, I^-, and citrate) is at least 10-fold. Figure 5-8B shows that this approach allows for the detection of 10 μM Na_2S in the presence of tested inferring species at concentrations of up to 100 μM. Figure 3-8C shows that the relative fluorescence change for PDDA/GSH-Au in the spiked spring water sample is linear ($y = 0.048 x + 0.048$, $R^2 = 0.99$) against Na_2S concentration over the range of 1−10 μM. As shown in Table 5-4, the recoveries and relative standard deviation (RSD) for the three samples were determined to be in the ranges from 83% to 90% and 3.8% to 7.8%, respectively. The concentration of sulfide ions in the spring water sample was determined to be 10 ± 1 μM ($n = 3$); meanwhile, this value was determined to be 9 ± 1 μM ($n = 3$) using the methylene blue method approved by APHA. According to the result of Student’s t test (t value of 1.4 under a confidence level of 95%), there is no significant difference between these two approaches, revealing that the PDDA/GSH-Au NCs have great potential for monitoring of sulfide level in environmental samples.

5.4 Conclusion

We demonstrated a GSH-assisted approach for the preparation of polymer-capped Au NCs with emission in the NIR region. Our study shows that the concentration and charge of the polymer and the pH value play important roles in determining the formation of polymer-capped Au NCs. In the presence of GSH as a reducing agent and PDDA as a template, stable PDDA/GSH-Au NCs were prepared at pH 11.0 within 6 h. In the GSH-assisted preparation system, PDDA over PSS is more suitable for the preparation of Au NCs with respect to fluorescence intensity and stability. More importantly, low-cost PDDA/GSH-Au NCs were found to be as stable as our previously prepared GSH/BSA-Au NCs. We also found that when excited at 365 nm, GSH-Au NCs and PDDA/GSH-Au NCs separately emit at the wavelengths of 620 and 800 nm. Due to their greater stability against salt, the PDDA/GSH-Au NCs are sensitive and selective for the quantitation of sulfides ions in real samples, based on analyte-induced fluorescence quenching. The practicality of this assay was validated by the detection of sulfide ions in spring water samples, showing its potential for environmental analysis.

5.5 References

[1] L.B. Zhang, E.K. Wang, Metal nanoclusters: New fluorescent probes for sensors and bioimaging, Nano Today, 9 (2014) 132–157.

[2] J. Sun, Y.D. Jin, Fluorescent Au nanoclusters: recent progress and sensing applications, J Mater Chem C, 2 (2014) 8000–8011.

[3] S.W. Chen, R.S. Ingram, M.J. Hostetler, J.J. Pietron, R.W. Murray, T.G. Schaaff, et al., Gold nanoelectrodes of varied size: Transition to molecule-like charging, Science, 280 (1998) 2098–2101.

[4] Y.Y. Huang, L. Fuksman, J. Zheng, Luminescence mechanisms of ultrasmall gold nanoparticles, Dalton T, 47 (2018) 6267–6273.

[5] J. Zheng, C. Zhou, M.X. Yu, J.B. Liu, Different sized luminescent gold nanoparticles, Nanoscale, 4 (2012) 4073–4083.

[6] X. Yuan, Z.T. Luo, Y. Yu, Q.F. Yao, J.P. Xie, Luminescent Noble Metal Nanoclusters as an Emerging Optical Probe for Sensor Development, Chem-Asian J, 8 (2013) 858–871.

[7] L.-Y. Chen, C.-W. Wang, Z. Yuan, H.-T. Chang, Fluorescent gold nanoclusters: recent advances in sensing and imaging, Anal Chem, 87 (2015) 216–229.

doi:10.6342/NTU202300566

[8] Z.Q. Yuan, M.H. Peng, L. Shi, Y. Du, N. Cai, Y. He, et al., Disassembly mediated fluorescence recovery of gold nanodots for selective sulfide sensing, Nanoscale, 5 (2013) 4683–4686.

[9] Y.-J. Liao, Y.-C. Shiang, C.-C. Huang, H.-T. Chang, Molecularly Imprinted Aptamers of Gold Nanoparticles for the Enzymatic Inhibition and Detection of Thrombin, Langmuir, 28 (2012) 8944–8951.

[10] F. Wen, Y.H. Dong, L. Feng, S. Wang, S.C. Zhang, X.R. Zhang, Horseradish Peroxidase Functionalized Fluorescent Gold Nanoclusters for Hydrogen Peroxide Sensing, Anal Chem, 83 (2011) 1193–1196.

[11] Y.-W. Lin, C.-C. Huang, H.-T. Chang, Gold nanoparticle probes for the detection of mercury, lead and copper ions, Analyst, 136 (2011) 863–871.

[12] K. Aslan, J.R. Lakowicz, C.D. Geddes, Nanogold plasmon resonance-based glucose sensing. 2. Wavelength-ratiometric resonance light scattering, Anal Chem, 77 (2005) 2007–2014.

[13] Y. Yang, L.Q. Lu, X.K. Tian, Y. Li, C. Yang, Y.L. Nie, et al., Ratiometric fluorescence detection of mercuric ions by sole intrinsic dual-emitting gold nanoclusters, Sensor Actuat B-Chem, 278 (2019) 82–87.

doi:10.6342/NTU202300566

[14] K. Sokolowska, E. Hulkko, L. Lehtovaara, T. Lahtinen, Dithiol-Induced Oligomerization of Thiol-Protected Gold Nanoclusters, J Phys Chem C, 122 (2018) 12524–12533.

[15] D. Mishra, F. Aldeek, E. Lochner, G. Palui, B.R. Zeng, S. Mackowski, et al., Aqueous Growth of Gold Clusters with Tunable Fluorescence Using Photochemically Modified Lipoic Acid-Based Ligands, Langmuir, 32 (2016) 6445–6458.

[16] Z.K. Wu, R.C. Jin, Stability of the Two Au-S Binding Modes in Au-25 (SG)(18) Nanoclusters Probed by NMR and Optical Spectroscopy, Acs Nano, 3 (2009) 2036–2042.

[17] Y. Negishi, Y. Takasugi, S. Sato, H. Yao, K. Kimura, T. Tsukuda, Magic-numbered Au-n clusters protected by glutathione monolayers (n=18, 21, 25, 28, 32, 39): Isolation and spectroscopic characterization, J Am Chem Soc, 126 (2004) 6518–6519.

[18] F.N. Lu, H.W. Yang, Y. Tang, C.-J. Yu, G.R. Wang, Z.Q. Yuan, et al., 11-Mercaptoundecanoic acid capped gold nanoclusters with unusual aggregation-enhanced emission for selective fluorometric hydrogen sulfide determination, Microchim Acta, 187 (2020) DOI: 10.1007/s00604-020-4159-1.

[19] J.-G. You, W.-L. Tseng, Peptide-induced aggregation of glutathione-capped gold nanoclusters: A new strategy for designing aggregation-induced enhanced emission probes, Anal Chim Acta, 1078 (2019) 101–111.

[20] N. Goswami, Q.F. Yao, T.K. Chen, J.P. Xie, Mechanistic exploration and controlled synthesis of precise thiolate-gold nanoclusters, Coordin Chem Rev, 329 (2016) 1–15.

[21] R.R. Nasaruddin, T.K. Chen, J.G. Li, N. Goswami, J.G. Zhang, N. Yan, et al., Ligands Modulate Reaction Pathway in the Hydrogenation of 4-Nitrophenol Catalyzed by Gold Nanoclusters, Chemcatchem, 10 (2018) 395–402.

[22] T. Higaki, C. Liu, M. Zhou, T.Y. Luo, N.L. Rosi, R.C. Jin, Tailoring the Structure of 58-Electron Gold Nanoclusters: Au103S2(S-Nap)(41) and Its Implications, J Am Chem Soc, 139 (2017) 9994–10001.

[23] Z.K. Wu, R.C. Jin, On the Ligand's Role in the Fluorescence of Gold Nanoclusters, Nano Lett, 10 (2010) 2568–2573.

[24] D.M. Chevrier, L. Raich, C. Rovira, A. Das, Z.T. Luo, Q.F. Yao, et al., Molecular-Scale Ligand Effects in Small Gold-Thiolate Nanoclusters, J Am Chem Soc, 140 (2018) 15430–15436.

[25] H.-Y. Chang, Y.-T. Tseng, Z.-Q. Yuan, H.-L. Chou, C.-H. Chen, B.-J. Hwang, et al., The effect of ligand-ligand interactions on the formation of photoluminescent

doi:10.6342/NTU202300566

gold nanoclusters embedded in Au(I)-thiolate supramolecules, Phys Chem Chem Phys, 19 (2017) 12085–12093.

[26] H. Cheng, L.N. Yang, Y. Jiang, Y.Y. Huang, Z.H. Sun, J. Zhang, et al., Adsorption kinetic process of thiol ligands on gold nanocrystals, Nanoscale, 5 (2013) 11795–11800.

[27] C.-C. Huang, Z. Yang, K.-H. Lee, H.-T. Chang, Synthesis of highly fluorescent gold nanoparticles for sensing Mercury(II), Angew Chem Int Edit, 46 (2007) 6824–6828.

[28] X.R. Song, N. Goswami, H.H. Yang, J.P. Xie, Functionalization of metal nanoclusters for biomedical applications, Analyst, 141 (2016) 3126–3140.

[29] Y.-Q. Wang, Y.-Y. Zhang, X.-G. Wu, X.-W. He, W.-Y. Li, Rapid facile in situ synthesis of the Au/Poly(N-isopropylacrylamide) thermosensitive gels as temperature sensors, Mater Lett, 143 (2015) 326–329.

[30] J. Zheng, J.T. Petty, R.M. Dickson, High quantum yield blue emission from water-soluble Au-8 nanodots, J Am Chem Soc, 125 (2003) 7780–7781.

[31] Y.J. Ju, N. Li, S.G. Liu, L. Han, N. Xiao, H.Q. Luo, et al., Ratiometric fluorescence method for malachite green detection based on dual-emission BSA-protected gold nanoclusters, Sensor Actuat B-Chem, 275 (2018) 244–250.

[32] B.-Y. Wu, C.-W. Wang, P.-C. Chen, H.-T. Chang, Glutathione assisted preparation of gold nanoclusters using minimum amount of protein, Sensor Actuat B-Chem, 238 (2017) 1258–1265.

[33] A.D. Eaton, L.S. Clesceri, A.E. Greenberg, M.A.H. Franson, Standard methods for the examination of water and wastewater. 20th ed., (1998).

[34] Z.T. Luo, X. Yuan, Y. Yu, Q.B. Zhang, D.T. Leong, J.Y. Lee, et al., From Aggregation-Induced Emission of Au(I)-Thiolate Complexes to Ultrabright Au(0)@Au(I)-Thiolate Core-Shell Nanoclusters, J Am Chem Soc, 134 (2012) 16662–16670.

[35] N. Schaeffer, B. Tan, C. Dickinson, M.J. Rosseinsky, A. Laromaine, D.W. McComb, et al., Fluorescent or not? Size-dependent fluorescence switching for polymer-stabilized gold clusters in the 1.1-1.7 nm size range, Chem Commun, (2008) 3986–3988.

[36] X. Yuan, N. Goswami, W.L. Chen, Q.F. Yao, J.P. Xie, Insights into the effect of surface ligands on the optical properties of thiolated Au-25 nanoclusters, Chem Commun, 52 (2016) 5234–5237.

[37] F.Q. Schafer, G.R. Buettner, Redox environment of the cell as viewed through the redox state of the glutathione disulfide/glutathione couple, Free Radical Bio Med, 30 (2001) 1191–1212.

[38] D.V. Goia, E. Matijevic, Tailoring the particle size of monodispersed colloidal gold, Colloid Surface A, 146 (1999) 139–152.

[39] D. Fixler, T. Nayhoz, K. Ray, Diffusion Reflection and Fluorescence Lifetime Imaging Microscopy Study of Fluorophore-Conjugated Gold Nanoparticles or Nanorods in Solid Phantoms, Acs Photonics, 1 (2014) 900–905.

[40] X. Le Guevel, B. Hotzer, G. Jung, K. Hollemeyer, V. Trouillet, M. Schneider, Formation of Fluorescent Metal (Au, Ag) Nanoclusters Capped in Bovine Serum Albumin Followed by Fluorescence and Spectroscopy, J Phys Chem C, 115 (2011,) 10955–10963.

[41] L.G. Li, L.H. Ferng, Y. Wei, C. Yang, H.F. Ji, Effects of acidity on the size of polyaniline-poly(sodium 4-styrenesulfonate) composite particles and the stability of corresponding colloids in water, J Colloid Interf Sci, 381 (2012) 11–16.

[42] J. Zheng, C.W. Zhang, R.M. Dickson, Highly fluorescent, water-soluble, size-tunable gold quantum dots, Phys Rev Lett, 93 (2004) 077402.

[43] R.J. Reiffenstein, W.C. Hulbert, S.H. Roth, Toxicology of Hydrogen-Sulfide, Annu Rev Pharmacol, 32 (1992) 109–134.

[44] K. Abe, H. Kimura, The possible role of hydrogen sulfide as an endogenous neuromodulator, J Neurosci, 16 (1996) 1066–1071.

doi:10.6342/NTU202300566

[45] T. Morris, H. Copeland, G. Szulczewski, Synthesis and characterization of gold sulfide nanoparticles, Langmuir, 18 (2002) 535–539.

[46] Y. Zhang, H.Y. Shen, X. Hai, X.W. Chen, J.H. Wang, Polyhedral Oligomeric Silsesquioxane Polymer-Caged Silver Nanoparticle as a Smart Colorimetric Probe for the Detection of Hydrogen Sulfide, Anal Chem, 89 (2017) 1346–1352.

[47] P.-C. Chen, Y.-C. Li, J.-Y. Ma, J.-Y. Huang, C.-F. Chen, H.-T. Chang, Size-tunable copper nanocluster aggregates and their application in hydrogen sulfide sensing on paper-based devices, Sci Rep-Uk, 6 (2016) 24882.

[48] Z.H. Li, S. Guo, C. Lu, A highly selective fluorescent probe for sulfide ions based on aggregation of Cu nanocluster induced emission enhancement, Analyst, 140 (2015) 2719–2725.

[49] J. Fan, R.P. Li, P.P. Xu, J.W. Di, Y.F. Tu, J.L. Yan, Sensitive Sulfide Sensor with a Trypsin-stabilized Gold Nanocluster, Anal Sci, 30 (2014) 457–462.

[50] M.L. Cui, J.M. Liu, X.X. Wang, L.P. Lin, L. Jiao, Z.Y. Zheng, et al., A promising gold nanocluster fluorescent sensor for the highly sensitive and selective detection of S^{2-}, Sensor Actuat B-Chem, 188 (2013) 53–58.

[51] J. Liu, J.H. Chen, Z.Y. Fang, L.W. Zeng, A simple and sensitive sensor for rapid detection of sulfide anions using DNA-templated copper nanoparticles as fluorescent probes, Analyst, 137 (2012) 5502–5505.

Table 5-1. Zeta potential of polymer/GSH-Au NCs prepared under different conditions.

Polymer	**pH**	**Conc. (%)**	**ζ (mV)** [a]
PDDA	2.0	0.01%	-12.9
		0.1%	18.2
		1%	23.2
	11.0	0.01%	-35.2
		0.1%	17.1
		1%	32.6
PSS	2.0	0.01%	-63.8
		0.1%	-70.2
		1%	-77.2

[a] The zeta potentials were measured at the synthetic pH value.

doi:10.6342/NTU202300566

Table 5-2. Fluorescence lifetimes of polymer/GSH-Au NCs prepared under different conditions.

Polymer	**pH**	**Conc. (%)**^{a}	**I (λ_{em}, nm)**^{b}	**τ_1 (ns)**	**τ_2 (ns)**
PDDA	2.0	0.01%	620	213 (71%)	1236 (29%)
		0.1%	620	406 (78%)	3000 (22%)
		1%	620	383 (68%)	2348 (32%)
	11.0	0.01%	680	153 (66%)	793 (34%)
		0.1%	690	752 (49%)	1695 (51%)
		1%	700	570 (47%)	1540 (53%)
PSS	2.0	0.01%	620	294 (71%)	1720 (29%)
		0.1%	620	241 (74%)	1720 (26%)
		1%	620	211 (68%)	1912 (32%)

[a] the concentration of polymer used in the preparation.

[b] Fluorescence intensity: I

Table 5-3. Comparison of nanomaterials-based sulfide sensors.

Nanomaterial	**Linear range (μM)**	**LOD (nM)**	**Ref.**
Au NDs	0.5－157	500	8
BSA-Au NCs	0.1－30	29	46
Trypsin-Au NCs	0.05－8	5.5	47
POSS[1]-Ag NPs	0.7－10	200	48
DNA-Cu NPs	0.2－2 2－20	80	49
PSS-PA[2]-Cu NCs	1－20	650	50
Cysteine-Cu NCs	0.2－50	42	51
PDDA/GSH-Au NCs	1－10	320	This study

[1] POSS: Polyhedral oligomeric silsesquioxane

[2] PSS-PA: Poly(styrenesulfonate)-penicillamine

Table 5-4. Recovery for sulfide detection in the real sample.

Sample	**Added (μM)**	**Found (μM)**	**Recovery (%)**	**RSD (%)**
Spring Water	0	1.14	-	-
	1	2.01	87%	7.8%
	6	6.09	83%	7.7%
	8	8.36	90%	3.8%

doi:10.6342/NTU202300566

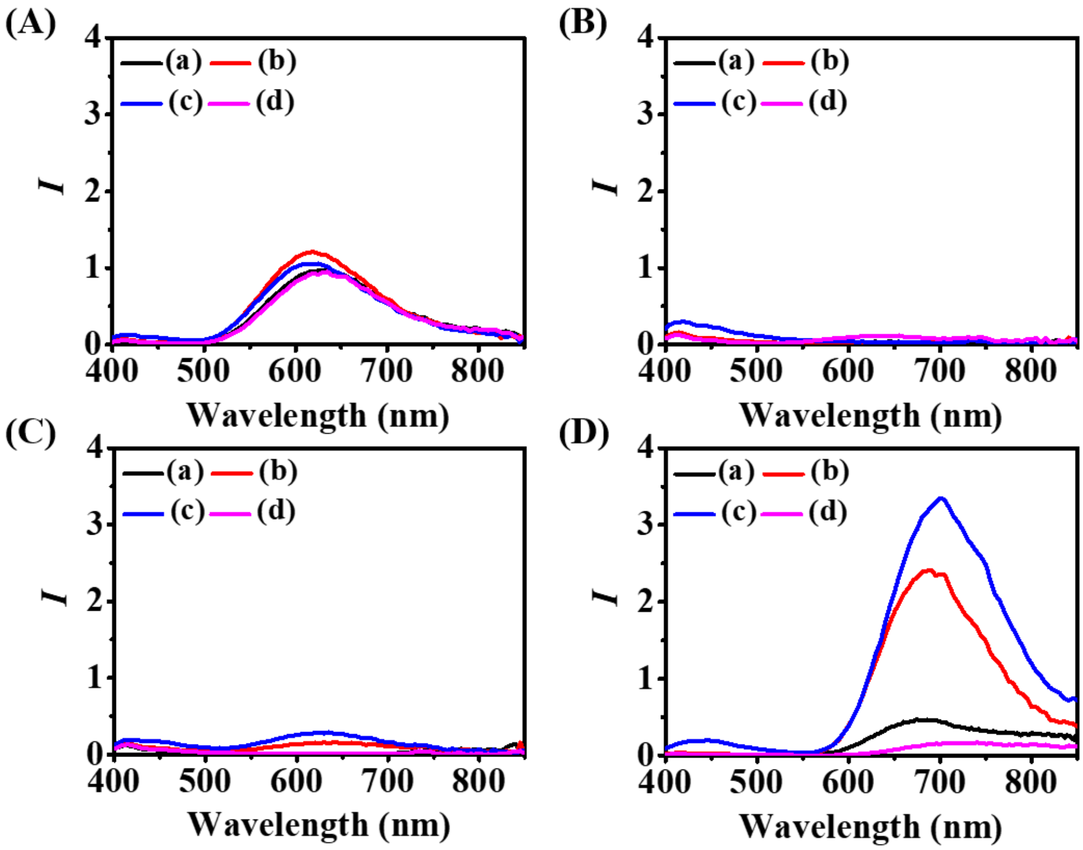

Figure 5-1. Fluorescence spectra for PDDA/GSH-Au NCs (0.1X) prepared in the presence of (a) 0.01%, (b) 0.1%, (c) 1% (d) 0% PDDA at pH values of (A) 2.0, (B) 5.0, (C) 8.0, and (D) 11.0. Fluorescence intensity (I) is plotted in arbitrary units when excited at a wavelength of 365 nm. The PDDA/GSH-Au NCs used for fluorescence measurements were prepared in phosphate buffer (20 mM, pH 7.0).

doi:10.6342/NTU202300566

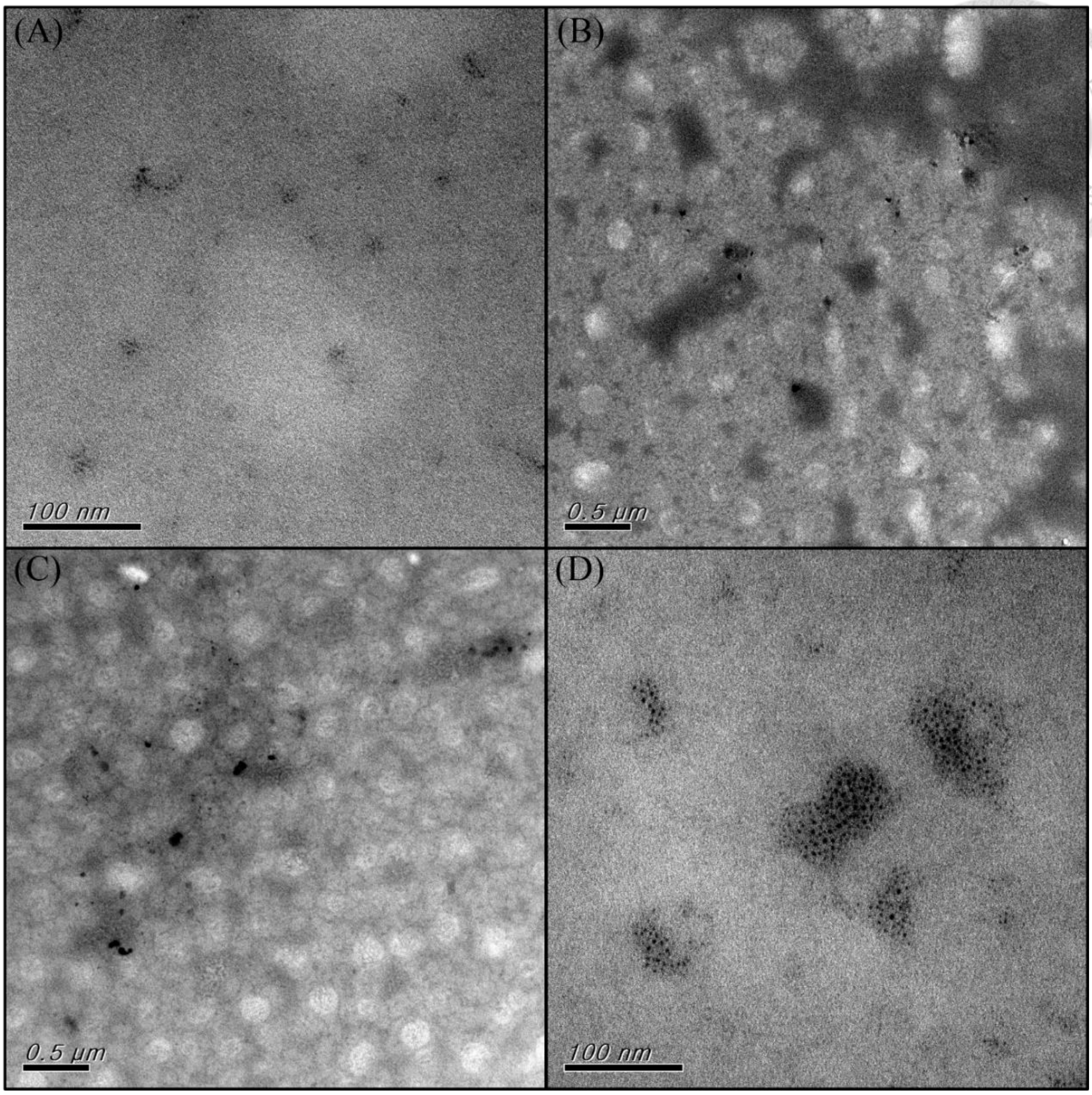

Figure 5-2. TEM images of PDDA/GSH-Au NCs synthesized at pH (A) 2, (B) 5, (C) 8, and (D) 11.

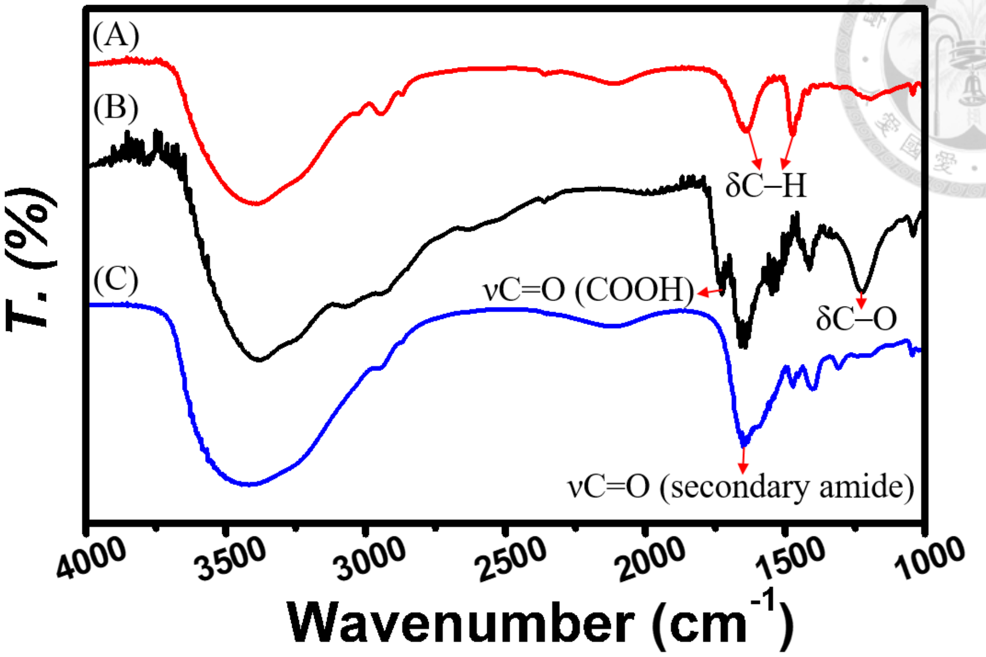

Figure 5-3. FTIR spectra of (A) PDDA, (B) GSH-Au NCs, and (C) PDDA/GSH-Au NCs.

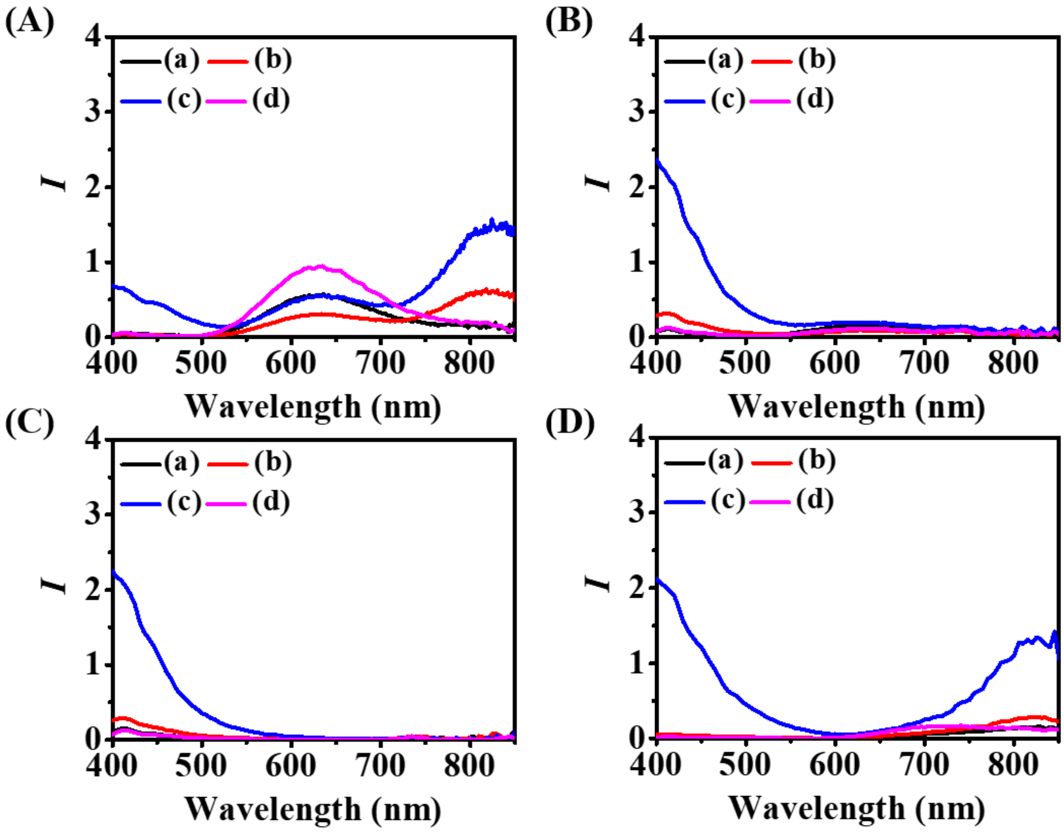

Figure 5-4. Fluorescence spectra for PSS/GSH-Au NCs (0.1X) prepared in the presence of (a) 0.01%, (b) 0.1%, (c) 1% (d) 0% PSS at pH values of (A) 2.0, (B) 5.0, (C) 8.0, and (D) 11.0. Other conditions are the same as in Figure 5-1.

doi:10.6342/NTU202300566

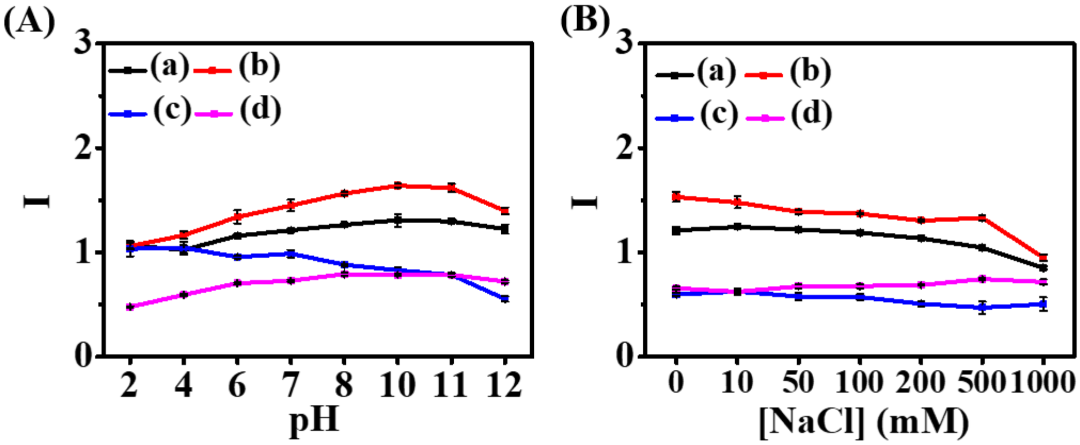

Figure 5-5. Effects of (A) pH (B) NaCl concentration on the fluorescence intensity of four types of Au NCs. PDDA/GSH-Au NCs prepared in the presence of (a) 0.1% and (b) 1% PDDA at pH 11.0. (c) PSS/GSH-Au NCs prepared in the presence of 1% PSS at pH 2.0. (d) GSH-Au NCs prepared at pH 2.0. Emission wavelengths (nm) are (a) 700 nm, (b) 690 nm, (c) 820 nm, and (d) 620 nm. (A) 10 mM PB solution, (B) pH 7.0. Other conditions are the same as in Figure 5-1.

doi:10.6342/NTU202300566

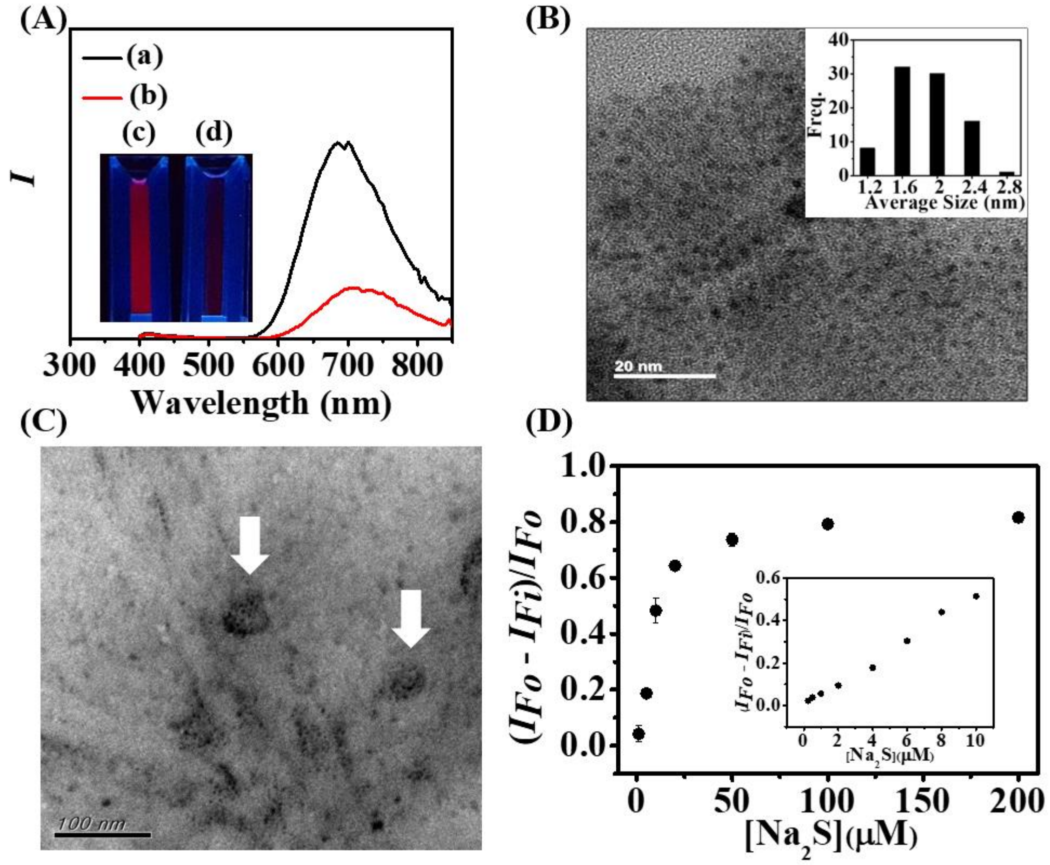

Figure 5-6. Effects of sodium sulfide on PDDA/GSH-Au NCs. (A) Fluorescence spectra for PDDA/GSH-Au NCs in the absence (a) and presence (b) of 10 μM Na_2S and (c, d) their corresponding fluorescence photographs. (B) and (C) show the corresponding TEM images. Inset in (B) shows the size distribution for the PDDA/GSH-Au NCs. (D) Detection of Na_2S using PDDA/GSH-Au NCs (0.05X) in phosphate buffer (10 mM, pH 10.0), in which I_{F0} and I_{Fi} are the fluorescence intensities for PDDA/GSH Au NCs at 690 nm measured in the absence and presence of S^{2-}, respectively. Inset in (D): linear range of the fluorescence ratio against Na_2S concentration. Other conditions are the same as in Figure 5-1.

doi:10.6342/NTU202300566

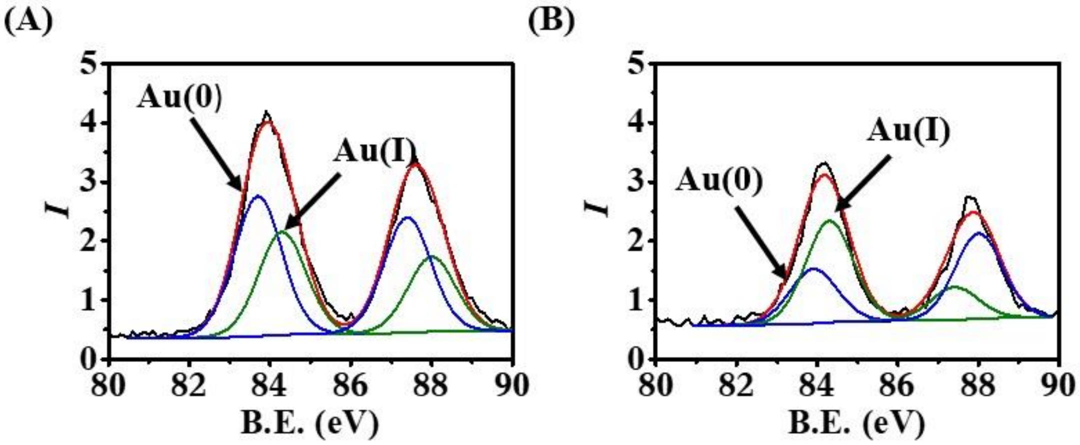

Figure 5-7. XPS of PDDA/GSH-Au NCs in the (A) absence and (B) presence of 10 μM of S^{2-} ions. Intensity (I) is plotted in an arbitrary unit.

doi:10.6342/NTU202300566

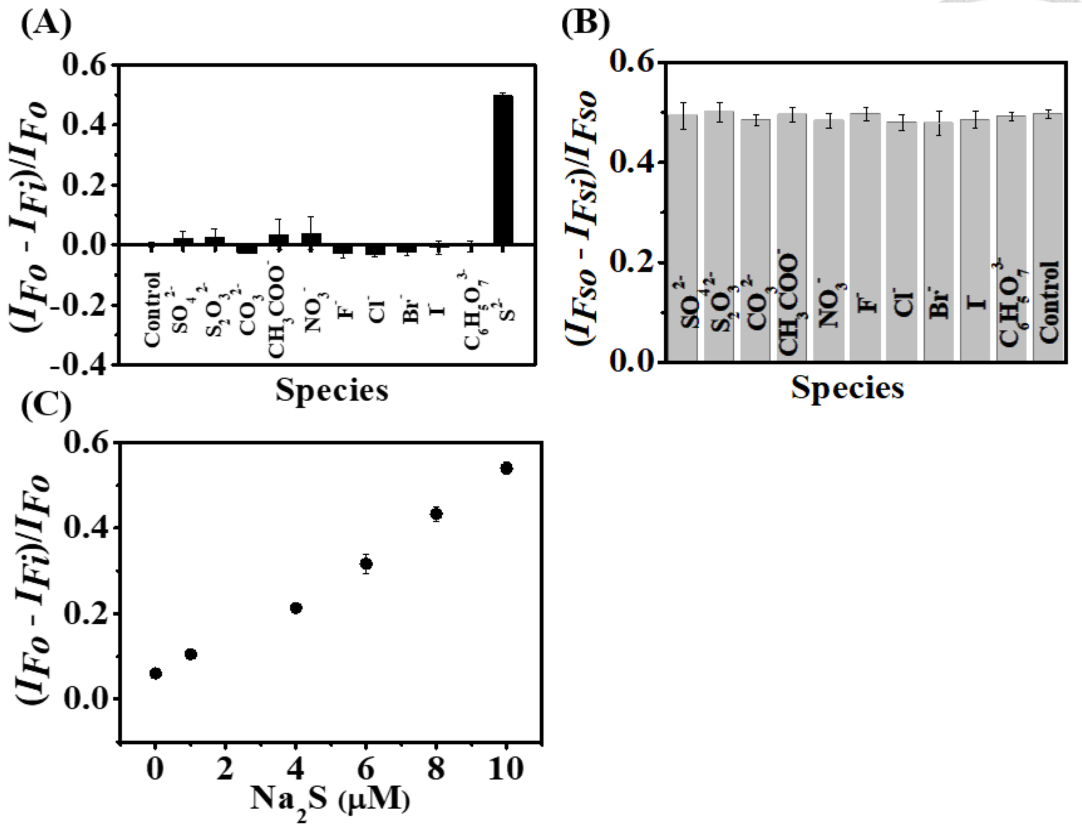

Figure 5-8. PDDA/GSH-Au NCs for the detection of S^{2-}. (A) Selectivity, (B) interference test, and (C) linearity for S^{2-} in spring water. The concentration of S^{2-} in (A) and (B) is 10 μM, and the tested anions in (B) have a concentration of 100 μM. Other conditions are the same as in Figure 3-1.

doi:10.6342/NTU202300566

Conclusions and Prospect

In this work, we developed metal ion (Cu^{2+}), anion (S^{2-} and ClO^{-}), hydrophobic metal complex (SCC), and pH sensors using photoluminescent nanomaterials. In the first part, histidine C dots were prepared using a simple electrochemical approach. When compared to hydrothermal routes, the reaction rate can be boosted by increasing the concentration of the electrolyte. In the second part, hydrophobic carbon dots (TO-C dots) showed us that nanosensors can work in a hydrophobic matrix. In the third part, a hypochlorite sensor, mPA CNPs with excellent selectivity and good sensitivity was developed. In the final part, we successfully synthesized and stabilized GSH-Au NCs by capping them with a polymer.

Although we have successfully expanded the potential for mass production and application of fluorescent nanosensors, to this day, no such products have become mainstream, indicating that the public and even regulators still have doubts about such materials. One of the most common problems is the purity of nanomaterials, especially the uniformity of C dots. Most nanomaterials can only be roughly identified and separated by size or morphology in current research. To define the purity of nanomaterials, we need better identification techniques that can quickly analyze the functional groups on each nanoscale particle to establish purity standards. The current

doi:10.6342/NTU202300566

size-based purification methods are not sufficient to convince the public, and we must achieve a certain level of uniformity in the functional groups on each C dot to explain the purity in terms of chemical properties. We can achieve this goal by purifying and developing more controllable synthesis methods, as well as developing new material identification methods. In this study, the electrochemical and chemical oxidation methods shows a greater ability to control the direction and rate of reactions compared to the current mainstream hydrothermal method, which promotes all reactions at high temperature and high pressure in a disordered manner.

Appendix: Publications

Papers:

[1] **Y.-S. Lin**, Y Lin, A.P. Periasamy, J Cang, H.-T. Chang, Parameters affecting the synthesis of carbon dots for quantitation of copper ions. Nanoscale Adv. 1 (2019) 2553–2561.

[2] **Y.-S. Lin**, T.-C. Chiu, C.-C. Hu, Fluorescence-tunable copper nanoclusters and their application in hexavalent chromium sensing. RSC adv. 9 (2019) 9228–9234.

[3] **Y.-S. Lin**, L.-W. Chuang, B.-Y. Wu, Y.-H. Lin, H.-T. Chang, Polymer/glutathione Au nanoclusters for detection of sulfides. Sens. actuators. B Chem. 333 (2021) 129356

[4] **Y.-S. Lin**, Y.-F. Lin, A Nain, Y.-F. Huang, H.-T. Chang, A critical review of copper nanoclusters for monitoring of water quality. Sensors and Actuators Reports 3 (2021) 100026.

[5] **Y.-S. Lin**, Z.-Y. Yang, A Anand, C.-C. Huang, H.-T. Chang, Carbon dots with polarity-tunable characteristics for the selective detection of sodium copper chlorophyllin and copper ions. Anal. Chim. Acta 1191 (2022) 339311.

[6] **Y.-S. Lin**, L.-W. Chuang, Y.-F. Lin, S.-R. Hu, C.-C. Huang, Y.-F. Huang, H.-T. Chang, Development of Fluorescent Carbon Nanoparticle-Based Probes for Intracellular pH and Hypochlorite Sensing. Chemosensors 10 (2022) 64.

doi:10.6342/NTU202300566